

# Investigating the Effect of Curvature on Chiral Domain Wall Velocity

Dissertation

zur Erlangung des Doktorgrades der Ingenieurwissenschaften (Dr. Ing.)

der

Naturwissenschaftlichen Fakultät II  
Chemie, Physik und Mathematik

der Martin-Luther-Universität Halle-Wittenberg

vorgelegt von

Herr **Chirag Garg**

geb. am 19.11.1991 in Kapurthala, Indien

Gutachter: Prof. Dr. Stuart S.P. Parkin

Prof. Dr. Georg Woltersdorf

Prof. Dr. Christan Back

Tag der öffentlichen Verteidigung: 30.04.2019



# Abstract

The invention of the modern hard disk drive a few decades ago ushered us in the information age and led to the boom of digital media, social networks and internet search engines. Since then, the amount of data being generated every year has increased tremendously while the improvements in the capacity of conventional forms of storage have struggled to keep pace. Racetrack memory is a proposed storage device that can overcome the fundamental limits of cramming information in two dimensions, which most conventional storage technologies are based on. The concept involves the use of domain walls, which are transition regions between magnetic domains of different orientations. Patterns of information can be encoded in the spacing between consecutive domain walls, which can then be electrically induced to move forward or backward along a magnetic nanowire, allowing read-write operations. The lock-step motion of domain walls in response to current pulses is what allows information to be retained during operations.

To store information in dense arrays of magnetic nanowires fabricated in three dimensions may involve curvature or bends that the domain walls would have to travel through. Despite the sustained interest in the motion of domain walls for over a decade, most of the studies on the current-driven motion have been performed on straight wires. Here, we demonstrate that chiral domain walls stabilized by Dzyaloshinskii-Moriya interaction dramatically speed up or slow down depending on the curvature of the wire. Alternating domain walls move with different speeds leading to the loss of lock-step motion and loss of information. We conduct experiments and develop an analytical model to reveal that this discrepancy in

the domain wall velocity arises from the distinct tilting behaviour of chiral domain walls for opposite curvatures. This serious problem can be solved by fabricating nanowires made out of a synthetic antiferromagnetic structure coupled through a Ru interlayer. We also show a novel application utilizing the effect of curvature in a magnetic domain sorter made out of a Y-shaped device. Our findings solve an unanticipated problem in the implementation of the racetrack memory in three dimensions as well as unravel a new mechanism for manipulating the dynamics of chiral domain walls.

# Contents

<b>Abstract</b>	<b>iii</b>
<b>Contents</b>	<b>iv</b>
<b>List of Figures</b>	<b>vii</b>
<b>Abbreviations</b>	<b>ix</b>
<b>1 Introduction</b>	<b>1</b>
1.1 Motivation . . . . .	1
1.2 Domain walls for racetrack memory . . . . .	2
1.3 Scope of the thesis . . . . .	4
<b>2 Background</b>	<b>7</b>
2.1 Introduction to Magnetism and Domain Walls . . . . .	7
2.2 Dzyaloshinskii-Moriya Exchange Interaction . . . . .	11
2.3 Domain-Wall Dynamics . . . . .	13
2.3.1 Spin transfer torque terms . . . . .	14
2.3.2 Torques arising from spin-orbit interactions . . . . .	16
<b>3 Experimental Methods</b>	<b>23</b>
3.1 Sample Preparation . . . . .	23
3.2 Magneto-Optical Kerr Effect . . . . .	26
3.3 Measurements of DW motion . . . . .	28
<b>4 Experimental results on the motion of DWs in a curved wire</b>	<b>33</b>
4.1 Device structure for experiments . . . . .	34
4.2 Experimental Results . . . . .	36
<b>5 Mechanism underlying the role of curvature</b>	<b>41</b>
5.1 Effect of DW tilting on the motion of DWs . . . . .	42

---

5.2	Comparison with experimental results . . . . .	45
5.3	Effect of curvature in narrow nanowires . . . . .	46
5.4	Comparison with micromagnetic simulations . . . . .	47
5.5	Elimination of the effect of curvature in synthetic antiferromagnetic structures . . . . .	49
<b>6</b>	<b>Highly Asymmetric Chiral Domain-Wall Velocities in Y-Shaped Junctions</b>	<b>53</b>
6.1	Experimental Details . . . . .	54
6.2	Analytical model for interpretation of results . . . . .	60
6.3	A Y-shaped domain sorting device . . . . .	68
<b>7</b>	<b>Conclusions</b>	<b>71</b>
<b>A</b>	<b>Quasi two-dimensional model for DW tilting in a curved wire</b>	<b>77</b>
A.1	Quasi two-dimensional model for DW tilting in a curved wire . . .	77
A.1.1	Definition of curvature . . . . .	79
A.1.2	Non-uniform anisotropy induced pinning effect . . . . .	81
A.1.3	Thermal broadening . . . . .	82
A.1.4	Non-uniform current distribution . . . . .	83
A.1.5	Lagrangian and Equations of Motion . . . . .	85
	<b>Bibliography</b>	<b>91</b>
	<b>Publications</b>	<b>103</b>
	<b>Acknowledgements</b>	<b>105</b>
	<b>Curriculum Vitae</b>	<b>107</b>
	<b>Eidesstattliche Erklärung</b>	<b>109</b>

# List of Figures

1.1	Illustration of a simple DW-based memory device. . . . .	3
1.2	Racetrack memory device as a concept. . . . .	4
2.1	Reduction of the magnetostatic energy in a ferromagnet by the process of domain formation. . . . .	8
2.2	Néel and Bloch DW configurations in PMA nanowires. . . . .	10
2.3	Néel DWs with opposite chirality. . . . .	13
2.4	Motion of a moment under field torque and damping torque. . . . .	14
2.5	Spin Hall effect. . . . .	19
2.6	Chiral domain wall motion. . . . .	21
3.1	Steps involved in the fabrication process. . . . .	25
3.2	Gold contact deposition using lithography. . . . .	25
3.3	Magneto-optic Kerr effect. . . . .	26
3.4	Nature of linearly polarized light. . . . .	27
3.5	Circular dichroism. . . . .	27
3.6	MOKE hysteresis loop of a Pt/Co/Ni/Co PMA film. . . . .	28
3.7	Electrical circuit for DW motion measurements. . . . .	29
3.8	Tracking of a DW position using Kerr microscopy. . . . .	30
3.9	Displacement plot for a DW as a function of pulse length. . . . .	31
4.1	Micrograph of a U-shaped device. . . . .	35
4.2	Conventions for DW motion measurements. . . . .	35
4.3	$d$ vs $t$ plot in a curved wire . . . . .	36
4.4	$v$ versus $J$ plot in a U-shaped device with $R = 7 \mu\text{m}$ and $w = 2 \mu\text{m}$	37
4.5	Kerr images showing expansion or contraction of a domain in a curved nanowire . . . . .	38
4.6	$v$ versus $J$ plot for magnetic stacks with different Pt overlayer/underlayer thickness. . . . .	39
4.7	Truth table denoting the influence of curvature on DW speed. . . . .	39
4.8	DW motion in a curved wire depending on $w$ and $\kappa$ . . . . .	40

---

5.1	DW tilting in a straight wire. . . . .	43
5.2	Schematic illustration of the parameters that describe the current-induced DW motion in a curved wire. . . . .	44
5.3	Comparison of Q2D model simulation results (with effects of non-uniform current density, pinning and thermal fluctuations included). . . . .	46
5.4	Q2D model simulation results for narrow nanowires. . . . .	47
5.5	Comparison of the Q2D model with micromagnetic simulations. . . . .	48
5.6	DW motion along a curved wire in a synthetic antiferromagnet (SAF) structure . . . . .	50
6.1	Out-of-equilibrium motion of DWs and Y-shaped device structure. . . . .	55
6.2	Current crowding in the Y-shape structure. . . . .	56
6.3	Measurement sequence. . . . .	57
6.4	Asymmetric DW propagation in the Y-shaped device. . . . .	59
6.5	Schematic for the modelling of DW motion in a Y-shape device. . . . .	61
6.6	Extended 1D model results for a Y-shaped device. . . . .	65
6.7	Influence of width on Y-shape device. . . . .	67
6.8	Symmetric DW motion in synthetic antiferromagnetically (SAF) coupled racetracks. . . . .	68
6.9	DW splitting versus sorting. . . . .	70
A.1	Schematic illustration of basic parameters used in the Q2D model . . . . .	80
A.2	Profile of periodic variation in pinning . . . . .	82
A.3	Calculation of thermal broadening . . . . .	84
A.4	Schematic of current distribution in curved wire . . . . .	85



# Abbreviations

DW	Domain Wall
SAF	Synthetic AntiFerromagnet
FM	FerroMagnet
NM	Non-Magnetic metal
HM	Heavy Metal
PMA	Perpendicular Magnetic Anisotropy
IPA	In-Plane magnetic Anisotropy
MTJ	Magnetic Tunnel Junction
DMI	Dzyaloshinskii-Moriya Interaction
SHE	Spin Hall effect
DC	Direct Current
LLG	Landau-Lifshitz-Gilbert
STT	Spin Transfer Torque
AHE	Anomalous Hall Effect
MOKE	Magneto-Optic Kerr Effect
Q2D	Quasi-Two Dimensional
MRAM	Magnetic Random Access Memory
SHA	Spin Hall Angle



# Chapter 1

## Introduction

### 1.1 Motivation

Magnetic domain walls (DWs) are transition regions between adjacent magnetic domains that are polarized in different directions. They have been an area of active research due to the variety of properties and behaviour they exhibit. At the same time, they are also technologically relevant because of their role in magnetization reversal in various forms of magnetic memory. Early work[1] (1960s-1970s) on studying DWs for storage devices focused on bubble-domain materials, that are magnetic systems with a perpendicular magnetic anisotropy (PMA), i.e., magnetized perpendicular to the plane of the film. They comprise mainly of ferrimagnetic materials such as garnets[2] or rare-earth transition metal alloys[3, 4]. Proposals to store and manipulate information in the form of bubble-domains involved the use of magnetic field gradients. In 1996, Berger[5] and Slonczweski[6] laid the theoretical groundwork for the excitation of magnetization dynamics by spin-transfer effects from the current, different from the effect of Oersted field. Advances in

lithography and thin film deposition enabled the realization of these effects when it became possible to fabricate nanowires ( $<300\text{nm}$ ) made out of deposited magnetic films which can be thin enough to apply reasonable levels of current densities ( $10^8 \text{ A/cm}^2$ ) through it. In such nanowires, DWs could be moved or shifted concurrently with the aid of currents through spin-transfer torques. A number of memory[7, 8] and logic[9] devices have been proposed on this concept. Amongst them, one such concept is the racetrack memory.

## 1.2 Domain walls for racetrack memory

Magnetic storage devices are based on the principle that information can be stored in the orientation of a magnetic region, such that the two distinct possible magnetic orientations represent bits of "0" and "1". The ability to manipulate these magnetic states by either current or field and then read them using an appropriate sensing device such as a magnetic tunnel junction[10, 11] (MTJ) is what magnetic hard disk drives are based on. Switching between these two possible states can also be done using controlled manipulation of magnetic domain walls[12]. In a simple example of this concept (Fig. 1.1), one can imagine a small nanowire, in which a domain wall has been created. By applying current pulses, the magnetization inside the nanowire can be switched from one direction to another, which can be read using an MTJ sensing device.

Racetrack memory[13, 14], an extended version of this concept suitable for mass-storage involves storing multiple bits of information in the same nanowire using DWs. A series of magnetic domains in a nanowire can thus represent a stream of information. DWs that exist between these magnetic domains can be driven by sending nanosecond current pulses. As DWs move together in a lock-step motion,

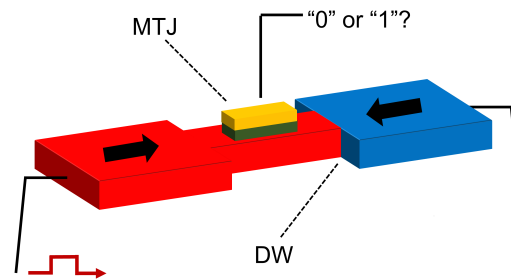


FIGURE 1.1: A one-bit DW-based memory device.

the encoded pattern can be sent back and forth to a location on the nanowire where it can be read or rewritten. By fabricating such nanowires vertically, or in three-dimensions, one can envision an ultra-dense, fast form of memory with no mechanically moving components. Studies into the current-driven motion of DWs is relevant for the technological implementation of such a device. In particular, one topic that has been largely ignored is the motion of DWs in curved geometries. In this thesis, we perform experiments in order to understand the effect of curvature on the motion and discuss its impact on the operation of a racetrack memory device.

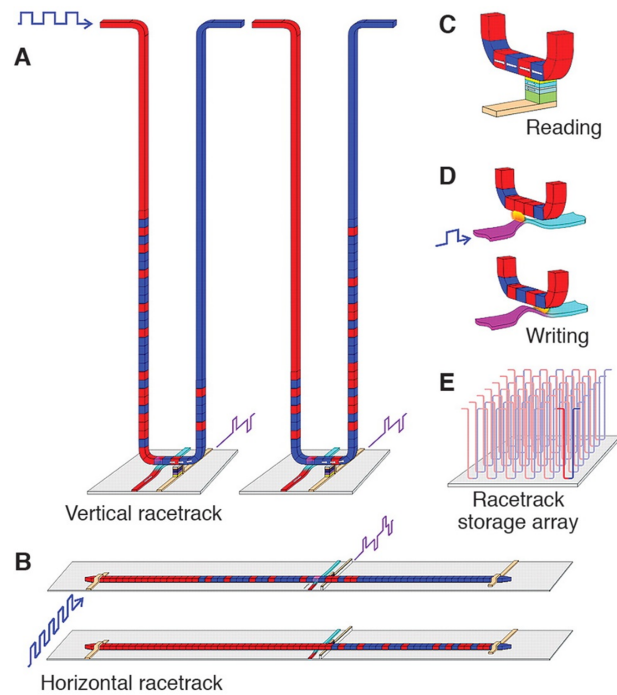


FIGURE 1.2: (a) Racetrack memory in the vertical configuration designed in the form of a U-shaped magnetic nanowire mounted on the surface of the substrate. This configuration gives the highest density. (b) Horizontal configuration which is easier to fabricate. (c) Data reading is done by sensing the magnetic state using an MTJ. (d) Data can be written by producing fringing fields on the nanowire through currents in an adjacent contact line. (e) Arrays of racetracks that can achieve high-density storage. Taken from [13].

### 1.3 Scope of the thesis

Chapter 2 gives a brief introduction to DWs and their dynamics.

Chapter 3 includes a discussion on the experimental methods and techniques used to fabricate magnetic nanowires and perform domain wall velocity measurements.

Chapter 4 consists of experimental work showing that the current-induced motion of DWs can be dramatically altered in a curved nanowire depending on the curvature.

Chapter 5 discusses simulation results from an analytical model that was developed to explain the experimental results obtained in Chapter 4 and to unravel the physical mechanism which influences the speed of a domain wall in a curved wire. We also show that the curvature plays no role in the motion of DWs in a synthetic antiferromagnetic nanowire.

Chapter 6 discusses the use of curvature to perform domain sorting operation in a Y-shaped device.

Chapter 7 summarizes the findings of this thesis and scope for future experiments.





# Chapter 2

## Background

*The properties and dynamics of domain walls arise from a host of interesting and competing interactions. In this chapter, we briefly cover the basics of magnetism that includes a discussion on the way domain walls are created, and the different structures they exhibit. We also review the different mechanisms that can be used to control domain walls - through external fields, conventional spin-transfer torques or spin-orbit torques that arise from spin-orbit coupling interactions in a magnetic heterostructure.*

### 2.1 Introduction to Magnetism and Domain Walls

Electrons as elementary particles not only possess charge, but also a *spin* that makes it behave like a tiny magnet. But unlike a charged spinning top from classical mechanics, the orientation of a spin is quantized and can only point in two directions. The quantized angular momentum associated with an electron's spin is,  $s = \frac{1}{2}\hbar$ . In most materials, these spins orient themselves randomly and

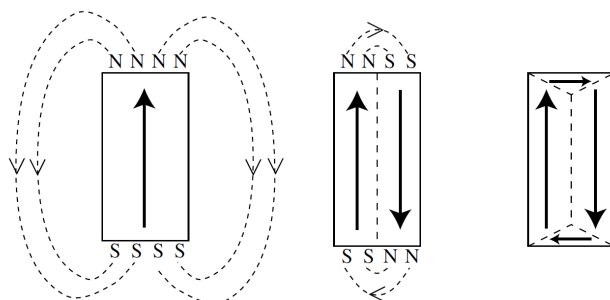


FIGURE 2.1: Reduction of the magnetostatic energy in a ferromagnet by the process of domain formation, adapted from [15].

as a result, the net magnetic moment of that material is zero. In some class of materials, these spins orient themselves in the same direction resulting in a non-zero net magnetic moment. These materials are known as ferromagnetic materials.

The presence of exchange interaction - a quantum mechanical phenomenon - causes spins in ferromagnetic materials to be aligned in the same direction. If exchange was the sole interaction present in ferromagnetic materials, one could expect them to be composed of a single domain with all the moments pointing in the same direction. Instead, it is composed of subunits of uniform magnetization known as magnetic domains. Apart from exchange contributions, there are a number of other factors which contribute to the total magnetic energy and determine the magnetic structure of a ferromagnet. Amongst those, anisotropy energy governs the orientation or axis along which alignment of spins is energetically favourable. Magnetostatic interactions typically govern the process of domain formation. A uniformly magnetized material such as shown in Fig. 2.1 has poles at the ends that lead to demagnetizing fields. The demagnetizing energy can be reduced by formation of multiple domains until this process is no longer favorable due to an increase in exchange energy.

At first glance, it may seem that the magnetization abruptly rotates at the boundary between two domains, but a microscopic examination will reveal that there is

a more gradual transition. This transition region is known as a domain wall (DW) and inside a DW, magnetic moments show a gradual rotation from the direction of one domain to another[16, 17]. Thus, a DW has its own internal magnetic structure as well. The width of a DW transition is determined by the competition between the exchange energy and the anisotropy energy and is given by  $\pi\Delta$ .

$$\Delta = \sqrt{\frac{A}{K_{eff}}}$$

$A$ , the exchange stiffness constant, is a measure of the strength of exchange interaction. The anisotropy energy, is given by  $K_{eff}$ . A larger exchange energy results in wider domain walls as the adjacent magnetic moments prefer to be as parallel as possible. A larger anisotropy energy results in narrower domain walls, as misalignment with the anisotropy axes of the material costs energy.

In addition, the arrangement of moments inside a DW can take different forms depending upon the interplay between anisotropy, demagnetizing (arising from magnetostatic interactions) and exchange energies. Magnetic thin films made out of materials which do not have any significant form of anisotropy contribution except from those arising from magnetostatic interactions have moments pointing in the plane of the film and are called as having in-plane magnetic anisotropy (IPA). In nanowires made out of such films, DWs are usually formed as vortex or transverse DWs[18, 19, 20]. Permalloy ( $\text{Ni}_{81}\text{Fe}_{19}$ ) is one material used to grow in-plane magnetized thin films. On the other hand, some materials possess an additional source of anisotropy (either arising from interfacial, magnetocrystalline or magneto-elastic contributions) which causes the moments to point perpendicular to the plane of the film. Such materials, are known as having perpendicular magnetic anisotropy (PMA)[21] and are typically found in layered structures of a transition magnetic metal and non-magnetic heavy element, e.g. Co/Pd[22] and

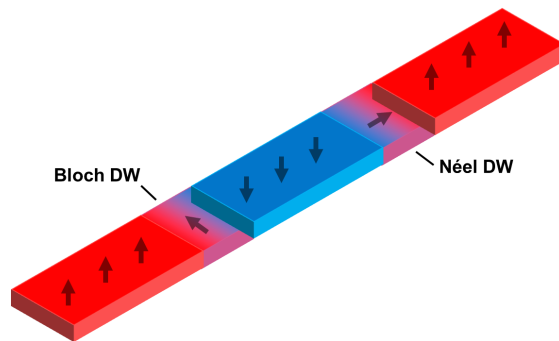


FIGURE 2.2: Néel DW and Bloch-type DWs formed in a magnetic nanowire with PMA.

Co/Pt[23]. The work done in this thesis focuses specifically on DWs formed in PMA systems and these DWs can generally exist in two configurations: Néel DW or Bloch DW. In a Néel DW, the moments rotate in the plane of the DW, whereas for a Bloch DW, the moments rotate out of the plane of the DW. Thus, in the case of a Néel DW, the magnetization in the middle of the DW points along the nanowire length, whereas for a Bloch DW, it points orthogonal to the nanowire in the plane of the film. This is shown schematically in Fig. 2.2.

In a magnetic nanowire, the Bloch-type DW is generally favorable due to magnetostatic interactions. However, for a given thickness, it is possible to transition to a Néel type configuration by making nanowire narrower, thus changing its aspect ratio[24, 25, 26, 27]. This change occurs because the rotation of moments along the length of the nanowire becomes energetically favorable over a rotation orthogonal to it. More recently, it has been shown that Néel-type DWs can also be stabilized through another mechanism known as Dzyaloshinskii-Moriya interaction.

## 2.2 Dzyaloshinskii-Moriya Exchange Interaction

The exchange interaction responsible for ferromagnetism discussed earlier is also known as Heisenberg exchange interaction. It is a form of symmetric exchange whose Hamiltonian is written as :

$$\mathcal{H} = -J\vec{S}_1 \cdot \vec{S}_2$$

Here,  $J$  is the strength of exchange interaction between two adjacent spins  $S_1$  and  $S_2$ . It follows that their energy is lowest when they are parallel (for  $J > 0$ , ferromagnetic case) or anti-parallel (for  $J < 0$ , antiferromagnetic case). There is also another form of exchange, known as Dzyaloshinskii-Moriya Exchange Interaction[28, 29] (DMI) whose Hamiltonian is defined as:

$$\mathcal{H} = -D[\vec{S}_1 \times \vec{S}_2]$$

DMI energetically favors an angle between  $S_1$  to  $S_2$ , but the sense of rotation is determined by the sign of  $D$ , which is the DMI energy constant. One particular sense of rotation is favorable over the other, hence it is an antisymmetric exchange. This type of exchange was first proposed by Dzyaloshinskii to explain weak ferromagnetism in bulk  $\text{Fe}_2\text{O}_3$ [28] arising from the lack of inversion symmetry (from the non-centrosymmetric lattice) in the presence of spin-orbit coupling.

In 2007, a report by Bode et al.[30] presented experimental evidence of a chiral magnetic order induced by a DMI contribution arising from interface. Using a spin-polarized scanning tunneling microscope, they observed a left-rotating spin cycloid in a monolayer of manganese grown on a tungsten (110) substrate. In this special case, the lack of structural inversion asymmetry in the presence of spin-orbit

coupling arises from the interface between an ultrathin heavy-metal/ferromagnet layer. There were subsequent experimental studies[31, 32, 33] probing the nature of DMI in such structures but a major development took place when Miron et al. reported fast current-driven domain wall motion in an ultrathin PMA heterostructure[34] made out of Pt/Co/AlO<sub>x</sub><sup>1</sup>. The authors attributed the high speeds (upto 400m/s) to the stabilization of the Bloch wall configuration by Rashba fields generated during current-driven motion. A different mechanism for fast DW speeds was proposed by Thiaville et al.[35] who pointed out that the spin accumulation generated from the spin Hall effect (SHE) in Pt can efficiently move Néel DWs stabilized through DMI. A sufficient strength of  $D$  can stabilize Néel DWs even in wide wires, thus overcoming magnetostatic interactions. The DMI generates a local longitudinal field at the DW of a chiral nature. Thus, the rotation of the magnetization inside a DW from an up (or down)<sup>2</sup> to a down( or up) domain has a fixed handedness which causes all DWs to move in the same direction under current, a feature useful for racetrack memory(Fig. 2.3). Experiments by Ryu et al.[36], and Emori et al.[37] confirmed the presence of this chiral field by performing longitudinal field dependence of DW motion in such structures. Upon the application of a longitudinal field, equal in magnitude and opposite in direction to the internal DMI field at the DW, the DW reverts to a Bloch DW leading to the absence of current-driven motion. The presence of interfacial DMI in conjunction with a ultrathin magnetic layer has been confirmed from several heavy metals: Pt[36, 37], Ta[37, 38], Pd[39], W[38], Hf[38], Ir[39].

---

<sup>1</sup>When a film structure is described, the layer on the left is grown to the bottom of the one on the right.

<sup>2</sup>In this thesis, when the directions up or down refer to the orientation of a magnetic domain, up means a vector pointing orthogonal to the surface of film in a direction away from the plane of the film, and down means a vector opposite of that. Directions up and down may also be represented using the symbols  $\odot$  or  $\uparrow$  and  $\otimes$  or  $\downarrow$ , respectively.

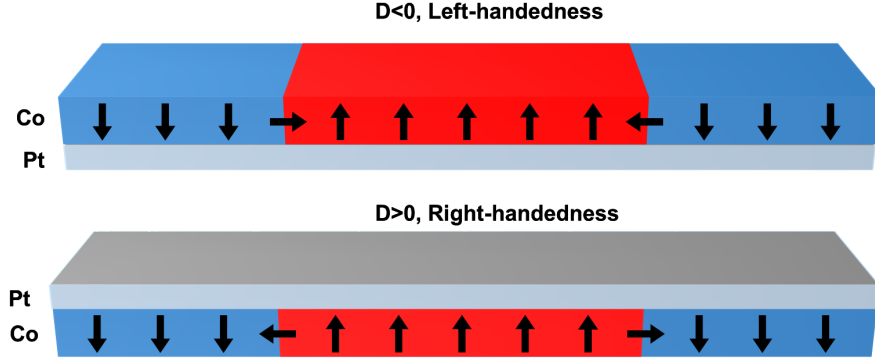


FIGURE 2.3: Top: For a Pt/Co structure,  $D < 0$ , which leads to the formation of left-handed chiral DWs ( $\uparrow \leftarrow \downarrow$  or  $\downarrow \rightarrow \uparrow$ ). Bottom: by making an inverse Co/Pt structure, the sign of  $D$  can be reversed leading to right-handed chiral DW. ( $\uparrow \rightarrow \downarrow$  or  $\downarrow \leftarrow \uparrow$ )

## 2.3 Domain-Wall Dynamics

In this section, we describe the Landau-Lifshitz-Gilbert (LLG) equation [40] which governs the domain wall dynamics. Magnetization dynamics are grounded on the mechanical law that the time-rate of angular momentum change is proportional to the torque,  $\vec{T}$ . For any unit volume of the magnetic material with where  $\vec{m}$  is the unit vector, the equation of the motion can be written as:

$$\frac{\partial \vec{m}}{\partial t} = -\vec{T} \gamma$$

For field-driven dynamics, the  $\vec{m}$  is acted upon by an effective field,  $\vec{H}_{eff}$  to produce the torque,  $\vec{T}$

$$\vec{T} = \vec{m} \times \vec{H}_{eff}$$

This effective field includes the effects of ferromagnetic exchange, anisotropy, magnetostatics as well as any external field applied on the magnetic material. In addition, an additional field acts proportional but in opposition to the rate of change of angular momentum. This field is the phenomenological representation of dissipative effects and can be considered analogous to the role of friction in mechanics.

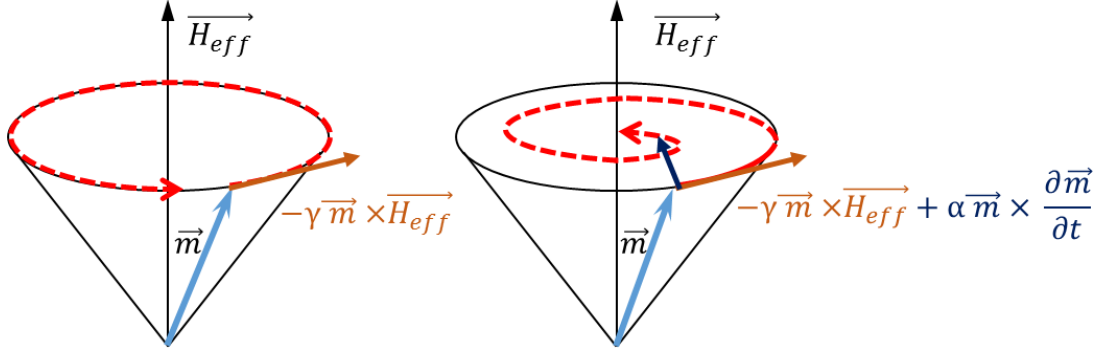


FIGURE 2.4: Schematic illustrating the evolution of magnetization under the presence of an effective field (left). Without the presence of a damping term (right) it continuously precesses and with its inclusion, it eventually lines up in the field direction.

Including this term, the equation of motion can be represented simply as

$$\frac{\partial \vec{m}}{\partial t} = -\gamma \vec{m} \times \vec{H}_{eff} + \alpha \vec{m} \times \frac{\partial \vec{m}}{\partial t}$$

This describes the LLG equation and the strength of the dissipative effect is measured by the dimensionless parameter,  $\alpha$  which is called the Gilbert damping constant [41].

### 2.3.1 Spin transfer torque terms

Electrons traveling in a material not only carry charge but also spin. In non-ferromagnetic samples, the conduction electrons have no net spin polarization. In ferromagnetic samples, conduction electrons can become partially spin-polarized due to the spin-based interactions between electrons and magnetic moments of the material. In other words, a majority of conduction electrons have spin oriented in the direction of the magnetization of the material. The degree of spin-polarization



$P$  can be quantified as

$$P = \frac{\sigma_{\uparrow} - \sigma_{\downarrow}}{\sigma_{\uparrow} + \sigma_{\downarrow}}$$

where  $\sigma_{\uparrow(\downarrow)}$  denotes the conductivity of electrons with spins aligned parallel (anti-parallel) to the magnetization in the material. 3d transition metal ferromagnets (Fe, Co and Ni) and their alloys exhibit  $P > 0$ .

The spin of a conduction electron not only aligns with the magnetization within the material, but also perturbs it when there is a mismatch of alignment between them. This happens through spin-transfer torque (STT)[42] which was proposed by Berger[43] in 1978 as a mechanism to drive DWs through electric currents. In the 1980s, Berger's group also experimentally observed domain wall motion in thin ferromagnetic films[44, 45] although the currents required to drive them were quite high ( $\sim 45$  A) owing to the mm-wide structures of the film. With the advances in nanofabrication techniques, studies by various groups[46, 47, 48] demonstrated domain wall motion in narrower strips with currents of few mA and below.

The originally proposed mechanism describes the motion of a DW as arising from the transfer of angular momentum from the conduction electrons to the localized magnetic moments. As the spin-polarized electrons pass through a DW, the spin tracks the rotating magnetization inside a DW adiabatically. During this process, the net angular momentum of the spin-polarized electron and the magnetic moment has to be conserved. The change in the angular momentum of the spin-polarized electron is transferred to the magnetization inside the DW and as a result, the DW moves in the electron flow direction. This type of torque is known as adiabatic STT. Incorporating the effect of this torque, the LLG equation[49] becomes:

$$\frac{\overrightarrow{\partial m}}{\partial t} = -\gamma \overrightarrow{m} \times \overrightarrow{H_{eff}} + \alpha \overrightarrow{m} \times \frac{\overrightarrow{\partial m}}{\partial t} - u(\overrightarrow{j} \cdot \nabla) \overrightarrow{m}$$

The term  $-u(\vec{j} \cdot \nabla)\vec{m}$  represents the contribution of adiabatic STT.  $u$  parameterizes the spin drift velocity, which is  $u = \frac{u_B PJ}{eM_s}$ .  $\vec{j}$  is the unit vector for the direction of the current flow,  $u_B$  is the Bohr magnetron,  $e$  the electron charge,  $J$  the current density and  $M_s$  is the saturation magnetization. When the conduction electron spins mistrack the local moments inside a DW, the electrons can be reflected from its original direction of motion leading to a DW motion through linear momentum transfer. The torque resulting from such a mechanism is known as non-adiabatic STT[50]. It is parameterized through  $\beta$ , and the strength of non-adiabatic STT is measured in terms of the ratio,  $\frac{\beta}{\alpha}$ .

$$\frac{\partial \vec{m}}{\partial t} = -\gamma \vec{m} \times \overrightarrow{H_{eff}} + \alpha \vec{m} \times \frac{\partial \vec{m}}{\partial t} - u(\vec{j} \cdot \nabla)\vec{m} + \beta u \vec{m} \times (\vec{j} \cdot \nabla)\vec{m}$$

### 2.3.2 Torques arising from spin-orbit interactions

Polarization of conduction electrons in a magnetic material is one mechanism through which spin currents can be generated that can be utilized for generating spin torques for manipulation of magnetic moments. The conversion of charge to spin currents can happen through another process arising from spin-orbit interactions. In some bilayer systems with a non-magnetic layer/ferromagnetic layer interface (NM/FM), the passage of charge currents in the non-magnetic layer can give rise to spin currents that can get absorbed by the adjacent magnetic layer leading to spin torques. The mechanisms leading to such spin torques can be classified as mainly arising from either the spin Hall effect (SHE) or the Rashba effect. The Rashba effect is an interfacial effect whereas SHE is a bulk effect. The Rashba effect[51, 52, 53] arises in magnetic heterostructures with structural inversion asymmetry. For example, in a structure like Pt/Co/AlO<sub>x</sub>[34, 54], the

presence of a heavy metal on one end, and an oxide on the other creates an asymmetric potential that leads to an electric field perpendicular to the plane of the interface. Electrons travelling through the ferromagnetic layer experience the electric field as a magnetic field due to relativistic effects and can tilt[55] resulting in a torque on the magnetization. Rashba effect generally result in a "field-like" torque although a "damping-like" component has also been predicted. We ignore the effect of Rashba torques in discussions pertaining to our experiments as in the systems we are interested in, it has been found to be of a negligible order[37] when compared to the spin Hall torques.

The spin Hall torque in bilayer systems arises from the absorption of the spin currents generated in the adjoining NM layer through the SHE. When an electric current is passed through the NM layer, a transverse spin current is generated with a direction of polarization orthogonal to the direction of the charge current as well as spin current. The SHE is similar to Anomalous Hall effect (AHE)[56] in the sense that spin-orbit coupling leads to a deflection of charge carriers depending on the spin orientation. In a ferromagnetic material, the majority and minority spin carriers have different populations, which lead to a transverse voltage that can be detected. In the case of a NM, there is no transverse voltage as there are equal carriers of both spin polarizations. SHE was originally proposed in 1971 by Dyakanov and Perel[57] as an extrinsic mechanism. The extrinsic mechanism depends on the spin-orbit interaction of electrons with impurities and can be classified as due to skew-scattering or side-jump. In the skew-scattering mechanism, an electron approaching a scattering centre experiences a gradient in magnetic field (owing to relativistic effects). As a result of this interaction, there is an asymmetric scattering where electrons with different spin polarizations acquire a transverse velocity in opposite directions. Also known as Mott scattering[58], this is a well-known effect used to induce polarization from a beam of unpolarized

electrons. In the case of side-jump scattering, spin-dependent acceleration or deceleration takes place during a scattering event, induced by an effective magnetic field. Consequently, there is a net transverse displacement upon several scattering events. This transverse displacement is spin-dependent[59]. Spin Hall effect can also arise based on an mechanism of an intrinsic nature was made by Murakami et al.[60] and Sinova et al.[61]. The second mechanism is due to intrinsic properties of the material, where the band structure in the presence of spin-orbit interactions can lead to spin Hall conductivity.

Early means of detection of SHE were accomplished by using Kerr microscopy to detect spin polarization accumulation at the edges of a channel[62]. Since then, the methods of detection evolved considerably to include various other detection techniques such as: detection of inverse Hall effect[63, 64, 65], spin torque ferromagnetic resonance[66] and harmonic Hall voltage measurements[67, 68]. The demonstration of nanomagnet switching through SHE in IPA[69], and PMA systems[70] made SHE interesting technologically, particularly for current-induced switching in MRAM devices. By having a source of spin current, that is independent of the magnetic layer, SHE and other spin-orbit related torques provide an additional degree of flexibility in designing devices with lower power consumption and better performance.

The efficiency of charge-to-spin conversion is parameterized by spin Hall angle,  $\theta_{SHE}$  which is defined as  $\theta_{SHE} = \frac{J_s}{J}$ . Here,  $J_s$  is the spin current density that is generated from a charge current density,  $J$ . Many 5d group NM elements are known to show reasonable values of  $\theta_{SHE}$  such as Pt[66, 71, 72], Ta[69] and W[73, 74, 75]. The addition of spin Hall torque term makes the final equation as:

$$\begin{aligned} \frac{\partial \vec{m}}{\partial t} = & -\gamma \vec{m} \times \overrightarrow{H_{eff}} + \alpha \vec{m} \times \frac{\partial \vec{m}}{\partial t} - u(\vec{j} \cdot \nabla) \vec{m} + \beta u \vec{m} \times (\vec{j} \cdot \nabla) \vec{m} \\ & + \vec{m} \times (\vec{m} \times H_{SHE}(\hat{z} \times \vec{j})) \end{aligned} \quad (2.1)$$

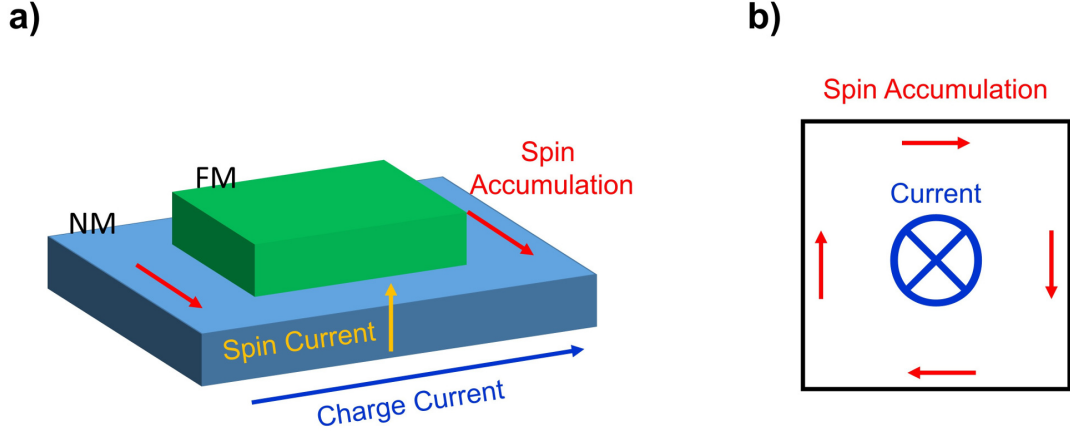


FIGURE 2.5: Spin Hall effect in a bilayer system. (a) Passage of charge current in a non-magnetic layer with SHE such as Pt, leads to a transverse spin current with a direction of spin accumulation orthogonal to both. This spin accumulation can be absorbed by the adjacent magnetic layer to produce a spin torque. (b) The spin accumulation is generated along all the four sides of the SHE material.

$H_{SHE}$  parameterizes the effective spin Hall field generated through the spin Hall effect and can be calculated as :

$$H_{SHE} = \frac{\hbar\theta_{SHE}J}{2eM_s t}$$

Here,  $t$  is the thickness of the NM layer which is responsible for SHE. Eq. 2.1 which includes the sum of all contributions that can contribute to DW dynamics is used in later chapters to derive the equations of motions for DWs under the influence of different torques. Here, in this section we describe intuitively the mechanism that is responsible for DW motion of chiral DWs. The DMI field which stabilizes the Néel configuration enforces a chirality such that the magnetization at the centre of DW always points from one magnetization direction to another. For the case of Pt/Co structure (Fig. 2.6a), the DW magnetization,  $\vec{m}_{DW}$  points towards the up-pointing domain when at rest. When a current is applied, the spin accumulation generated through spin Hall effect of platinum applies a torque on  $\vec{m}_{DW}$  so as

---

to cant it transverse to the wire direction. Consequently, the DMI field which likes to stabilize the Néel configuration applies a restoring torque on the  $\vec{m}_{DW}$  that produces an out-of-plane rotation and consequently motion of the DW. Note that since the chirality of the DW is locked, the out-of-plane rotational torque is opposite for an  $\uparrow\downarrow$  vs  $\downarrow\uparrow$  DW. Consequently, this leads to the motion of DWs in the same direction, which is the basic operating principle of a racetrack memory device.

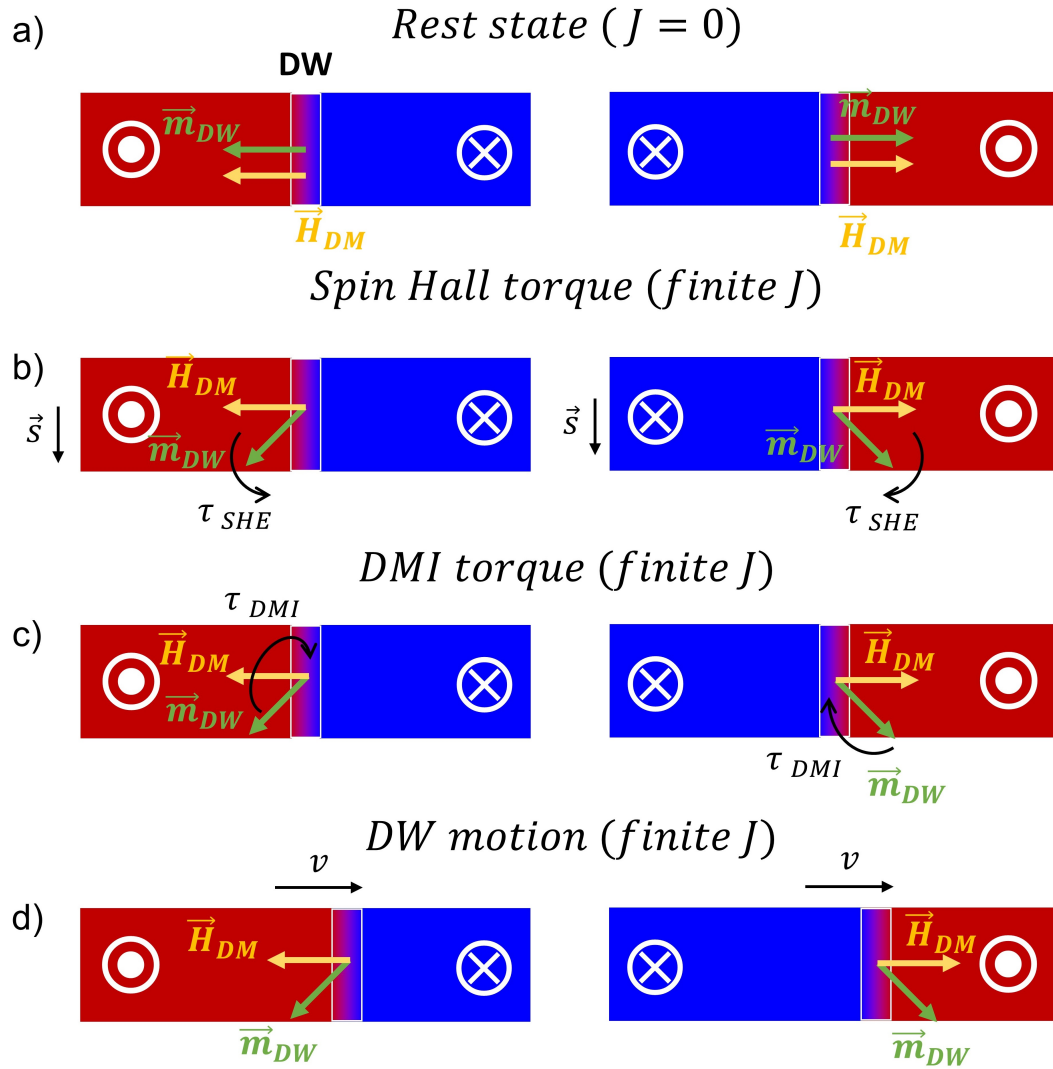


FIGURE 2.6: Domain wall motion arising from interplay of SHE-derived and DMI torques as seen from a top-bottom viewpoint. (a) At rest,  $\vec{m}_{DW}$  assumes a Néel configuration. (b) Passage of current through an underlayer such as Pt leads to a SHE-derived spin accumulation with direction transverse to the wire. This causes a torque on  $\vec{m}_{DW}$ . (c) As  $\vec{m}_{DW}$  veers away from its Néel configuration, DMI field acts to restore its previous configuration leading to an out-of-plane torque. (d) The direction of out-of-plane DMI torque is opposite for the different DW configurations yet the direction of motion is the same.





# Chapter 3

## Experimental Methods

*This chapter includes an introduction to the experimental methods and techniques used in this thesis. It includes details of film growth, fabrication and measurement techniques used for detecting domain wall motion.*

### 3.1 Sample Preparation

The thin film structures studied in this thesis were grown using magnetron sputtering on Si(100) wafers with a 250 Å thick capping layer of SiO<sub>2</sub>. The typical stack[36] for observing domain wall motion in PMA magnetic racetracks with a single ultrathin ferromagnetic layer was : 100 AlO<sub>x</sub>/20 TaN/15 Pt/3 Co/7 Ni/1.5 Co/50 TaN<sup>1</sup>. Based on our experiments, the seed layer of 100 AlO<sub>x</sub>/20 TaN plays a key role in inducing strong PMA in the magnetic layers. The seed layer was deposited by first growing AlO<sub>x</sub> by reactive magnetron sputtering in an Ar/O<sub>2</sub> (97/3) mixture followed by the growth of TaN by reactive sputtering Ta in an

---

<sup>1</sup>Numbers indicate the individual thicknesses of the layers in Ångstrom units.

Ar/N<sub>2</sub> (90/10) mixture. The rest of the magnetic heterostructure is then deposited before growing a capping layer of TaN in order to prevent further oxidation. The thicknesses of the layers grown is determined by measurements of thick calibration films using a thin film profilometer. Some variations of this structure with varying Pt thicknesses on the top and the bottom interface adjoining the magnetic layer were also grown[36].

The device structures were fabricated using standard photolithographic techniques and Ar ion milling as illustrated in Fig. 3.1. First, a layer of SPR photoresist (670 nm) is spin coated on the sample. Using photolithography, patterns are created in the resist which give definition to the device structures during the Ar-ion milling process. After milling, a layer of AlO<sub>x</sub> is deposited in order to refill the etched material followed by a subsequent step of lift-off using a NMP solvent.

In some cases, gold contact pads are deposited onto the patterned devices to provide a bigger surface area for making contact using wire bonding.

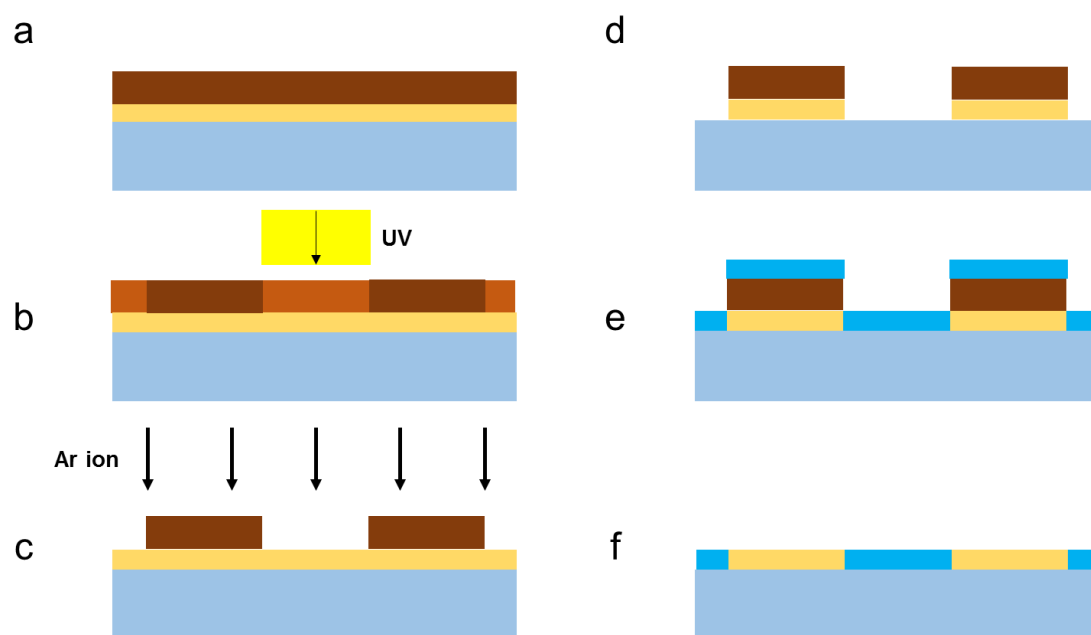


FIGURE 3.1: Procedure to fabricate device structures using photolithography: (a) SPR photoresist spin-coated over film, (b) SPR photoresist exposed to UV photolithography, (c) after use of a chemical developer, unexposed photoresist acts as the hard mask for Ar ions being bombarded, (d) after ion milling, (e)  $\text{AlO}_x$  refill, and finally (f) lift-off process.

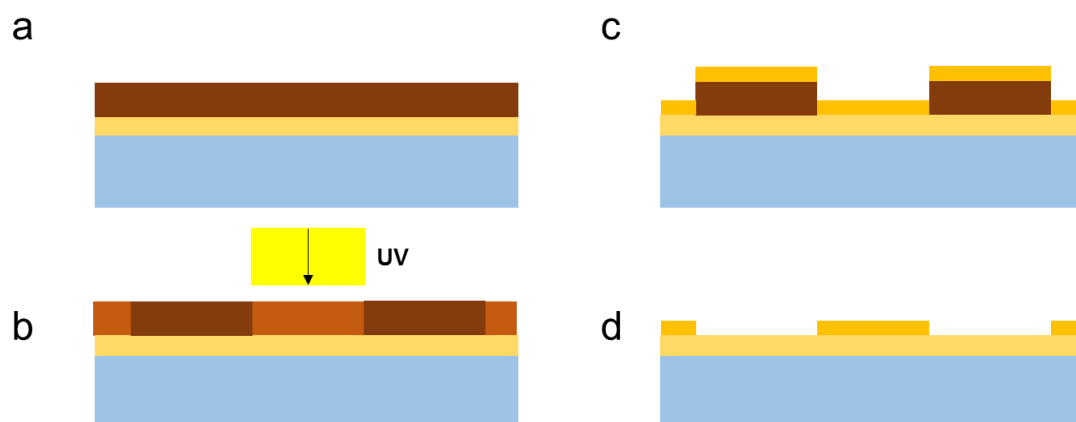


FIGURE 3.2: Deposition of gold-contact pad by photolithography, sputtered deposition of gold and subsequent lift-off.

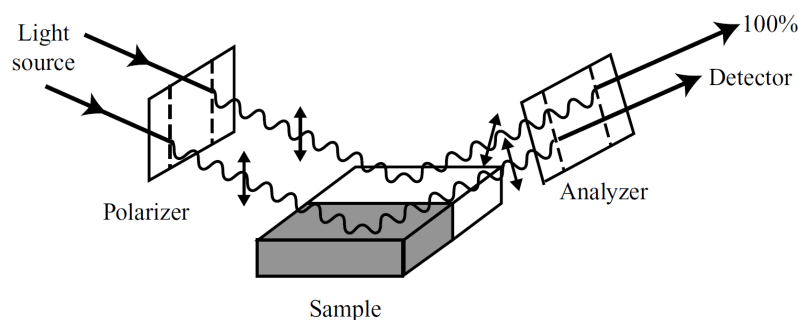


FIGURE 3.3: Plane of polarization rotation for an incident beam of linearly polarized light upon reflection from a magnetic sample. Magnetic regions pointing differently (grey and white) produce different rotations in the reflected beam[15].

## 3.2 Magneto-Optical Kerr Effect

Magneto-optical detection of domain structures can be done either using reflection or transmission of linearly polarized light incident on the surface of a magnetic material. The former is called the Faraday effect while the latter is called the Kerr effect. Both are based on the principle that an interaction between the magnetization in the material and the incident polarized light can lead to a small rotation of the plane of polarization which can be detected by passing the reflected or transmitted beam through an analyzer that is set cross-polarized to the polarizer of the incident beam.

The strength of such magneto-optical effects depends on the magnitude as well as the orientation of the magnetization. The physics underlying Faraday and Kerr effect can be understood by considering that linearly polarized light can be decomposed into two oppositely polarized circular polarizations. Photons carry angular momentum of the same magnitude but opposite signs,  $L = \pm 1$  (in units of  $\hbar$ ) for the left and right circularly polarized light, when projected along the direction of propagation.

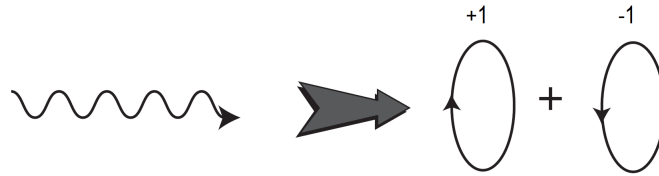


FIGURE 3.4: Linearly polarized light can be resolved into circularly polarized light with opposite polarizations[15].

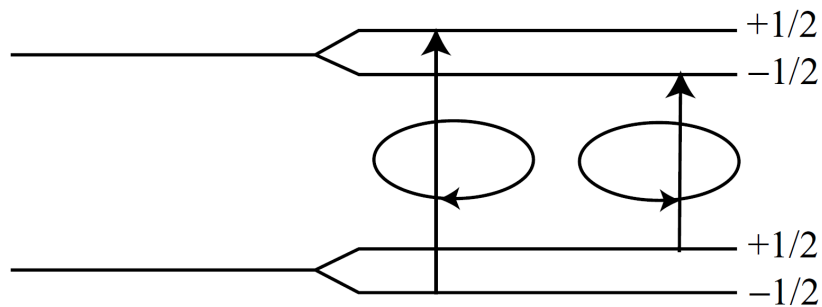


FIGURE 3.5: Electronic excitations corresponding to the two the opposite polarizations of circularly polarized light[15].

In a magnetic material, these photons can impart angular momentum to electrons and cause excitation between the two electronic energy levels,  $S = \pm\frac{1}{2}$  which arise from Zeeman splitting. Thus, an electron at  $S = -\frac{1}{2}$  level absorbs a photon with  $L = +1$  to jump to the  $S = +\frac{1}{2}$  state, while an electron at  $S = +\frac{1}{2}$  level absorbs a photon  $L = -1$  to jump to the  $S = -\frac{1}{2}$  state. This is illustrated in Fig. 3.5

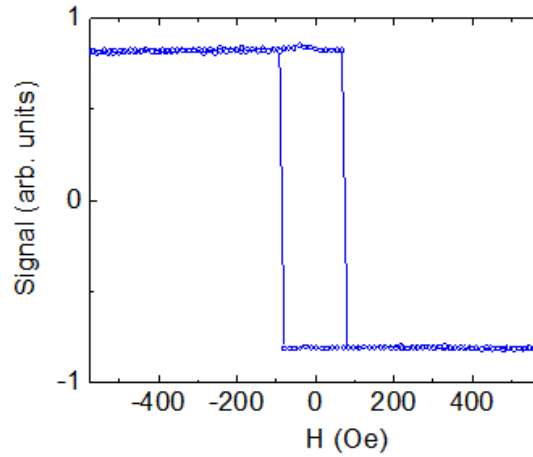


FIGURE 3.6: p-MOKE hysteresis loop showing switching between the two magnetization states in the presence of field perpendicular to the plane of the film.

### 3.3 Measurements of DW motion

The Kerr effect can be used to image magnetic domain structures by employing a Kerr microscope. Kerr microscopy can be done using a wide-field microscope or a laser-scanning technique. In the former, a regular microscope is used which is able to provide an image immediately while in the later, a laser spot scans sequentially the different regions of the sample to form an image. In our studies, we use a wide-field Kerr microscope. Often, there are irregularities on the surface of a sample which contribute to an undesirable contrast of a non-magnetic origin. In some cases, the difference in contrast produced between the up-pointing and down-pointing domains may not be sufficient. Both problems can be eliminated using Kerr microscopy in a differential mode. In this method, a reference image is first captured and then stored digitally. The subsequent feed from the camera is then digitally subtracted from this reference image. Unless there is a drift in the feed, the non-magnetic features get subtracted away and only magnetic features appear in the processed images. These magnetic features only appear if there is

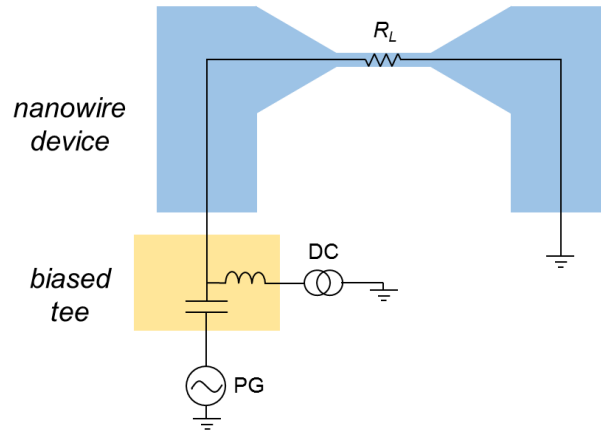


FIGURE 3.7: Circuit diagram of a nanowire device used for DW motion measurements

a change in magnetization compared to the reference image. If an up-pointing domain gets displaced by a down-pointing domain, we see a bright contrast in the corresponding region. This contrast is dark when a down-domain gets displaced by an up-pointing domain. By averaging and amplification of this signal, the contrast can be further increased[17].

Devices fabricated for DW motion measurements typically have a nanowire<sup>2</sup> that joins two big pads that are used to make electrical connections. Aluminium wire bonds are used to make connections onto the device pads. One of the pads is electrically grounded, while the other one is simultaneously connected to a Tektronix pulse generator and a DC current generator by means of a biased tee. A small current of 10  $\mu\text{A}$  is injected into the device by the DC current generator in order to monitor the device resistance. Electrical pulses of varying pulse lengths and voltages are sent using the pulse generator to induce domain wall motion and the displacement of the DW. Although the motion of a DW happens roughly in the time interval,  $t_p$  - when the current pulse is applied - i.e. in nanoseconds, the

<sup>2</sup>The width of a typical nanowire device used in our domain wall motion experiments is a few  $\mu\text{m}$  but we still refer to it as a nanowire because of its thickness ( $<10\text{nm}$ ).

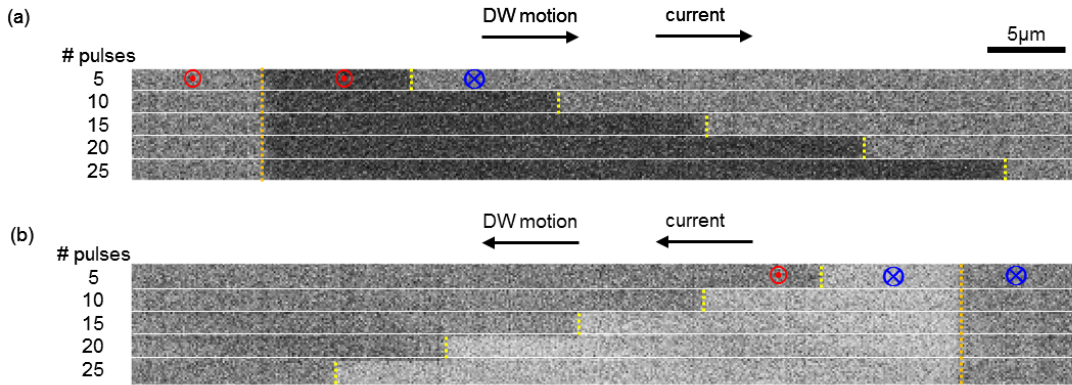


FIGURE 3.8: Kerr images of the current-driven motion of a DW in differential mode upon application of 5, 10, 15, 20 and 25 pulses of 5 ns duration. (a) A DW travelling left-to-right displaces down-pointing regions with up-pointing regions as indicated by the area that appears as a dark contrast. (b) A DW travelling right-to-left displaces up-pointing regions with down-pointing regions as indicated by the area that appears as a bright contrast.

capture rate of the Kerr microscope is in milliseconds, and hence measurements can only be made about the final displacement,  $d$  of the DW after the current has been shut off. Post-facto measurements about the average velocity,  $v$  of a DW can be made in this way as  $v = \frac{d}{t_p}$ .

For all domain wall motion measurements, a DW needs to be injected first. This is done in the following way. Initially, an out-of-plane field is applied to form a single domain in the magnetic device. In order to inject a DW into the nanowire structure, an electrical pulse of a sufficient current density in the presence of an in-plane field is applied to switch the magnetization using spin Hall torques[70, 76]. The magnetization switching is limited to the nanowire region as the current density there is much higher than the adjoining pads due to the geometry of the device. As a result, domain walls are formed on both ends of the nanowire. By the application of current pulses in the presence of an out-of-plane magnetic field, there is an asymmetric expansion of the domain nucleated in the nanowire and



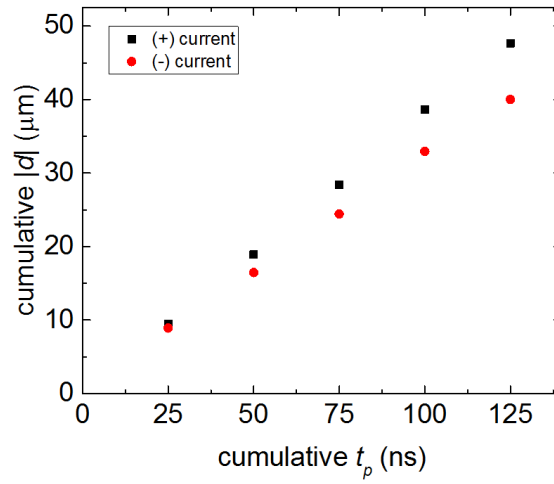


FIGURE 3.9: Plot showing cumulative displacements of DWs vs cumulative time for the measurements performed in Fig. 3.8. A linear fit gives mean  $v$ .

one DW propagates to the pad while the other DW remains in the nanowire. This DW is then used for DW velocity measurements as shown in Fig. 3.8 and 3.9.



# Chapter 4

## Experimental results on the motion of DWs in a curved wire

*Current-driven domain wall motion in thin ferromagnetic layers has been studied extensively over the past decade. This has led to the discovery of suitable material systems as well as newer and more efficient mechanisms for moving domain walls. However, most, if not all of the studies have been limited to the motion of domain walls in straight wires. In order to completely evaluate the racetrack memory device in two and three dimensions, it is also important to consider the effect curvature of a nanowire may have on domain wall motion. In this chapter, we conduct experiments to explore this and find that the curvature of a nanowire can dramatically influence the velocity of domain walls moving through them.<sup>1</sup>*

---

<sup>1</sup>The contents of this chapter have been either adapted or directly taken from my publication: Garg, C., Yang, S.H., Phung, T., Pushp, A. and Parkin, S.S., 2017. Dramatic influence of curvature of nanowire on chiral domain wall velocity. Science advances, 3(5), p.e1602804. Reprinted with permission from AAAS.

## 4.1 Device structure for experiments

Experiments for the understanding of the effect of curvature on the motion of domain walls (DWs) were performed in a U-shaped magnetic nanowire (Fig. 4.1) made from ultrathin Co/Ni/Co sandwiches[36] deposited on a Pt underlayer whose structure has been discussed earlier in Sec. 3.1. In this structure, the Pt underlayer induces perpendicular magnetic anisotropy (PMA) in the Co/Ni/Co sandwich and also gives rise to a Dzyaloshinskii-Moriya interaction (DMI) that stabilizes Néel DWs that are chiral in nature. Thus, DWs are formed at the boundaries between magnetic regions with magnetization pointing out of ( $\odot$ ) and into the plane ( $\otimes$ ) of the nanowire, where the magnetization rotates from ( $\odot$ ) to ( $\otimes$ ) in a plane that is perpendicular to the length of the DW. This rotation can be in a clockwise or counterclockwise direction, which is determined by the sign of the DMI vector. The U-shaped structure has two straight sections joined by a curved nanowire of a width,  $w$ , and mean radius,  $R$ . This design allows the motion of a DW in the straight section to be directly compared to the curved section in the same device. The curvature of a nanowire can be defined as:

$$|\kappa| = \frac{1}{R}$$

The magnitude of the curvature is simply the reciprocal of the radius, whereas the sign of curvature is determined by the direction of motion of a DW. If we consider the DW velocity as a vector that is changing along the arc defined by the magnetic nanowire, then a DW travelling in a clockwise direction is moving along a positive curvature ( $\kappa > 0$ ). Whereas, a DW moving in the anti-clockwise direction can be defined as moving along a negative curvature ( $\kappa < 0$ ). We can also define the curvature of the nanowire by using the current vector but we choose to stick with the DW velocity vector. We assign DWs as either  $\otimes|\odot$  or  $\odot|\otimes$  with regard to

the direction of their motion. DW motion measurements for a particular current density,  $J$ , are made by measuring  $d$  (Fig. 4.2) as a function of various suitable pulse lengths,  $t$ , until a steady state velocity is reached (Fig. 4.3).

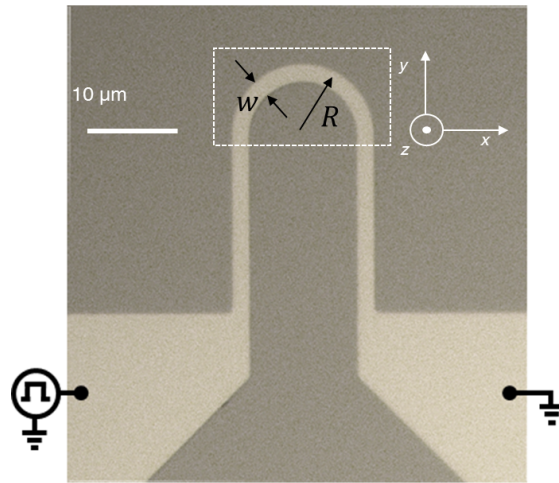


FIGURE 4.1: Optical image of a typical U-shaped device with  $R = 7 \mu\text{m}$  and  $w = 2 \mu\text{m}$ .

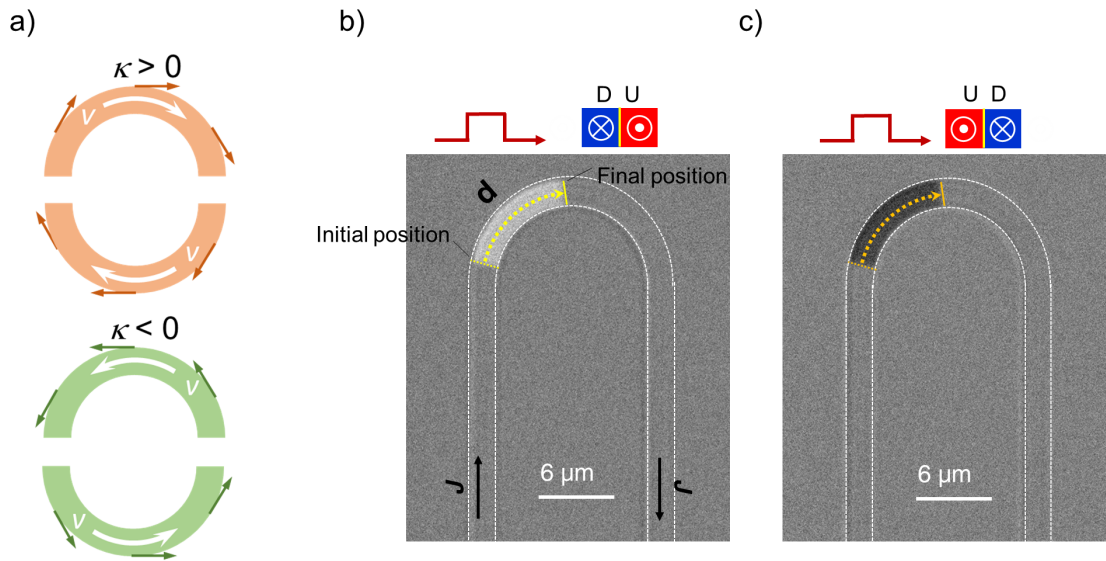


FIGURE 4.2: (a) Cartoon depicting the sign of curvature based on the velocity,  $v$ , of a DW in a curved wire. (b-c) The aftermath of a (b)  $\otimes|\odot$  or (c)  $\odot|\otimes$  DW travelling a distance,  $d$ , along a curved wire upon the application of a current pulse. The distance traversed by the DW appears as a (b) bright or (c) dark region, respectively

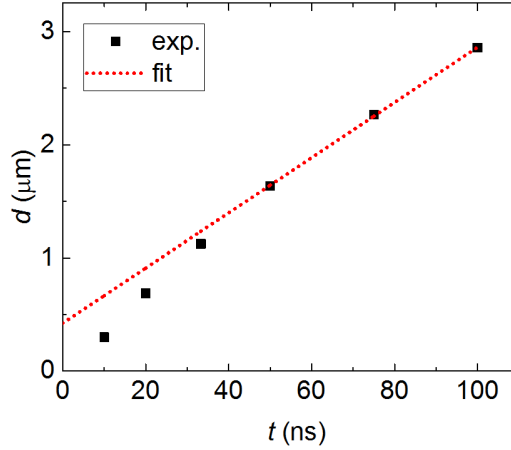


FIGURE 4.3: A  $d$  vs  $t$  plot for a DW moving in a curved wire with a linear fit to it after a steady state velocity has been reached.

## 4.2 Experimental Results

The dependence of  $v$  on the current density,  $J$  is shown in Fig. 4.4 for a device with  $R = 7 \mu\text{m}$  and wire width  $w = 2 \mu\text{m}$ . Four sets of measurements are undertaken corresponding to both signs of curvature for each DW configuration. It is clear that there is a speeding up or slowing down of DWs as they travel in the curved section of the nanowire compared to their motion in a straight wire.  $\odot|\otimes$  DWs along a negative curvature travel at the same higher speed as  $\otimes|\odot$  DWs in a positive curvature. Switching the sign of the curvature causes the corresponding DWs to move much more slowly. The DW speeds for opposite curvatures can differ by more than a factor of 3 as shown in Fig. 4.4.

The disparity in speeds of the two opposite DW configurations can be visualized more vividly by studying the concurrent motion of two neighbouring DWs. Two DWs with varying inter-DW distances are placed inside the curved section of the wire. Subsequently, two current pulses of length 100 ns and a current density of  $0.6 \times 10^8 \text{ A/cm}^2$  were applied to move the DWs. The four panels in Fig. 4.5

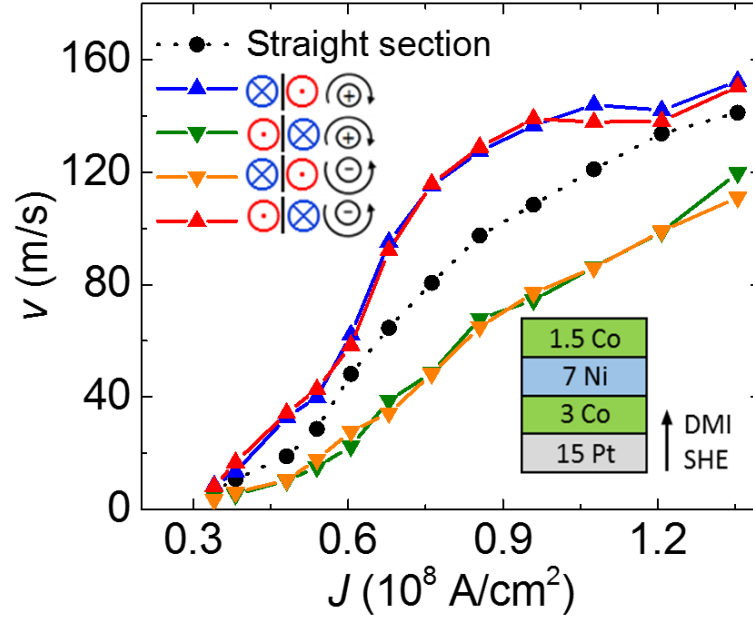


FIGURE 4.4:  $v$  versus  $J$  shows faster or slower DW motion in a curved nanowire ( $R = 7 \mu\text{m}$  and  $w = 2 \mu\text{m}$ ) compared to a straight wire.

correspond to the four cases for  $\odot|\otimes|\odot$  and  $\otimes|\odot|\otimes$  DWs for the two different curvatures. The two DWs are color-coded in each image, and their respective motions are represented by curved arrows of the same corresponding color. In each case, the DWs move at different velocities, which can be seen in the Kerr difference images as an expansion or contraction of the initial spacing between the DWs. Consistent with the single DW data shown in Fig. 4.4, we find that (i)  $\otimes|\odot$  DW with positive curvature moves at the same high speed as the  $\odot|\otimes$  DW with negative curvature (Fig. 4.5, compare top left and bottom right panels) and that (ii)  $\odot|\otimes$  DW with positive curvature moves at the same low speed as the  $\otimes|\odot$  DW with negative curvature (Fig. 4.5 compare top left and bottom right panels).

In Fig. 4.6d-e, we compare similar Co/Ni/Co structures in which variations in thicknesses of the Pt and Co layers at the top and bottom interfaces are used to

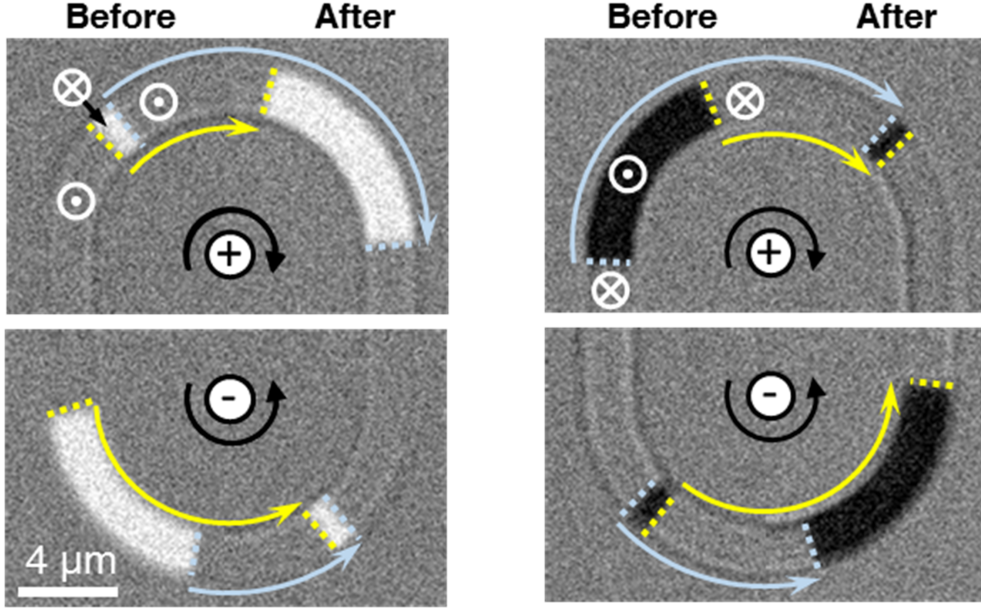


FIGURE 4.5: Representative Kerr images showing the expansion or contraction of a magnetic domain along the positive or negative curvature of a curved nanowire. The Kerr images are taken before and after the application of two 100-ns-long electrical pulses with a current density of  $0.6 \times 10^8$  A/cm<sup>2</sup>. They are overlaid together, and the unedited picture is available in [77]. The yellow (gray) dots indicate the positions of  $\odot|\otimes$  ( $\otimes|\odot$ ) DWs, and the arrows represent the trajectory of their motion.

control the effective signs of the DMI and SHE in the structures[36]. Our experiments show that for any values of SHE and DMI,  $\otimes|\odot$  ( $\otimes|\odot$ ) DWs go faster (slower) for positive curvature. Conversely,  $\otimes|\odot$  ( $\odot|\otimes$ ) DWs go slower (faster) for negative curvature. Thus, although the motion of DWs in such structures arises from two chiral phenomena, namely, DMI and SHE, the chirality of these phenomena plays no role in determining whether the DWs go faster or slower for a given curvature. This is summarized in Fig. 4.7.

The dependence of the DW velocity on the radius of curvature and width of the nanowire is shown in Fig. 4.8. We find that whether the DW velocity is increased or decreased for a given curvature is independent of  $R$  and  $w$ . We note that there is a threshold current density  $J_c$  needed to cause DW motion, as seen earlier in



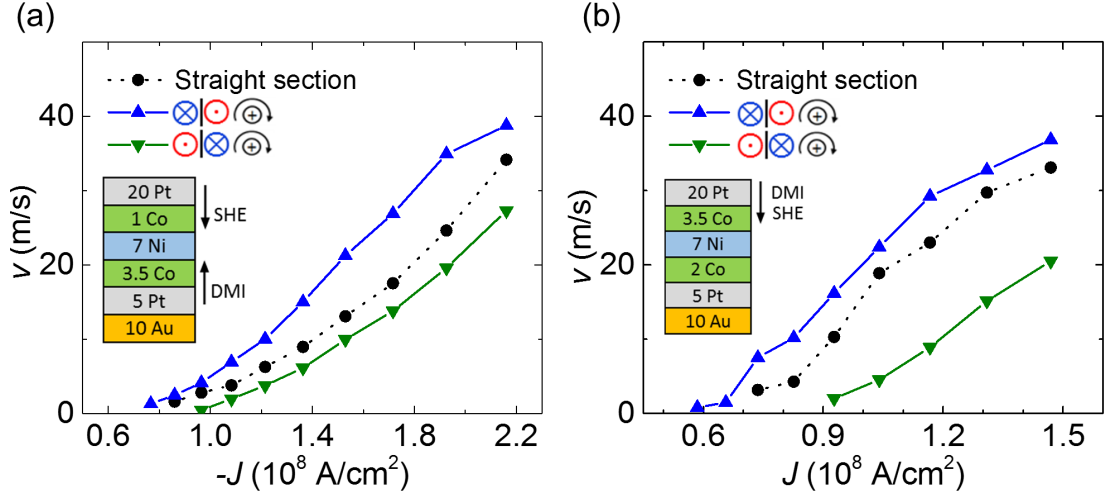


FIGURE 4.6:  $v$  versus  $J$  showing the same relationship [as Fig 4.4] between the sign of the curvature on the increase or decrease in the DW velocity irrespective of the signs of DMI and SHE.

Configuration	Motion	Velocity
$\odot   \otimes$	$\odot \rightarrow$	slow
$\otimes   \odot$	$\otimes \rightarrow$	fast
$\odot   \otimes$	$\odot \leftarrow$	fast
$\otimes   \odot$	$\otimes \leftarrow$	slow

FIGURE 4.7: Truth table derived on the basis of Fig. 4.4 and Fig. 4.6.

Figs. 4.4 and 4.6. When  $J$  slightly exceeds the threshold current for DW motion, the ratio of the velocities for  $\odot | \otimes$  and  $\otimes | \odot$  DWs for the same curvature takes the largest value, reaching almost 10 for the smallest  $R$  used in our experiments, as shown in Fig. 4.8. However, when  $J$  is increased significantly above  $J_c$ ,  $v_{DU}/v_{UD}$  becomes smaller but remains larger than 1 and becomes insensitive to  $R$  and  $w$ . We suppose that the motion of the DWs at low current densities will be “creep-like,” that is, dominated by thermal activation, and at higher current densities will

be “flow-like.” Then, the current density at which the DW motion passes from one regime to the other can be influenced because of the enhanced or reduced torques resulting from the curvature of the wire. In their respective regimes, the ratio of the curvature-dependent torques is similar. Thus, the peak in the velocity ratio will appear when the faster DW moves from the creep-like to the flow-like regime.

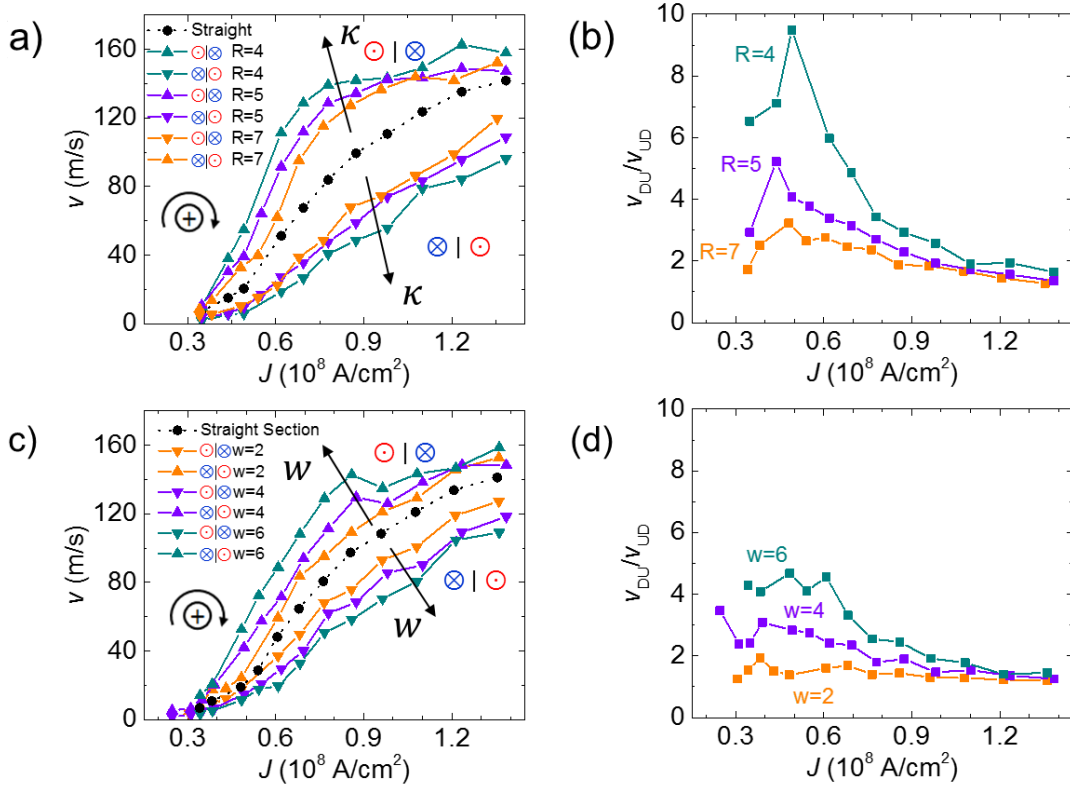


FIGURE 4.8: DW motion as a function of  $\kappa$  (a-b) and  $w$  (c-d) for the film structure used in Fig. 4.4. Nanowires in (a-b) have a constant  $w = 2 \mu\text{m}$  while nanowires in (c-d) have a constant  $\kappa = 16 \mu\text{m}$ . (a,c) show  $v$  versus  $J$  behavior. (b,d) show the calculated ratio,  $v_{DU}/v_{UD}$  for positive  $\kappa$ .

## Chapter 5

# Mechanism underlying the role of curvature

*In the previous chapter, we have conclusively shown that the curvature of a nanowire plays an important role in influencing the speeds of the domain walls (DWs) travelling through them. The speeding up or slowing up of DWs depends on the curvature as well as the configuration of the DW. In this chapter, we unravel the inner workings of the physical mechanism responsible for the curvature effect and develop an analytical model to explain the experimental results we have obtained so far. We also show that the effect of curvature on the motion of DWs can be eliminated by the use of synthetic antiferromagnetic structures.*<sup>1</sup>

---

<sup>1</sup>The contents of this chapter have been either adapted or directly taken from my publication: Garg, C., Yang, S.H., Phung, T., Pushp, A. and Parkin, S.S., 2017. Dramatic influence of curvature of nanowire on chiral domain wall velocity. *Science advances*, 3(5), p.e1602804. Reprinted with permission from AAAS.

## 5.1 Effect of DW tilting on the motion of DWs

As discussed earlier in the Sec 2.2, chiral DWs of Néel-type configuration are formed in films structures with a heavy metal/magnetic layer interface which can then be driven to high speeds due to the spin orbit torques acting on the magnetization of the DW. The injection of current in a nanowire leads to spin accumulation derived from the spin Hall effect (SHE), which cants the DW magnetization,  $\vec{m}_{DW}$ , by an angle  $\phi$ . Subsequently, there is an out-of-plane restoring torque from the DMI field whose orientation is normal to the DW surface in the plane of the nanowire. The speed of the DW is proportional to  $\vec{H}_{DM} \sin(\phi)$ , and thus depends on the torque generated by the DMI exchange field,  $\vec{H}_{DM}$  on the  $\vec{m}_{DW}$ . In straight wires, another important factor that influences DW speed is the current induced tilting of the DW from its initial radial direction that it takes up in the absence of current. Current induced tilting of DWs has previously been observed[78, 79] and is due to an increase in the DMI exchange energy as the spin Hall torque rotates  $\vec{m}$  away from  $\vec{H}_{DM}$  which can be minimized by DW tilting. However, this lengthens the DW, thereby increasing the magnetostatic energy, and limiting the DW tilt angle. The DMI driving torque acting on the DW is thus modified to be  $\vec{H}_{DM} \sin(\phi - \chi)$  where  $\chi$  is the angle the DW normal makes with the nanowire (Fig. 5.1). In straight wires, the tilting of the DW is only determined by the competing interactions between the DMI energy and magnetostatic energy.

In curved wires, an additional cause of tilting arises from the geometrical shape of the curved wire in the following ways: (1) A DW travelling along a curved wire has to travel unequal distances along the inner rim and the outer rim of the wire, and (2) An unequal distribution in the current densities along the cross-section of the wire resulting from geometry will lead to unequal torques along different sections of the DW. Thus, an additional tilt will result that may either add to, or

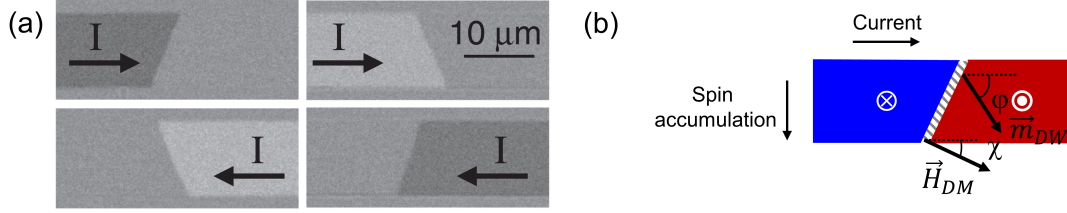


FIGURE 5.1: (a) Tilting of a chiral DW under current-induced torques in a Pt/Co/Ni/Co heterostructure (Adapted from [78]. Copyright 2012 The Japan Society of Applied Physics). (b) Illustration of the  $\vec{H}_{DM}$  tilt,  $\chi$  and DW magnetization angle,  $\phi$  induced under the effect of current-induced motion.

subtract from the tilt that is already induced by the DMI interaction. In order to qualitatively and quantitatively evaluate the additional tilt imposed by the curved wire geometry, we develop an analytical model that has been successfully used to describe the current induced motion[36, 39, 80] and dynamic tilting[79] of DWs in straight racetracks. In this model, the DW's profile is assumed fixed along the cross-section of the wire and its motion can be evaluated for a one-dimensional nanowire. A quasi-2D model for curved wires was developed under the assumption that the DW's profile now remains constant within the DW's moving frame of reference. To do this, we need to make a transformation between the Cartesian coordinate system of the observer and the cylindrical coordinate system of the DW. The critical parameters in the model to describe the DW motion with the moving frame of reference are,  $q$ ,  $\phi$  and  $\zeta$ , (see Fig. 5.2; Fig. A.1a).  $\phi$  is the angle that  $\vec{m}$  makes with respect to the tangent direction to the nanowire, and  $\zeta$  is the tilting angle of the DW with respect to the radial direction. Apart from  $\vec{H}_{DM}$  whose direction is always perpendicular to the DW,  $\vec{H}_k$  is the DW shape anisotropy field, which is also always perpendicular to the DW, but whose direction favors  $\vec{m}$  being parallel to the DW. There are two important torques that drive the DW that are shown in Fig. 5.2A. These torques derived from  $\vec{H}_{DM}$  and  $\vec{H}_k$  are  $\vec{\tau}_{DM} = -\gamma \vec{m} \times \vec{H}_{DM}$  and  $\vec{\tau}_k = -\gamma \vec{m} \times \vec{H}_k$ , respectively, where  $\gamma$  is the

gyromagnetic ratio. Based on our model, we find that the tilt of the DW during motion can be either in the same or the opposite direction to the physical rotation of the wire itself (i.e. curvature) leading to distinctive behaviors for opposite curvatures as illustrated in Fig. 5.2. When the DW tilts away from the direction of the curvature then the chiral spin torque is decreased (Fig. 5.2a). For opposite curvature then the chiral spin torque is increased (Fig. 5.2b). In both cases this is due to the increase or decrease of the angle between the  $\vec{H}_{DM}$  and  $\vec{m}$ , which determines the driving torque on the DW. In addition  $\vec{\tau}_k$  either adds or subtracts from  $\vec{\tau}_{DM}$  depending on the curvature, which is different from straight wires when  $\vec{\tau}_k$  is always opposite to  $\vec{\tau}_{DM}$ . Refer to the Appendix A in order to go through the complete details of the analytical model and its derivation.

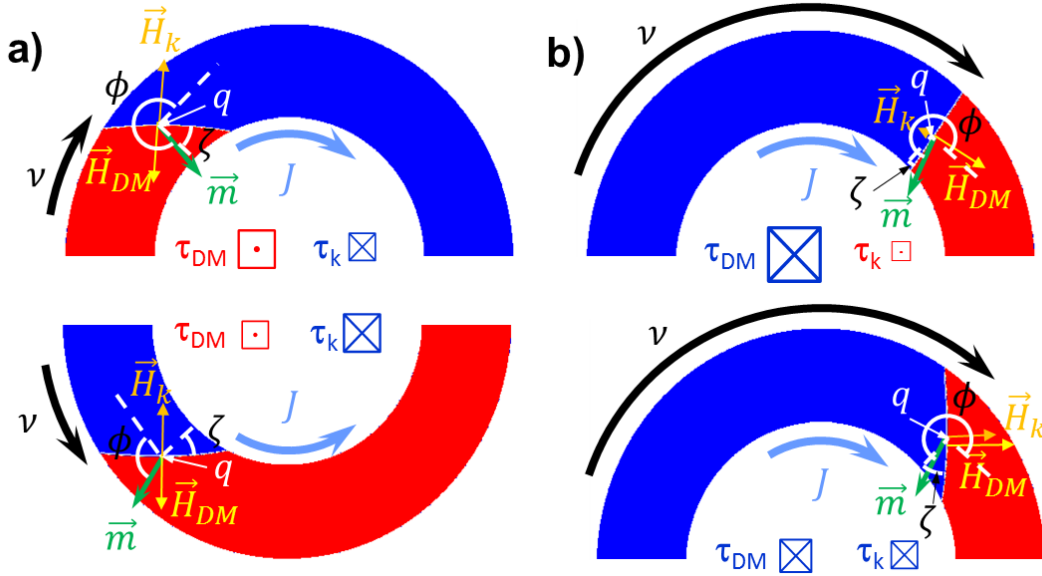


FIGURE 5.2: Schematic illustration of the critical parameters, fields, and torques that describe the current-induced DW motion. (a)  $\odot|\otimes$  positive curvature (top) and  $\otimes|\odot$  with negative curvature (bottom). (b)  $\otimes|\odot$  with positive curvature at low  $J$  (top) and  $\otimes|\odot$  with positive curvature at high  $J$  (bottom). Size of symbols  $\square$  and  $\boxtimes$  represent the magnitudes of their respective torques.

## 5.2 Comparison with experimental results

Detailed results from the quasi 2D model that include the effect of non-uniform current density, DW pinning, and thermal fluctuations in the DW are shown in Fig. 5.3. Simulations were performed for devices with dimensions identical to ones used to obtain experimental results in Fig. 4.8. The model has features similar to our experimental results concerning the dependence of  $\nu$  on  $J$ , namely a threshold  $J$  above which  $\nu$  gradually increases until  $\nu$  plateaus at different values for different curvatures and widths. Both  $\phi$  and  $\zeta$  reach plateaus at the same  $J$  as  $\nu$  but whereas  $\zeta$  takes very different values for different curvatures,  $\phi$  is insensitive to the curvature. Thus, it is  $\zeta$  that controls the dramatic dependence of the dynamical motion of the DW on curvature, as illustrated schematically in Fig. 5.2.  $\zeta$  takes a smaller value for a  $\otimes|\odot$  going through a positive curvature due to the competition between the DW tilting due to the DMI and the geometry of the wire. As a result, this DW travels at a higher speed. For a  $\odot|\otimes$  travelling along a positive curvature, the tilt adds up, and hence the DW travels with a larger  $\zeta$  and a smaller speed. Interestingly,  $\zeta$  has a non-monotonic dependence on  $\nu$  that results from the DW pinning. Whilst it is clear that our model does not exactly match our experiments it does account for the major features that we find, and gives useful insight into their origin. Most importantly, the universal relationship between the DW speed and curvature that we find experimentally is reproduced by the model. The model also shows how increasing either the curvature or width of wire increases the disparity in the motion of DW when travelling through opposite curvatures.

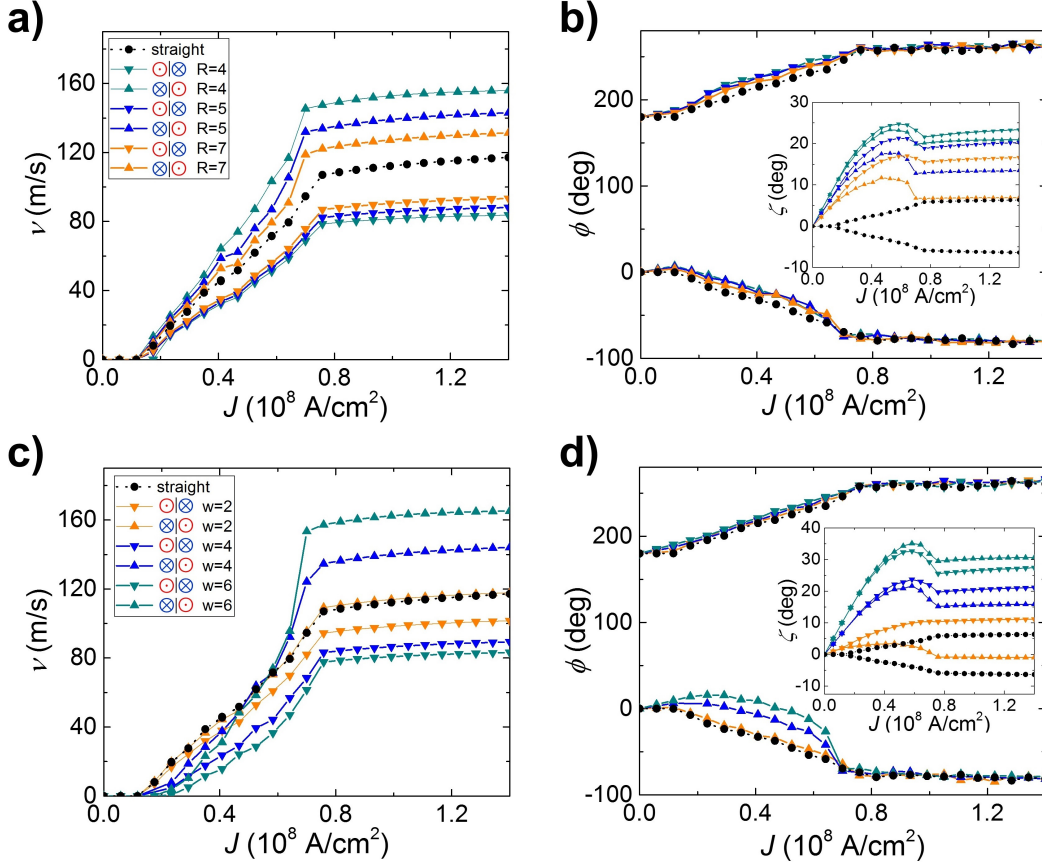


FIGURE 5.3: Calculated  $\nu$  vs  $J$  for  $\odot|\otimes$  and  $\otimes|\odot$  configurations for the case  $\kappa > 0$ : (a) straight wire, and curved wires with  $R = 4, 5$  and  $7 \mu\text{m}$  for fixed  $w = 2 \mu\text{m}$ , (b) straight wire, and curved wires with  $w=2, 4$  and  $6 \mu\text{m}$  for fixed  $R=16 \mu\text{m}$ . (b,d) Calculated  $\phi$  (main panels) and  $\zeta$  (insets) vs  $J$  that correspond to (a) and (c) respectively, with the same corresponding colors and symbols. Note that  $R$  and  $w$  in (a-d) are in  $\mu\text{m}$ . All simulations were done for  $\kappa > 0$ . Parameters used for simulation are discussed in the Appendix A.

### 5.3 Effect of curvature in narrow nanowires

The large disparity in motion of alternating DWs in a curved wire was obtained for micron-wide wires. One may question if the curvature still makes a difference in DW motion of narrow nanowires since the widths of nanowires should be small ( $\sim$  a few tens of nanometers) in practical devices with high density. Hence to



answer this question we calculate the DW velocity for various radii of curvature  $R = 100, 125$  and  $175$  nm at fixed width  $w=50$  nm, which correspond to the same ratio of  $\frac{R}{w}$  for  $R = 4, 5$  and  $7 \mu\text{m}$  at fixed  $w = 2 \mu\text{m}$  that are shown in Fig. 4.8a-b and Fig. 5.3a-b. It is clearly observed that the DW velocity is different depending on the curvature although the difference is smaller than the wider wires (see Fig. 5.4). However, this difference in narrow wires is critical thus preventing the proper operation of racetrack device since the lockstep motion independent of DW configuration is essential.

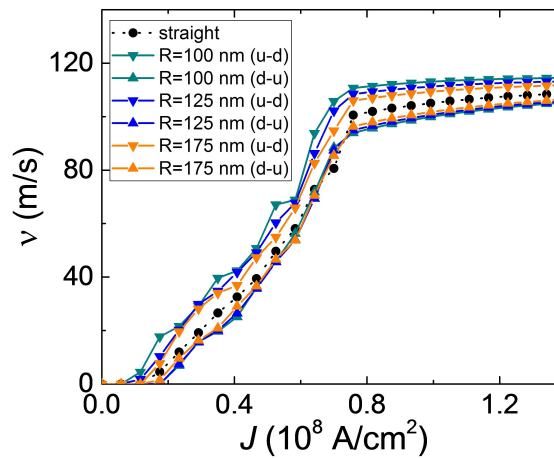


FIGURE 5.4:  $\nu$  against  $J$  of Q2D model calculation results that take non-uniform current distribution, pinning and thermal fluctuation into account for  $R=100, 150, 175$  nm while  $w$  is fixed at  $50$  nm. All simulations were done for  $\kappa > 0$ .

## 5.4 Comparison with micromagnetic simulations

Micromagnetic simulations of current driven DW motion in curved nanowires have been carried out using LLG micromagnetics simulator[81]. Due to the memory intensiveness of simulating a wire of the same size as our experiment, we simulated a wire which was smaller in dimension ( $w=0.4 \mu\text{m}$ ,  $R=1 \mu\text{m}$ ). We have then initialized two magnetic configurations for running our simulation with the domain wall

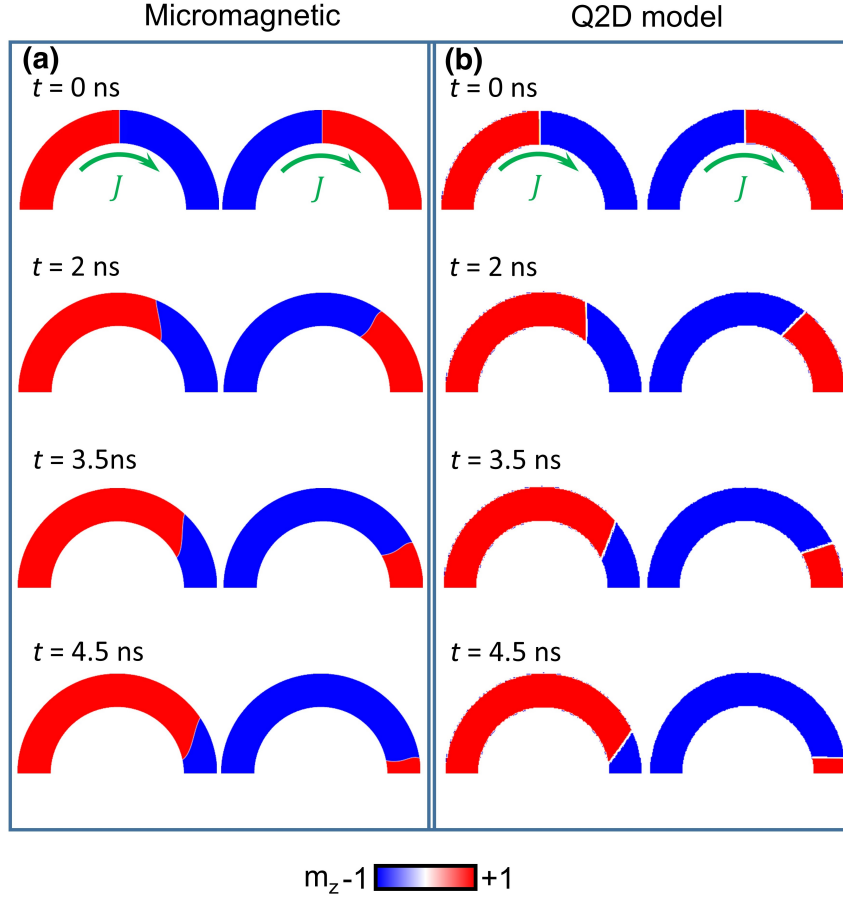


FIGURE 5.5: Snapshots of (a) micromagnetic simulations and (b) Q2D model calculations at time  $t=0, 2, 3.5$  and  $4.5$  ns since the onset of current pulse application. For both simulations, the following parameters are employed: ferromagnetic layer thickness  $t_f$  is  $1.5$  nm, the DMI parameter  $D = -1$  erg/cm<sup>2</sup>,  $M_s = 580$  emu/cm<sup>3</sup>,  $K_{eff} = 5.11 \times 10^6$  erg/cm<sup>3</sup>,  $A = 0.75$   $\mu$ erg/cm,  $\alpha = 0.1$ ,  $w = 0.4$   $\mu$ m,  $R = 1$   $\mu$ m, the current density,  $J = 1.0 \times 10^8$  A/cm<sup>2</sup>, and spin Hall angle  $\theta_{SH} = 0.1$ . As for the micromagnetic simulations the used cell size is  $2.5$  nm  $\times$   $2.5$  nm  $\times$   $1.5$  nm, and the spin Hall layer that is placed under the ferromagnetic layer is chosen to be  $1.5$  nm thick.

in the middle of the wire. After sending an electrical pulse with the current density  $1.0 \times 10^8$  A/cm<sup>2</sup>, we see that that a  $\otimes|\odot$  DW responds differently than a  $\odot|\otimes$  consistent with our understanding and experimental observations. The micromagnetic simulation results are in excellent agreement with Q2D model calculations that use the same parameters (see. Fig. 5.5).

## 5.5 Elimination of the effect of curvature in synthetic antiferromagnetic structures

One very important consequence of the curvature dependent DW velocity is that, in the presence of curvature,  $\odot|\otimes$  and  $\otimes|\odot$  DWs move at different speeds: these speeds, as we have shown, can vary by an order of magnitude. This is a serious problem that has not previously been appreciated for DW devices such as race-track memory that rely on the lock-step motion of a series of DWs along a nanowire. However, we have discovered that the influence of the curvature is eliminated in synthetic antiferromagnetic (SAF) nanowires. Such SAF nanowires are comprised of lower and upper magnetic layers that are coupled strongly antiferromagnetically via an ultra-thin ruthenium layer[82, 83, 84] (see the schematic structure in Fig. 5.6a). Typical results for the DW velocity versus current density for a SAF U-shaped device are shown in Fig. 5.6b. We note that, in agreement with our previous results for the current induced DW motion in SAF nanowires[80], the DW velocity is significantly higher in the SAF structure compared to single magnetic layer devices, both in the straight and the curved sections. The DWs move at speeds of up to 450 m/s compared to only 150 m/s for the same current densities in single magnetic layer nanowires. The data in Fig. 5.6b clearly show that the DWs move at the same velocity independent of the curvature of the wire and thus, the lock-step motion of a series of DWs is possible, as shown in Fig. 5.6c.

The insensitivity of the DW velocity on the curvature of SAF nanowires can be explained as follows. Firstly, the DW tilting is largely suppressed in the SAF because the tilting of the  $\odot|\otimes$  DW in one layer is opposite to the  $\otimes|\odot$  DW in the other layer and the strong antiferromagnetic coupling therefore mitigates tilting. Secondly, the CIDWM in the SAF nanowire is dominantly driven by an exchange-coupling torque[80] that is derived from the antiferromagnetic exchange coupling

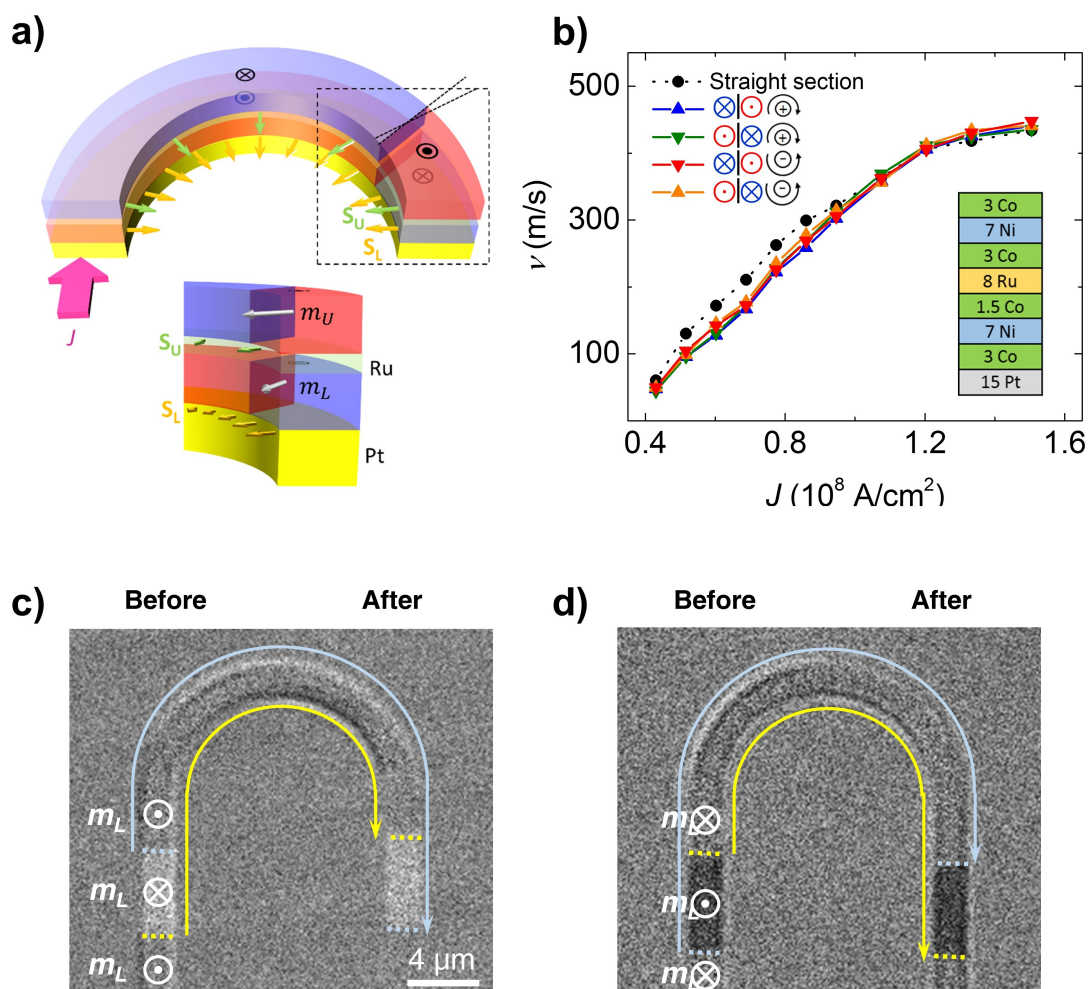


FIGURE 5.6: (a) Schematic illustration of the DW motion in a curved SAF nanowire showing the current induced rotation of the Néel moments in the top ( $m_U$ ) and bottom ( $m_L$ ) layers by SHE from spin accumulation from the underlying Pt layer. (b)  $v$  vs  $J$  for  $\odot|\otimes$  and  $\otimes|\odot$  for positive and negative curvature for a device with  $R = 7 \mu\text{m}$  and  $w = 2 \mu\text{m}$ . The film stack is shown in the inset with thicknesses of layers in  $\text{\AA}$ . (c,d) Representative Kerr images showing the motion of a  $(\odot|\otimes|\odot)$  and  $(\otimes|\odot|\otimes)$  DWs through a curved SAF nanowire.

field that is much larger than both  $\vec{H}_{DM}$  and  $\vec{H}_k$ . This torque depends only on the relative angle between the DW magnetizations in the lower and upper layers  $\vec{m}_L$  and  $\vec{m}_U$  which is independent of the DW configuration.

In summary, we have found that the velocity of DWs is significantly affected by the curvature of racetracks in which they are driven by current. Moreover, we find that there is a universal relationship between the increase or decrease of the DW's velocity to the direction in which the DWs move around the racetrack, independent of the sign of the SHE and DMI that provide the driving torques. In racetracks formed from synthetic antiferromagnets the effect of the curvature is significantly diminished or eliminated, reinforcing the attractiveness of synthetic antiferromagnetic racetracks for DW based memory, logic and sensor devices.



## Chapter 6

# Highly Asymmetric Chiral Domain-Wall Velocities in Y-Shaped Junctions

*In the previous chapters, it was shown that a DW travelling through a curvature can speed up or slow down depending on the sign of curvature and this effect arises from the influence of the curvature on the tilt of the DW surface as it travels through it. In a curved nanowire, the DW travels along a wire of constant curvature, thus reaching steady-state dynamics. Here, by designing a nanowire in the shape of a Y-shaped junction, we observed the dynamics of a DW which upon travelling from an input branch into the two symmetric output branches is subjected to a momentary change in the curvature at the junction connecting them. This allowed us to capture the motion of a DW as it enters a metastable state upon experiencing an abrupt turn in the nanowire and its eventual relaxation back to steady-state*

*dynamics. We devise a way to use this device for performing sorting of domains into one branch or another.*<sup>1</sup>

## 6.1 Experimental Details

Fig. 6.1b shows an optical image of a representative Y-shaped device used to perform Kerr microscopy measurements of the DW motion. The device is patterned (see Sec. 3.1) using standard lithography techniques from the magnetic stack: 100 AlO<sub>x</sub> / 20 TaN / 15 Pt / 3 Co / 7 Ni / 1.5 Co / 50 TaN (the numbers indicate the respective film thicknesses in Å) grown by magnetron sputtering on Si substrates with a 250 SiO<sub>2</sub> layer for electrical isolation. Care is taken so that there is minimal roughness along the edges of the structure so that both output branches B and C, with an angle  $\theta$  between them, are nominally identical for DW motion[85]. The input A is designed to be twice in width as compared to the widths of the two output branches B and C to keep the current density across the entire Y-shaped structure constant. The current crowding near the bifurcation region is highly localized as obtained from finite element modeling as seen in Fig. 6.2. A nanosecond voltage pulser is connected to the input branch whereas the two output branches are electrically grounded. Fig. 6.1c illustrates schematically the SHE-derived spin accumulation profile at the Pt-Co interface due to the current flowing in the Pt underlayer along the different branches of the structure.

The Y-shape junction can be used as a tool to explore the current-driven dynamics of a chiral DW which would ordinarily not be possible in a straight wire geometry. By causing the DW to travel through an abrupt turn in the Y-shape, we obtain

---

<sup>1</sup>The contents of this chapter have been either adapted or directly taken from my publication: Garg, C., Pushp, A., Yang, S.H., Phung, T., Hughes, B.P., Rettner, C. and Parkin, S.S., 2018. Highly Asymmetric Chiral Domain-Wall Velocities in Y-Shaped Junctions. *Nano letters*, 18(3), pp.1826-1830.



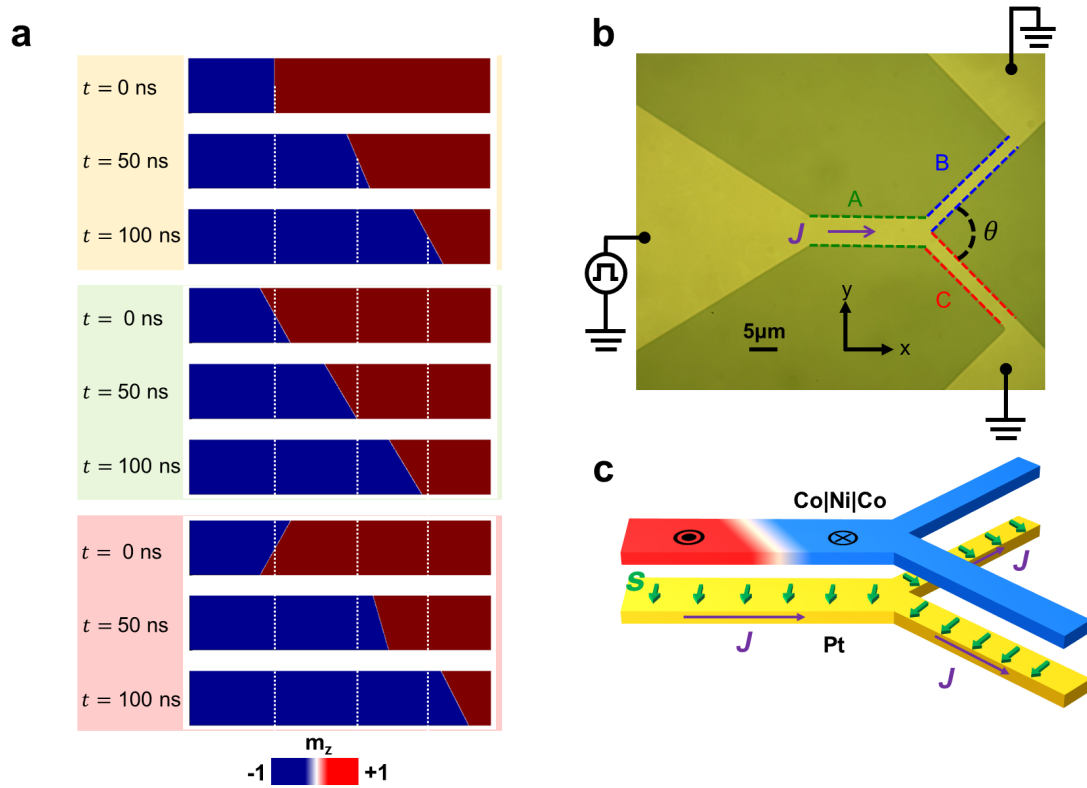


FIGURE 6.1: Out-of-equilibrium motion of DWs and device structure. (a) Time-resolved 1D model snapshots of the current-induced motion of a chiral DW in wires with different initial DW states at  $t = 0$  ns, each having a different tilt angle. Reference lines (white) are drawn to compare the displacements of DWs  $t = 50$  and  $100$  ns. Depending on the initial tilt, a DW travels either faster or slower compared to a DW which starts from a rest state. Modelling parameters are described in the later sections. (b) Micrograph and electrical circuit of the Y-shape structure with its three branches labelled as A, B and C. The width of input branch A ( $5 \mu\text{m}$ ) is twice that of output branches B and C ( $2.5 \mu\text{m}$ ) that subtend an angle  $\theta$  between them. All the branches are  $20 \mu\text{m}$  long. Branch A is electrically connected to a nanosecond pulser while branches B and C are electrically grounded. (c) Schematic showing a typical Y-shape structure and the spin Hall derived spin accumulation (green) which changes direction at the Y-junction. The current density  $J$  is uniform across all branches except for narrow regions near the bifurcation region.

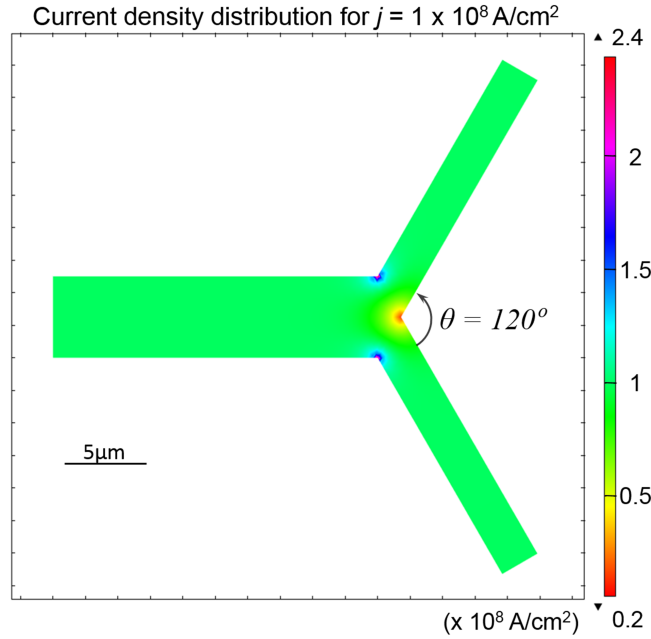


FIGURE 6.2: Current density distribution from finite element model shows increase in the current density around the outside edges and a corresponding decrease in current density along the inside edges. The regions with smaller or larger current densities are quite small and scale with the width of the magnetic structure and  $\theta$ .

an out-of-equilibrium tilt of the DW with respect to the new spin accumulation direction (that is defined by the current direction in the nanowire). Depending on this tilt, a DW travels either faster or slower than it would do when starting from a rest state. This is succinctly captured in the snapshots of our modelling results as shown in Fig. 6.1a. We see that DWs with different tilt angle in three wires travel with different speeds. Eventually, the DW accelerates or decelerates to reach steady-state motion and the associated timescales can vary distinctly depending on the initial out-of-equilibrium tilt and width of the wire. Thus in order to understand this, we design various Y-shape junctions and observe dramatic differences in the DW dynamics that we explain using an extended form of the 1D model.

A DW is first created in the input branch A (Fig. 6.3) and is then moved towards

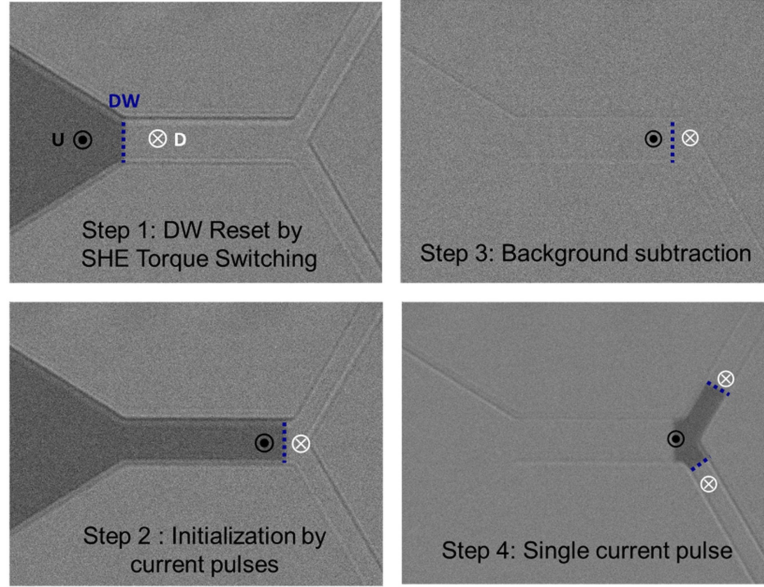


FIGURE 6.3: The wider input branch is connected to a voltage pulser, whereas both the narrower output branches are electrically grounded.

the bifurcation region of the Y-junction by a predetermined distance without any external magnetic field. Once the DW is at the desired location, the background Kerr contrast is reset. Afterwards, a single pulse of voltage  $V_p$  with a typical rise time of 300ps and a fall time of 700ps and pulse length  $t$  is applied across the device, which makes the DW (i) move distance  $d_A$  from its initial position in branch A, (ii) split into two DWs that then (iii) travel into the two output branches, represented by the Kerr contrast images. The distances traversed  $d_B$  and  $d_C$  by the two DWs in their respective output branches B and C are then measured. This single-shot experiment for a given  $V_p$  and  $t$  is repeated 50 times to build statistics. The experiment is repeated for  $10 \text{ V} \leq V_p \leq 28 \text{ V}$  and  $20 \text{ ns} \leq t \leq 100 \text{ ns}$  for devices with  $\theta = 30^\circ, 60^\circ, 90^\circ$  and  $120^\circ$  as summarized in Fig. 6.4. The two distances  $d_B$  and  $d_C$  differ from each other in a systematic way as a function of  $V_p$ ,  $t$  and  $\theta$ . Note that the domains wall in Fig. 6.4a are oriented nearly perpendicular to the wire edges whereas in earlier experiments on similar wires the domain walls were found to have a significant tilt after current driven

motion[78]. However, in these previous studies the magnetic layers were deposited on a TaN seed layer as compared to the  $\text{Al}_2\text{O}_3/\text{TaN}$  seed layers used in the current experiments. The latter seed layer has the effect of reducing the pinning of the domain walls so that after the current pulse is removed the tilt of the domain wall introduced by the spin-orbit torque relaxes back to its equilibrium state without any tilt.

Fig. 6.4a (left column) shows representative Kerr images of an up-down (UD) DW that travels much further in branch B than in branch C as  $\theta$  is increased after a  $V_p = 16$  V and  $t = 100$  ns pulse is applied. Remarkably, in some devices, a down-up (DU) DW (Fig. 6.4a; right column) travels further in branch C than in branch B. Fig. 6.4b represents the asymmetric behavior of an UD DW in a device with  $\theta = 90^\circ$  (see [85] for detailed data for all  $\theta$ ). Experimental data indicating the distance travelled by a DW into the branches A, B and C upon application of a single pulse is indicated by solid lines. Dashed lines of corresponding color indicate the displacement of a DW, had it travelled in a straight wire, with a constant steady-state velocity  $u_V$  in the respective branches. Values of  $u_V$  are obtained experimentally from current-induced DW motion experiments in the device. Clearly, in the branch B, the DW has travelled further and in the branch C, it has fallen behind compared to a DW traveling in a straight wire with the velocity,  $u_V$ . Alternatively, we can plot  $d_B - d_C$ , which is the asymmetry in the distance traversed by the DWs in branches B and C as shown in Fig. 6.4c. We find that for  $V_p = 15.8$  V,  $d_B - d_C$  keeps increasing up to  $t = 100$  ns which is the range of our instrument. This indicates that the out-of-equilibrium DW dynamics which are responsible for this asymmetry are sustained for significant timescales and distances beyond the initial bifurcation region where the DW splits. The DWs reach an equilibrium state when they start moving at  $u_V$  in both the branches and hence  $d_B - d_C$  saturates. This is seen more clearly for  $V_p = 19.9$  V and 25 V. For

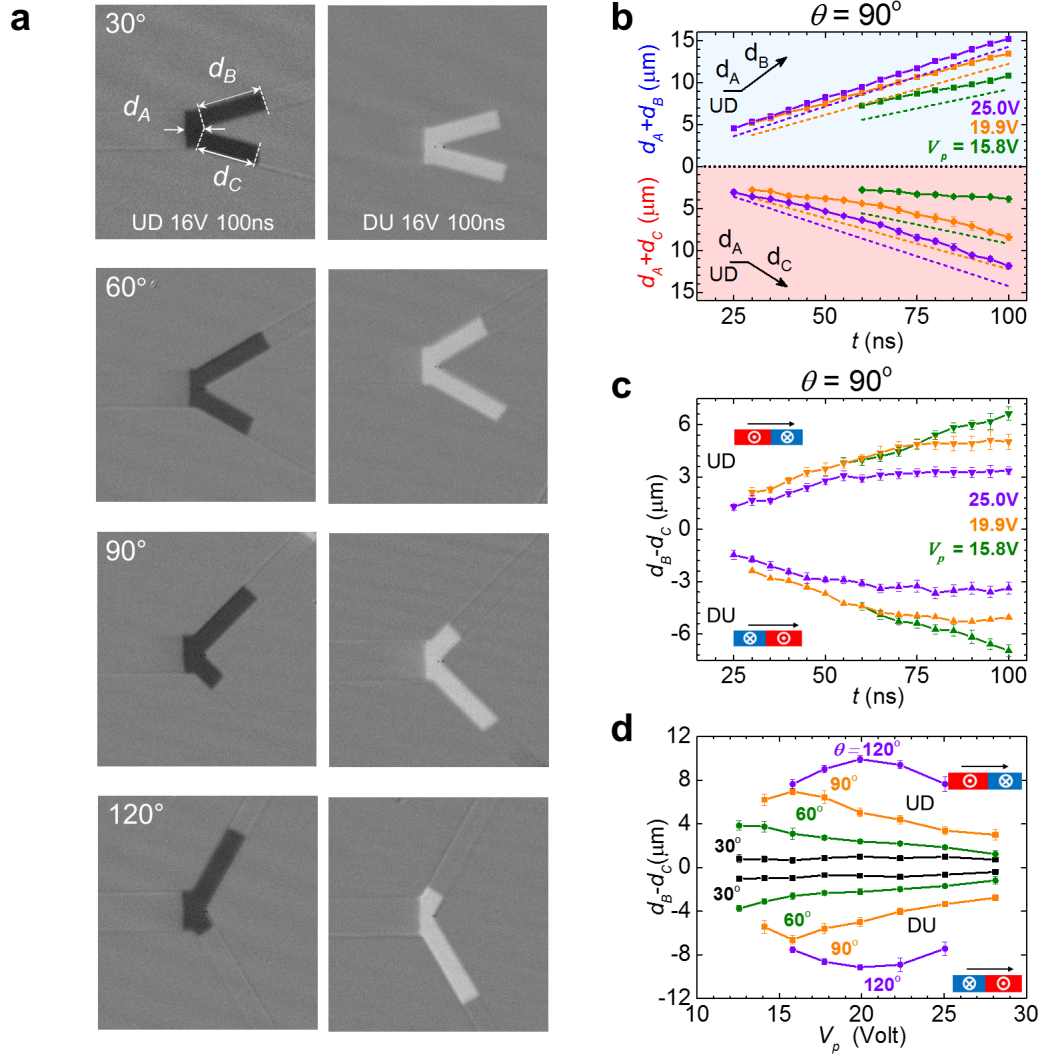


FIGURE 6.4: Asymmetric DW propagation. (a) (left column) The dark region shows the wake of an up-down (UD) DW that moves from branch A into branches B and C upon splitting into two DWs when a single pulse of  $V_p = 16$  V and  $t = 100$  ns is applied across the devices with  $\theta = 30^\circ$ ,  $60^\circ$ ,  $90^\circ$ ,  $120^\circ$ . (right column) The bright region indicates the same but for a down-up (DU) DW. (b)  $d_A + d_B$  and  $d_A + d_C$  measured as a function of  $V_p$  and  $t$  for  $\theta = 90^\circ$ . Each data point is obtained after performing 50 repetitions to build statistics. The dashed lines indicate the distance that the DW should have moved at its steady-state velocity in the respective branches. Only those combinations of  $V_p$  and  $t$  have been considered where the DW in branch A splits into two and travels into the two output branches B and C. (c) Asymmetry defined as  $d_B - d_C$  for  $\theta = 90^\circ$  for UD (top-half panel) and DU (bottom-half panel) DWs. (d) Asymmetry as a function of  $V_p$  for  $t = 100$  ns for devices with  $\theta = 30^\circ$ ,  $60^\circ$ ,  $90^\circ$  and  $120^\circ$ . Measurements for UD are in the top-half panel and DU are in the bottom-half panel.

$\theta = 120^\circ$ ,  $d_B - d_C$  does not saturate at any  $V_p$  (refer to [85]).  $d_B - d_C$  for an UD and DU DW also look remarkably like a mirror image of each other, i.e., the asymmetry in the branches is reversed (Fig. 6.4). Although electrical measurements confirm that the branches B and C are symmetrical, this further suggests that this asymmetry is not due to spurious effects such as lithographic patterning, edge pinning, current crowding near the bifurcation region, or any other inhomogeneity in the magnetic structure that would make one branch more favorable over the other for DW motion. Fig. 6.4d shows a systematic increase in the asymmetry  $d_B - d_C$  with increasing  $\theta$  for different voltages, which we will discuss later.

## 6.2 Analytical model for interpretation of results

In the previous chapter, we described the use of an analytical model to account for the effect of curvature on the velocity of curved wires. The differences in the DW tilting behaviour along different curvatures resulted in the speeding up/slowing down of DWs along a curved wire. In a similar vein, we have developed a detailed 1D model [36, 79] extended in 2D to account for the observed experimental results for the Y-shape device. The difference here being that instead of a DW travelling along a wire with constant curvature, it is subjected to a single abrupt turn in its trajectory. It is assumed that when a single DW from the input branch splits into two DWs, which then enter the upper (lower) branch of the Y-junction, the DW tilting angle and magnetization angle change immediately and instantaneously by  $+\frac{\theta}{2}$  ( $-\frac{\theta}{2}$ ) with respect to the wire edge direction (Fig. 6.5).

For the case of perpendicularly magnetized nanowires the DW dynamics can be described within the 1D model by just two parameters, namely the position  $q$  of the DW along the nanowire and its conjugate momentum  $2M_s\phi/\gamma$  where  $\phi$  is the angle

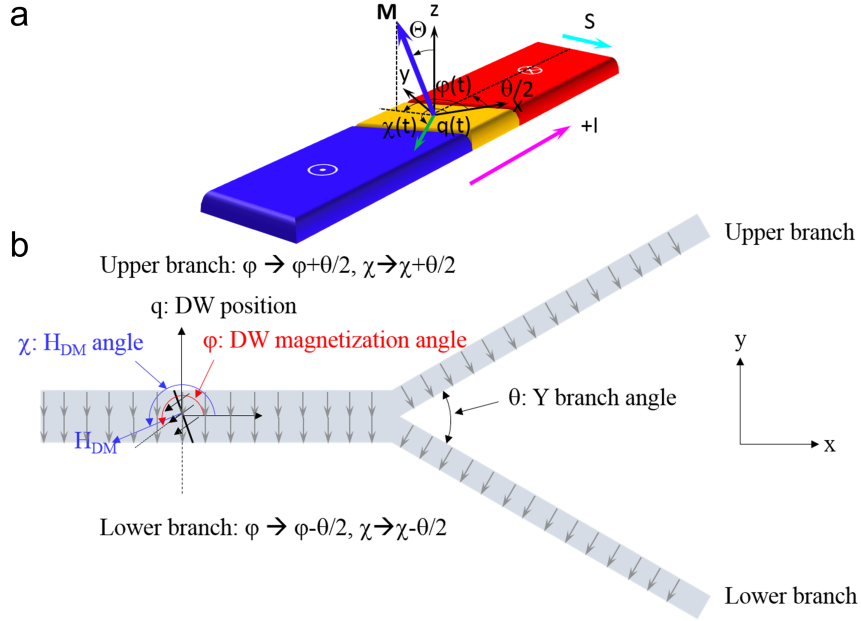


FIGURE 6.5: (a) Notation for the coordinate axes along with the UD DW and its magnetization angle. (b) Upon entry into the output branches of the Y-shaped structure, the DW magnetization angle and the normal to the DW front both get subjected to an abrupt change in their value by  $+\frac{\theta}{2}$  ( $-\frac{\theta}{2}$ ), depending on upper (lower) branch. In the wider input branch,  $\theta = 0$ .

of the DW's magnetization in the plane of the wire with respect to the direction  $x$  along the wire's length (see Fig. 6.5a),  $M_s$  is the saturation magnetization, and  $\gamma$  is the gyromagnetic ratio. We use the corresponding symbols,  $q$  (the position of DW center),  $\phi$  (DW magnetization angle), and  $\chi$  (Dzyaloshinskii-Moriya (DM) field angle or DW tilting angle) as defined in Fig. 6.5a. In the Y-shaped nanowire, the DW profiles of the DWs are given by

$$\Theta = 2 \tan^{-1} \left\{ \exp \left[ \pm \frac{x \cos \left( \chi \mp \frac{\theta}{2} \right) + y \sin \left( \chi \mp \frac{\theta}{2} \right) - q \sin \left( \chi \mp \frac{\theta}{2} \right)}{\Delta} \right] \right\}$$

, where  $+$  and  $-$  in blue correspond to the UD and DU DW configurations, respectively whilst  $-$  and  $+$  in red correspond to upper and lower branches, respectively.

$\Theta$  is the angle that the magnetization is rotated from the direction perpendicular to the layer, i.e. the  $z$  axis, as shown in Fig. 6.5a.  $\Delta$  is the domain wall width parameter. Note that the  $y$  axis is set along the direction in the plane of the wire transverse to the wire. Note that  $\phi$  and  $\chi$  are all defined from the  $+x$  axis. We describe the dynamics of DW motion in the Y-shape nanowire by extending the Landau-Lifshitz-Gilbert (LLG) equation to include the adiabatic and non-adiabatic spin transfer torques, the spin Hall current torque, the Dzyaloshinskii-Moriya exchange field, and an applied longitudinal field. The magnetization dynamics is then given by the following equation:

$$\frac{\partial \mathbf{M}}{\partial t} = -\gamma \mathbf{M} \times \mathbf{H} + \frac{\alpha}{M} \mathbf{M} \times \frac{\partial \mathbf{M}}{\partial t} - b_J \mathbf{M} \times \mathbf{M} \times \frac{\partial \mathbf{M}}{\partial x} - \beta c_J \mathbf{M} \times \frac{\partial \mathbf{M}}{\partial x} + \xi_{SH} b_J \mathbf{M} \times \mathbf{M} \times \hat{y} \quad (6.1)$$

where  $M(r, t)$  is the magnetization vector,  $\alpha$  is the Gilbert damping constant,  $H$  is the effective magnetic field,  $b_J$  is the adiabatic spin transfer torque (STT) coefficient,  $\beta$  is the non-adiabatic STT coefficient,  $\xi_{SH}$  is the spin Hall angle (or the effective spin Hall angle that describes the magnitude of the spin accumulation that the magnetic layer is subjected to), and  $\xi_{SH} b_J$  is the magnitude of the spin Hall current torque. Note that the accumulated spin from the spin Hall current is oriented along transverse to the wire length direction (Fig. 6.5). The effective magnetic field  $H$  is determined by the magnetostatic and exchange energy density  $w$  per area where

$$\mathbf{H} = -\frac{\partial w}{\partial \mathbf{M}}$$



The equations of motion is derived from eq. (1) as follows;

$$\begin{aligned}
-\frac{\alpha \cos(\chi \mp \frac{\theta}{2})}{\Delta} \dot{q} \pm \dot{\varphi} &= \frac{\beta u}{\Delta} \cos(\chi \mp \frac{\theta}{2}) \pm \gamma H_z - \frac{\pi}{2} \gamma H_{SH} \cos(\varphi \mp \frac{\theta}{2}) \\
-\frac{\cos(\chi \mp \frac{\theta}{2})}{\Delta} \dot{q} \mp \alpha \dot{\varphi} &= \frac{\cos(\chi \mp \frac{\theta}{2})}{\Delta} u \mp \frac{\gamma H_k}{2} \sin 2(\varphi - \chi) \mp \frac{\pi}{2} \gamma H_{DM} \sin(\varphi - \chi) \\
\frac{\pi^2}{6\gamma} \alpha M_s \Delta \left( \left( \frac{w}{\Delta \pi} \right)^2 \sec^2 \chi + \tan^2 \chi \right) \dot{\chi} &= -\sigma \tan(\chi \pm \frac{\theta}{2}) \\
\mp \pi \Delta M_s H_{DM} \sin(\varphi - \chi) - H_k M_s \Delta \sin 2(\varphi - \chi) &
\end{aligned} \tag{6.2}$$

where  $\sigma \equiv 4K\Delta + M_s H_k \Delta \sin^2(\varphi - \chi) + \pi M_s H_{DM} \Delta \cos(\varphi - \chi)$ , i.e., DW magnetostatic energy. Here the upper and lower of the signs within the blue symbols correspond to the UD and DU domain magnetic configurations, respectively while those within the red symbols correspond to the upper and lower branches, respectively.  $H_k$  is the magnitude of the in-plane anisotropy field derived from the shape anisotropy of the DW that favors a Bloch DW configuration over that of a Néel wall.  $H_{DM}$  is the Dzyaloshinskii–Moriya interaction exchange field at the DW whose direction is always perpendicular to DW length direction but which is of opposite sign for the UD and DU configurations (see Fig. 6.6a and Fig. 6.5). Pinning of the DWs due to localized imperfections is not considered here. The volume spin transfer torque from the current within magnetic layer is parameterized by  $u = \frac{\mu_B P J}{e M_s}$ , where  $\mu_B$  is the Bohr magneton,  $e$  is the electron charge,  $P$  is the spin polarization of the current and  $J$  is the current density in the magnetic layer. The spin Hall effect is parameterized by an effective field  $H_{SH}$  that is given by  $H_{SH} = \frac{\hbar \xi_{SH} J_{UL}}{2e M_s}$  where  $J_{UL}$  is the current density in the underlayer. Incorporating these equations, we solve for time evolution of the DW displacement,  $d$ , instantaneous velocity  $v$ , angle of the DMI field,  $\chi$ , and DW magnetization angle,  $\phi$ , as the DW traverses from the wider branch A (green) to the two narrower output branches B (blue) and C (red) for devices with different widths,  $w$  and angle  $\theta$  as indicated in each plot (Fig. 6.6b-e, 6.7c and [85]). The curves have been color coded depending upon which branch the DW is located. The dashed green lines

indicate the DW response for comparison when  $\theta = 0$ , i.e., for the case when the output branch were straight and its width had abruptly decreased to half the width of branch A while maintaining the same current density.

From its inertial frame of reference, when a DW traveling in input branch A enters an output branch (B or C), it experiences an abrupt change in the SHE-SOT as well as the DMI torque. Specifically, upon entry of the DW into an output branch, the DMI effective field,  $\vec{H}_{DM}$  (Fig. 6.6a,d) retains its direction (due to the tilt of the DW evolving slowly in time - being dependent on square of the width of the nanowire[79]), whereas the DW's magnetization,  $\vec{m}_{DW}$ , responds almost instantly ( $< 1\text{ns}$ ) to the abrupt change in SHE-SOT (Fig. 6.6a,e). Consequently, the DMI-derived driving torque ( $\propto \vec{m}_{DW} \times \vec{H}_{DM}$ ) becomes instantaneously higher for the UD (DU) DW in the upper (lower) branch resulting in higher instantaneous velocity, whereas it significantly decreases in the lower (upper) branch resulting in lower instantaneous velocity (Fig. 6.6a,c). This detail is accounted for in our model, which shows that for the dimensions of the wires used in our experiments, the DW acceleration or deceleration times to reach a steady-state can be significant (on the order of tens of nanoseconds). Subsequently, we see the evolving disparity in the DW displacements in the individual branches in agreement with our experimental results (Fig. 6.6b). The model also predicts that the acceleration time of the slow moving DW is significantly larger than the deceleration time of the fast moving DW, thereby, corroborating the experimental results (Fig. 6.4b).

From our model, we also find that by increasing  $\theta$ , we can launch the DW into the Y-shape branches at an angle further away from the steady-state DW configuration, leading to longer acceleration or deceleration times and consequently, greater  $d_B - d_C$ . This is seen most clearly in Fig. 6.4d where  $d_B - d_C$  at the end of a  $t = 100$  ns pulse for devices with various  $\theta$  are summarized. A systematic increase in  $d_B - d_C$  follows with an increase in  $\theta$  for all  $V_p$ . We also find that

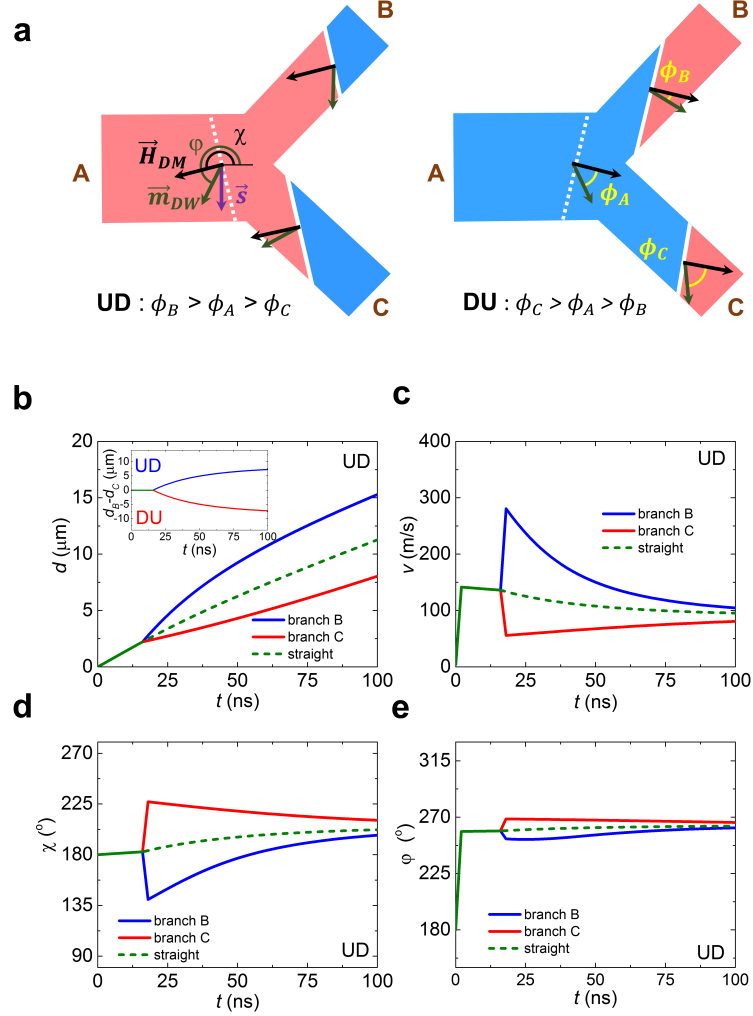


FIGURE 6.6: Extended 1D model. (a) Schematic of a device with an UD (left) and a DU (right) DW initially in the branch A (dashed white line) when current is applied. Spin accumulation (violet) causes the canting of the DW magnetization unit vector,  $\vec{m}_{DW}$  (green) and subsequently the DW tilt. Black arrow indicates the effective DMI field direction  $\vec{H}_{DM}$ , which is always perpendicular to the DW front. After splitting at the Y-shape junction, the DW (solid white line) makes different angles with the  $\vec{m}_{DW}$  in the two branches ( $\phi_B$  and  $\phi_C$ ) than it made initially ( $\phi_A$ ) and thus experiences different effective torques which gives rise to different velocities. Extended 1D simulation for a device (width of branch A is  $5\mu\text{m}$ , width of branches B and C is  $2.5\mu\text{m}$  and  $\theta = 90^\circ$ ) showing time evolution of (b) displacement,  $d$  with the asymmetry  $d_B - d_C$  shown in inset (c) Instantaneous velocity,  $v$  (d) angle of  $\vec{H}_{DM}$ ,  $\chi$  and e, DW magnetization angle,  $\phi$  for an up-down DW as it travels from branch A (solid green) into branches B (blue) and C (red) upon splitting. Results of the motion of a DW in a straight wire are also shown in comparison (dashed green).

$d_B - d_C$  decreases monotonically after reaching a particular  $V_p$  though that exact point does not appear for  $\theta = 30^\circ, 60^\circ$  for the range of  $V_p$  we were able to measure. This suggests that for a particular  $\theta$ , while the DWs in the two branches move with disparate velocities and this difference grows with  $V_p$ , they are also able to attain a steady-state motion faster. The acceleration or deceleration times increase with  $\theta$ , and may cause the downturn in  $d_B - d_C$  to be seen at a higher  $V_p$  as seen in Fig. 6.4d. Finally, this model also confirms that when the width of the nanowire is decreased, the acceleration/deceleration time for a DW decreases and the DW relaxes to its new equilibrium position much faster (Fig. 6.7). Thus, while we acknowledge that our 1D model simulations may not be able to quantify the effects of pinning, or current crowding that may happen at the bifurcation point, by and large, they are able to qualitatively reproduce the key trends we see in our measurements.

In both our experiments and model, we find that a chiral DW travels different distances when injected into the branches of a Y-shaped junction. For the opposite DW configuration, the asymmetry in DW propagation is a mirror inverse of the original one. Hence by incorporating two coupled chiral DWs of the opposite configurations in the same structure, we should be able to nullify the asymmetry caused in the two branches. We do this by forming a synthetic antiferromagnet (SAF) using a Ru spacer layer sandwiched between two Co/Ni/Co layers[80] as follows: 100 AlO<sub>x</sub> / 20 TaN / 15 Pt / 3 Co / 7 Ni / 1.5 Co / 8Ru / 3Co / 7Ni / 3Co / 50 TaN (Fig. 6.8a). By forming a Y-shape junction out of this film structure, we perform current driven motion of DWs and find that the DW travels identical distances in the two branches upon splitting (Fig. 6.8b). This further reinforces the concept that the asymmetry is caused due to the SHE-SOT torques.

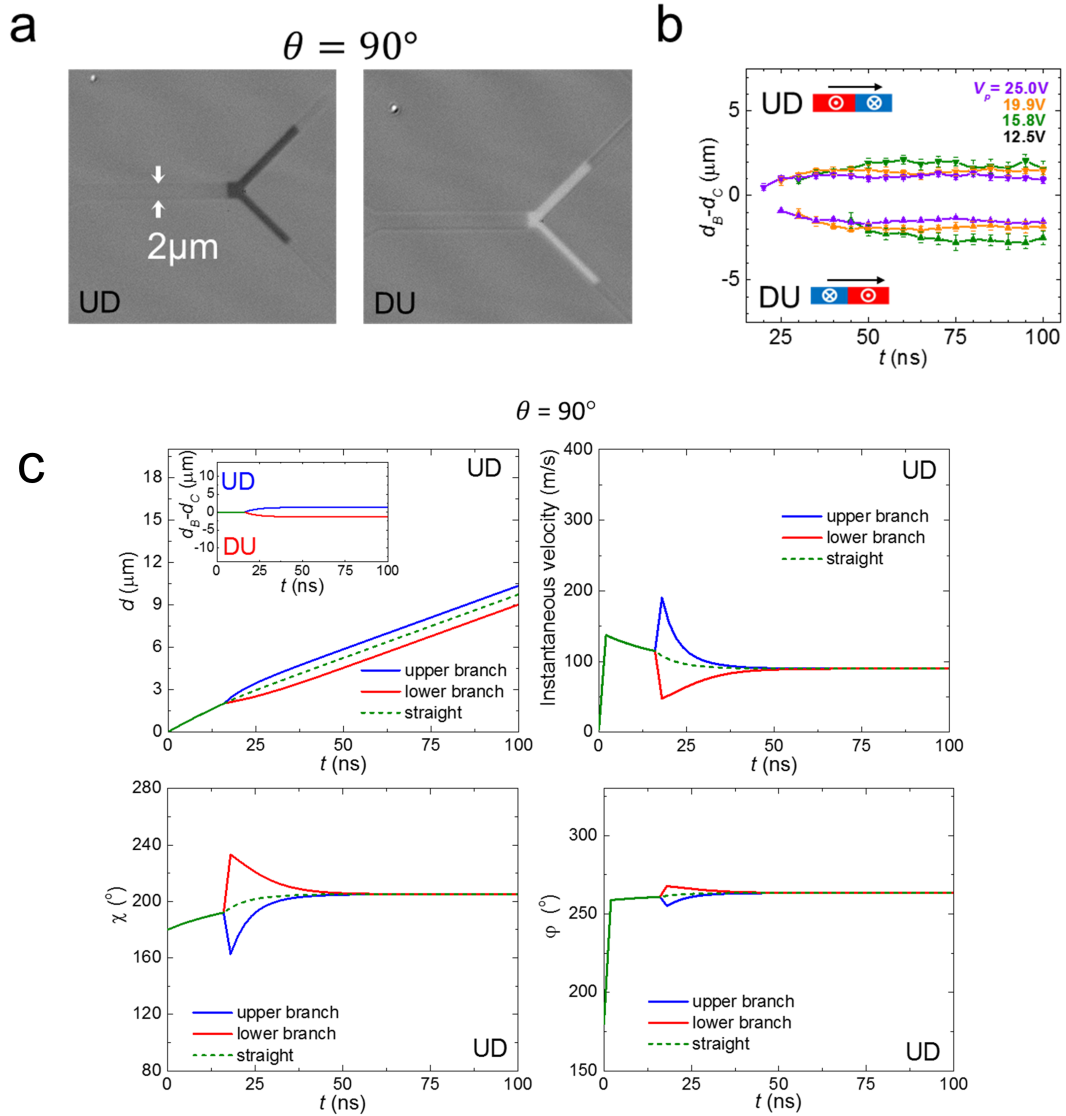


FIGURE 6.7: Influence of width. (a) Kerr images of the measurements taken on a narrower device with branch A width  $2\mu\text{m}$  and branches B and C widths  $1\mu\text{m}$  each for a device with  $\theta = 90^\circ$ . Upon injection from the input branch, the DW displacements in the two output branches are quite similar for both an up-down domain wall (left) and a down-up domain wall (right). (b) Asymmetry  $d_B - d_C$  for the same device. The results show that the timescale for the saturation of  $d_B - d_C$  is shorter compared to the wider device (Fig. 6.4) used in our experiments. (c) Model results for device where branch A width is  $2\mu\text{m}$ , branch B and C width is  $1\mu\text{m}$  and  $\theta=90^\circ$ . The DW reaches its steady-state faster and we see a smaller asymmetry compared to our model results for a device in Fig. 6.6.

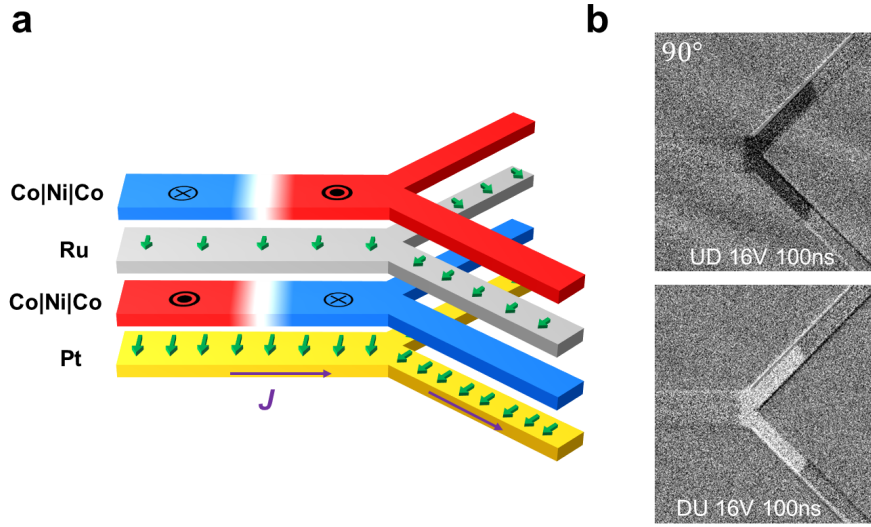


FIGURE 6.8: Symmetric DW motion in synthetic antiferromagnetically (SAF) coupled racetracks (a) Schematic of a SAF structure used in our experiment (b) Representative image for  $\theta = 90^\circ$ ,  $V_p = 16$  V and  $t = 50$  ns showing symmetric injection of the DW into the Y-shape output branches.

### 6.3 A Y-shaped domain sorting device

The controlled manipulation of magnetic domains and domain walls (DWs) by current forms the basis of a number of proposed memory and logic devices[16, 86, 87] for conventional as well as neuromorphic[88] computing. We now demonstrate (Fig. 6.9) that our findings above can be utilized to sort domains of opposite polarities (pair of DWs rather than individual DWs as reported earlier in in-plane soft magnetic nanowires[89, 90] on the basis of significantly different velocities of UD and DU DWs upon entering an output branch. Instead of bringing a single DW near the bifurcation region as in our earlier experiments, we now bring a pair of DWs, i.e., a domain of a predetermined length, and monitor its motion as a pulse of  $V_p = 25$  V and either (i) a series of  $t = 15$  ns or (ii) a single pulse of  $t = 100$  ns is applied across the device. In case (i), the domain splits into two and travels into both output branches B and C (see supplementary movie S1 and

S3 in [85]). This is because both the DWs constituting a domain have time to relax to their zero-current equilibrium state before a subsequent electrical pulse arrives, thereby leading to the lock-step motion of both the DWs. In case (ii), however, in presence of a continuous electrical pulse, an UD DW travels faster in branch B upon entry while it slows down in branch C, whereas a DU DW does the inverse; the DU DW moving faster in branch C can overcome and annihilate the slow moving UD DW for appropriate domain and pulse lengths (see supplementary movie S2 in [85]). For the same reason, due to the velocity difference, the distance between the UD and DU DW gets increased in branch B. This results in sorting of an up domain in branch B (Fig. 6.9a(ii)). Similarly, a down domain can be split (see supplementary movie S3 in [85]) into both the branches or can be sorted (see supplementary movie S4 in [85]) in branch C (Fig. 6.9b(ii)).

By utilizing symmetry breaking, we have shown that a DW, depending on its polarity, can be simultaneously accelerated or decelerated in two identical output branches of Y-shaped magnetic nanowires over rather long time scales and distances, which depends on the angle between the output branches, the current density used to move the DW and the width of the nanowire. Using this simple technique, we can indirectly visualize the temporal evolution of the various torques and their respective effects on the magnetization vector and the velocity of the DW, since ours is a post-facto rather than a real time technique. Furthermore, by designing a voltage pulse sequence, we show that the domain length in a nanowire can be manipulated without any magnetic field thereby allowing for all electrical complex logic in memory devices, where timing of electrical pulses can be encoded in domain lengths. Finally, the asymmetry can be eliminated in a synthetic antiferromagnetic structure having two opposite DWs coupled together.

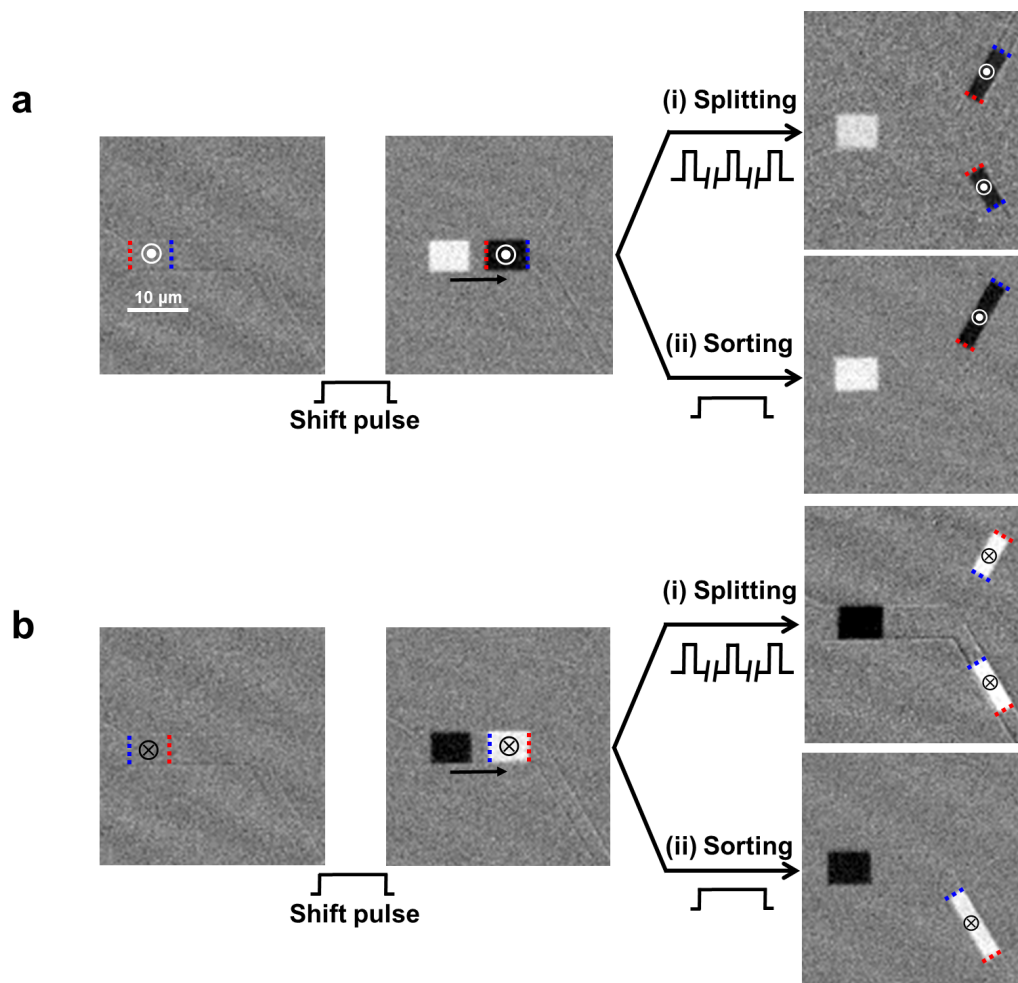


FIGURE 6.9: DW splitting versus sorting. (a) Splitting (i) or sorting (ii) of an up domain by modifying the pulse waveform. For a series of short pulses, both the DWs move in lock-step and during the time the pulse is turned off, the DW magnetization as well as DW profile for both the DWs relax into their respective equilibrium positions before the subsequent short pulse arrives. (ii) For a single pulse, the two DWs travel at different velocities in the two output branches leading to annihilation of the two domain walls in the bottom branch, whereas increase in the domain length in the top branch. (b) Splitting (i) or sorting (ii) of a down domain by modifying the pulse waveform just as discussed in a. The up domain gets sorted in the top branch B, whereas the down domain gets sorted in the bottom branch C. Red and blue dashed lines show the positions of a DU and UD domain wall, respectively, in any given frame.



# Chapter 7

## Conclusions

The controlled manipulation of magnetic moments by charge currents is the key principle behind many proposed memory technologies. There are several approaches in doing so, and one approach which has gained considerable interest recently is the generation of torques derived from spin-orbit interactions. In thin film structures with a heavy metal non-magnetic layer/magnetic underlayer, passing currents through the non-magnetic layer can give rise to spin currents that can be absorbed by the adjoining magnetic layer. These spin currents can efficiently drive chiral Néel domain walls (DWs) stabilized by Dzyaloshinskii Moriya Interaction (DMI) to high velocities of  $\sim 350$  m/s. Reversal of a nanomagnet through DW motion can be used in the operation of magnetic random access memory (MRAM) or racetrack memory devices for fast and low-power operation. As such, investigation of the motion of chiral DWs under spin-orbit torques has been done by various studies to unravel the statics and dynamics of DWs under applied fields and current. Yet no study investigated the current-induced motion of chiral DWs in curvilinear geometries which are required for the operation of some DW devices

such as racetrack memory in two and three-dimensions. The work done in this thesis attempted to fill this gap.

In straight nanowires of an ultrathin ( $<3\text{nm}$ ) perpendicularly magnetized system such as Pt/ Co/ Ni/ Co, chiral DWs move in lock-step motion in response to currents which give rise to spin Hall torque arising from spin-orbit interactions. The synchronized motion of DWs is essential for the transmission of information encoded in the DWs spacing between neighbouring DWs. We designed U-shaped nanowires with a semicircular section of a constant mid-radius and found that while alternating DWs travelled with the same speed in the straight sections, upon entering the curved section, the speeds were vastly different. A  $\otimes|\odot$  DW travelling around a curved wire with a positive curvature travelled faster while it slowed down for the opposite curvature. The reverse happened for a  $\odot|\otimes$ , i.e. it travelled slower for a positive curvature. The difference between the speeds of a DW travelling in opposite curvatures increased with a increase in curvature (or with a decrease in radius), and can vary vastly, reaching a factor of 10 in some cases. As a consequence, two neighbouring DWs travelling through a curved wire either increase or decrease greatly the size of magnetic domain enclosed between them. In some cases, the DWs can come close enough to annihilate each other. Not only are the speeds different, but the threshold current densities to move the two DWs of opposite configuration can also be different.

In order to investigate this effect, we grew structures similar to the ones that were studied but with different thicknesses of Pt/Co layers at the top and bottom interfaces of the magnetic stack. This allowed us to invert the sign of the DMI and spin Hall angle (SHA) in the stack. Since the DW motion in these structures arises from an interplay of DMI and spin Hall torques, we expected this to also play into the effect curvature has on the motion of DWs. Surprisingly, we find that the speeding up or slowing down of DWs remains independent of the overall

sign of the DMI and SHA in the structure. Thus, there is a universal relationship between the effect of curvature on the speed of DW that is independent of the two chiral mechanisms - DMI and spin Hall effect (SHE) - which it originates from.

In the past, studies have shown that current-induced torques can lead to tilting of the DW during motion. This tilting behavior changes the effective driving torque on the magnetization of the DW which is maximum when DMI field vector is orthogonal to the magnetization (the DMI field vector is perpendicular to the DW profile). In straight wires,  $\odot|\otimes$  and  $\otimes|\odot$  DWs tilt oppositely by the same amount, and hence still travel with the same speed. In curved wires, the geometry itself induces tilting of a DW during motion. This tilt results from the disparity in the current density as well as the distance a DW has to travel at the inner and the outer rims of curved wire. When the tilt induced by the curvature cancels the tilt induced by the DMI, the DW speed is increased. In the opposite case, the DW speed is decreased. This physics is captured by a quasi-two dimensional model of DW motion that assumes that a DW can be defined by three parameters, its position, its tilt and its azimuthal magnetization angle. The analytical model is based on moving cylindrical frame that is representative of our curved nanowires. Our model results qualitatively match our experimental results. More specifically, we were able to reproduce 1) The speeding up and slowing down of DWs for opposite curvatures 2) The impact of curvature and width of the wire on DW speed 3) The universal relationship between curvature and its influence on DW speed. We also find that the differences in the DW speed is indeed coming from the different tilting behavior of DWs of opposite curvature along a curvature. In our calculations, the DW tilt angle evolves differently for opposite DWs, resulting in different effective torques, while the DW magnetization angle which is insensitive to curvature is roughly identical.

Our work on the DW motion in curved wires shows a previously unanticipated problem, i.e., there is no longer a lock-step motion of DWs in curved wires, a detrimental problem for the operation of DWs in a racetrack memory device. We manage to solve this problem by designing curved wires made out of synthetic antiferromagnetic (SAF) structures. In such structures, two magnetic layers are coupled antiferromagnetically by the interlayer exchange induced by a Ru spacer layer that is in the middle. A  $\odot|\otimes$  DW in the bottom layer is coupled to a  $\otimes|\odot$  DW in the top layer. During the application of current in the nanowire, a coupled DW in this structure moves without any tilting as the tilt in top layer is cancelled by the tilt in the bottom layer. As a result, the tilting behaviour that is responsible for the curvature-induced speeding up or slowing down of DWs in a curved wire can no longer play a role. In addition to that, the exchange coupling torque, which drives DWs in SAF nanowires does not depend on the tilt angle of the DW, only the relative angle between the DW magnetizations in two layers. Thus, DWs in SAF curved wires move at the same speed as straight wires.

In the last part of this thesis, we show the impact of an abrupt turn, i.e., sudden curvature on the motion of a DW compared to the constant curvature in a curved wire. We do this by designing a Y-shaped structure with a single input branch and two equal output branches. Upon application of a single pulse, a DW entering the input branch splits into two DWs as it enters the two output branches. However, the DW that enters the top branch experiences a curvature equal and opposite to the DW entering the bottom branch. The two DWs travel with different speeds, and travel different distances at a non-equilibrium velocity before entering the steady-state regime of the straight wire. By conducting this experiment with different pulses, we map the time-evolution of the DW dynamics in the non-equilibrium regime and find that the DW can take several tens of nanosecond to reach an equilibrium velocity which increases with the angle between the two

output branches. We use this asymmetric behavior to design a domain biphlexer. Two alternating DWs (or a domain) that are simultaneously injected into the bifurcation point of the Y-shape lead to the annihilation of the DWs in one branch, and an expansion in the other. This arises due to the relative velocity between two DWs during motion. For the opposite domain, the annihilation happens in the other branch. Thus with the domain as the input, depending on its magnetization direction (up or down) we can select which branch it enters.

In summary, by investigating the motion of chiral DWs along curved structures, we have been able to unravel dramatic changes in its motion which are of consequence to the operation of DWs in memory and logic devices. Our work sheds light on the mechanism that is at play for these changes in speed, and also a solution to eliminating this effect. It also provides a new control for manipulating the motion of DWs that is based on geometry rather than by changing materials, which has been the choice for most research studies. In addition, it also solves one unanticipated problem to the implementation of racetrack memory in two or three dimensions. A few other challenges that remain are fabrication and design of a complete architecture for dense storage, reliability of motion, as well as fast motion at low current densities. With the continued amount of active research in this field, I hope to see a commercial product based on DW motion in the next decade.



# Appendix A

## Quasi two-dimensional model for DW tilting in a curved wire

### A.1 Quasi two-dimensional model for DW tilting in a curved wire

The quasi two-dimensional model (Q2D)<sup>1</sup> in curved nanowires used for modelling of DW motion in Chapter 5 is developed by incorporating (1) a moving reference frame with Cartesian coordinates that allows for tilting of the DW to be taken into account, (2) periodic variation in anisotropy to simulate DW pinning, (3) thermal fluctuations in the DW position and magnetization along the wire, and (4) a non-uniform current density transverse to the wire. The basic assumption of our model is that if the DW width is much smaller than the radius of curvature, the DW has a

---

<sup>1</sup>The contents of this chapter have been either adapted or directly taken from my publication: Garg, C., Yang, S.H., Phung, T., Pushp, A. and Parkin, S.S., 2017. Dramatic influence of curvature of nanowire on chiral domain wall velocity. *Science advances*, 3(5), p.e1602804. Reprinted with permission from AAAS.

fixed magnetization profile of polar angle  $\theta$  by which the magnetization is rotated from the direction perpendicular to the layer, i.e. the z-axis, and the azimuthal magnetization angle  $\psi$  is uniform all over the wire at each instant of time when it is manipulated either by current or magnetic field or a combination of the two. In contrast, when the DW width becomes comparable to the radius of curvature of the wire, an additional curvature effect should be taken into account since the azimuthal magnetization angle within DW does not look uniform anymore in the curved wire moving frame coordinate. However, the wires used in our experiment have a few microns of curved radius whilst the DW width parameter is  $\sim 5$  nm. Hence the former assumption is valid since the latter effect is vanishingly small and neglected hereafter. For the case of perpendicularly magnetized nanowires the DW dynamics can be described within the Q2D model by three parameters, namely the position  $q$  of the DW along the nanowire, its conjugate momentum  $2M_s\psi/\gamma$ , where  $\psi$  is the angle of the DW's magnetization in the plane of the wire with respect to the direction  $\hat{x}$ , and the tilting angle  $\chi$  is defined with respect to the direction  $-\hat{y}$  (see Fig. A.1).  $M_s$  is the saturation magnetization and  $\gamma$  is the gyromagnetic ratio. Here, the key point to note is that the DW motion in curved wires is instantaneously governed by the DW magnetization angle  $\phi$ , and tilting angle  $\zeta$ , defined with respect to unit vectors,  $\hat{e}_s$ ,  $\hat{e}_r$  and  $\hat{z}$  in the moving frame coordinates but the DW dynamics is ultimately described by the static Cartesian coordinates in Q2D model because  $\hat{e}_s$  and  $\hat{e}_r$  vary as a function of time and DW position.  $\phi$  and  $\zeta$  are connected to the corresponding parameters,  $\psi$  and  $\chi$ , defined in static Cartesian coordinates, respectively, via DW position  $q$ :  $\phi(t) = \frac{q(t)}{R} + \psi(t)$  and  $\zeta(t) = \frac{q(t)}{R} + \chi(t)$  where  $R$  is the mid-radius of wire (see Fig. S1). As a result, the domain wall profile of curved wires in terms of moving frame parameters is



given by

$$\theta(r, t) = 2 \arctan \exp \left[ \pm \frac{r \left( \xi - \frac{q(t)}{R} \right) \cos \zeta(t) + (r - R) \sin \zeta(t)}{\Delta} \right] \quad (\text{A.1})$$

This can be rewritten by static Cartesian coordinates as following.

$$\theta(x, y, t) = 2 \arctan \exp \left[ \pm \frac{\left( \sqrt{x^2 + y^2} \arctan \frac{y}{x} - q(t) \right) \cos \left( \frac{q(t)}{\sqrt{x^2 + y^2}} + \chi(t) \right) + \left( \sqrt{x^2 + y^2} - R \right) \sin \left( \frac{q(t)}{\sqrt{x^2 + y^2}} + \chi(t) \right)}{\Delta} \right] \quad (\text{A.2})$$

Here the upper and lower signs correspond to the  $\odot|\otimes$  and  $\otimes|\odot$  domain magnetic configurations, respectively, and  $\Delta$  is the domain wall width parameter. It should be noted that the azimuthal magnetization angles  $\phi(t)$  and  $\psi(t)$  do not depend on spatial parameters,  $r$ ,  $x$ , and  $y$ , i.e. uniform as mentioned above. Consequently, the DW defined by eq. (A.1) is not a straight line as seen in Fig. A.1 since the DW tilt angle  $\zeta$  in moving coordinates is constant along the transverse to the wire direction thus showing that the tangent of DW at each point along the DW keeps the same angle with  $-\hat{e}_r$  direction.

### A.1.1 Definition of curvature

In differential geometry, the curvature vector is simply the rate of change of tangent along an arc. The curvature  $\kappa$  in a curved line  $\vec{r}(s) = (x(s), y(s))$  that is a function of a parameter  $s$  in the  $x - y$  plane can be defined as:

$$\kappa = \frac{\frac{dy}{ds} \frac{d^2x}{ds^2} - \frac{dx}{ds} \frac{d^2y}{ds^2}}{\left[ \left( \frac{dx}{ds} \right)^2 + \left( \frac{dy}{ds} \right)^2 \right]^{3/2}} \quad (\text{A.3})$$

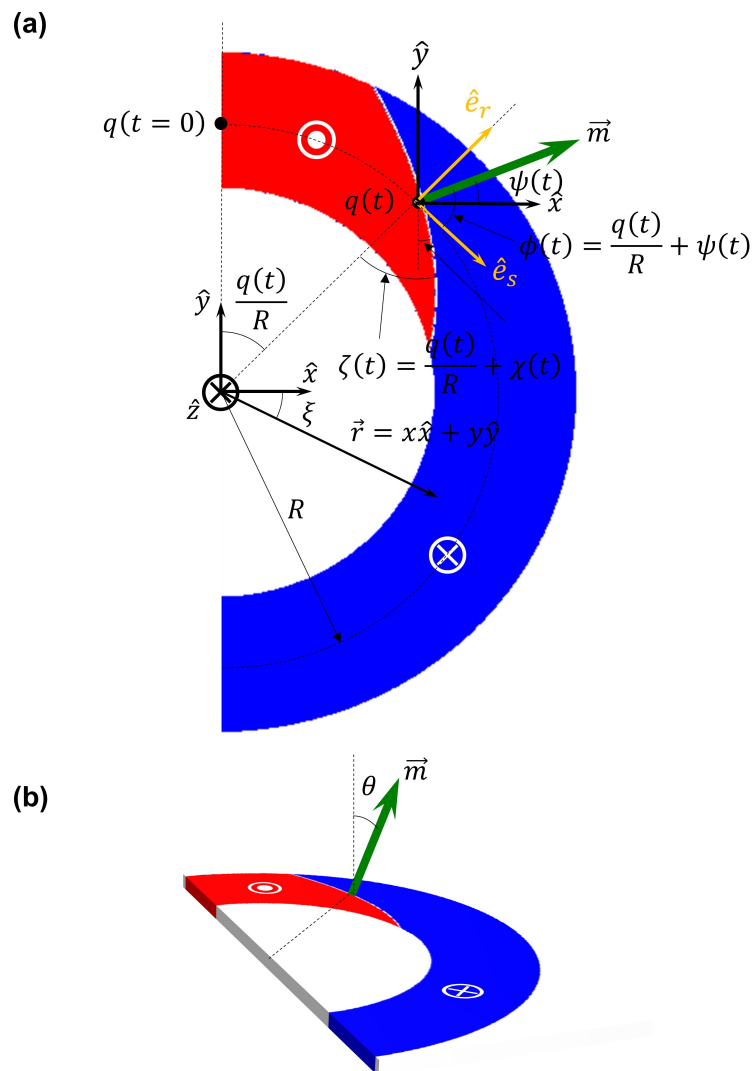


FIGURE A.1: Schematic illustration of basic parameters used in the Q2D model for current driven domain wall motion in top view of curved wires with  $\odot|\otimes$  domain configuration: (a) top view and (b) slanted overview. The moving frame coordinates  $\hat{e}_s$ ,  $\hat{e}_r$  and  $\hat{z}$  are cartooned together with the static Cartesian coordinates  $\hat{x}$ ,  $\hat{y}$  and  $\hat{z}$ .

Since the DW position  $q$  is constrained to lie within the nanowire, we choose  $q$  to describe the curved nanowire  $\vec{r}(s)$ . The time  $t$  can be used for  $s$ , so we set  $s = t$ . Since  $\vec{r}(t) = (R \sin \frac{q}{R}, R \cos \frac{q}{R})$  (see Fig. A.1A) and  $q = \nu t$  in the steady state, then  $\vec{r}(t) = (R \sin \frac{\nu t}{R}, R \cos \frac{\nu t}{R})$ . Finally using  $\frac{d\vec{r}(t)}{dt} = (\nu \cos \frac{\nu t}{R}, -\nu \sin \frac{\nu t}{R})$ , and  $\frac{d^2\vec{r}(t)}{dt^2} = \left(-\frac{\nu^2}{R} \sin \frac{\nu t}{R}, -\frac{\nu^2}{R} \cos \frac{\nu t}{R}\right)$  then we find from eq. A.3, that the curvature  $\kappa$  is given by

$$\kappa = \frac{1}{R} \frac{\nu}{|\nu|} \quad (\text{A.4})$$

Eq. A.4 shows that the curvature  $\kappa$  is positive (negative) when the DW moves clockwise (counter-clockwise). Similarly, if we choose the current density  $J$  to be a parameter that describes  $\vec{r}(t)$ , then we find:

$$\kappa = \frac{1}{R} \frac{J}{|J|} \quad (\text{A.5})$$

Before deriving the equations of motion, let us first discuss the additional effects as shown in Sec. A.1.2-A.1.4 that we have taken into account in development of Q2D model in curved wires.

### A.1.2 Non-uniform anisotropy induced pinning effect

The threshold current density above which the DWs start to be depinned and move by current is zero in the absence of any pinning. Since the curved nanowire devices we measured do not have any artificial notches or blips, we consider the intrinsic DW pinning only. There are various intrinsic sources that cause DW pinning. Among them we make use of the periodic variation of anisotropy  $K_{eff} = K_{eff}^0 \left[1 - \eta \cos \frac{2\pi(q-q_s)}{q_0}\right]$  along the length of wire to simulate pinning since it is the major factor that give rise to the broadening of ferromagnetic resonances (FMR) spectrum linewidth, that is, so-called inhomogeneous broadening. Here  $\eta$ ,  $q_s$  and

$q_0$  are the strength, center position and period of anisotropy, respectively (see Fig. A.2). The pinning field induced by the periodic anisotropy is  $H_{pin} = \frac{4\pi\Delta\eta K_{eff}^0}{q_0 M_s}$  where  $M_s$  is the saturation magnetization. Based on our fitted parameters, we have  $H_{pin}$  560 Oe that is consistent with 5-10% of anisotropy field  $H_K \sim 1$  T of our film since the inhomogeneous broadening is known to correspond to this proportion of  $H_K$ [91].

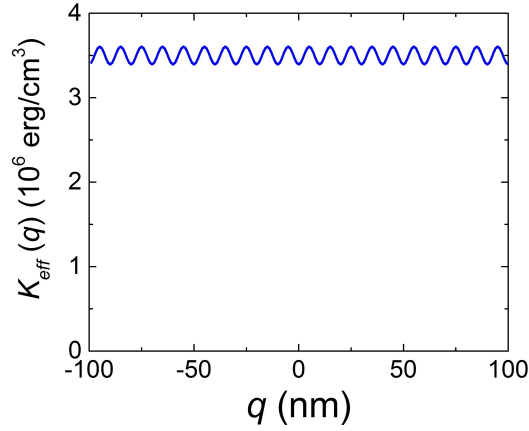


FIGURE A.2: Profile of anisotropy constant  $K_{eff}(q)$  with  $K_{eff}^0=3.5\times 10^6$  erg/cm<sup>3</sup>,  $\eta=0.03$ ,  $q_s=0$  nm, and  $q_0=10$  nm.

### A.1.3 Thermal broadening

At finite temperatures, thermal fluctuations are known to induce normal distributions (Gaussians) of the initial position  $q$  and magnetization angle  $\psi$  of DW[92]. The distribution Gaussians can be derived as (see Fig. A.3a,b):

$$P(q_{initial}) = \sqrt{\frac{M_s H_{c0} \omega t_m}{\pi q_0 k_B T}} \exp\left(-\frac{M_s H_{c0} \omega t_m q_{initial}^2}{q_0 k_B T}\right)$$

$$Z(\psi_{initial}) = \sqrt{\frac{M_s H_{c0} \omega t_m \Delta}{2 k_B T}} \exp\left(-\frac{M_s H_{c0} \omega t_m \Delta \psi_{initial}^2}{q_0 k_B T}\right)$$

where  $w$  is the width of wire,  $t_m$  is the thickness of magnetic film,  $H_{c0}$  is the propagation field,  $k_B$  is the Boltzmann constant,  $q_{initial}$  and  $\psi_{initial}$  are the initial condition of DW position and azimuthal angle of magnetization, respectively. Since the sample temperature  $T$  is proportional to the power applied to the wire,  $T \propto J^2$  where  $J$  is the current density and we use  $T(J=0)=300$  K, and  $T(J=2 \times 10^8 \text{ A/cm}^2)=500$  K (see Fig. A.3c). The thermal broadening effect is implemented in the Q2D model by meshing  $q_{initial}$  and  $\psi_{initial}$  around  $q_{initial} = 0$  and  $\psi_{initial} = 0$ , calculating the results at each mesh point and then averaging them weighted by the Gaussians as following:

$$X = \frac{\sum_{i,j} X_{ij} P(q_{initial,i}) Z(\psi_{initial,j})}{\sum_{i,j} P(q_{initial,i}) Z(\psi_{initial,j})}$$

where  $X = q$ ,  $\psi$ , and  $\chi$ . Note that the thermal effect makes difference only near the critical current density since it plays a key role in depinning of DWs.

#### A.1.4 Non-uniform current distribution

When an electrical current is flowed along a metallic curved wire, the current density is not uniform along the transverse direction to the wire. This happens because (1) electrons, majority carriers in metals, would flow along the gradient of electrical potential, that is, the arc direction, and consequently (2) the resistance linearly increases with the increasing radius. For example, when a voltage  $V$  is applied to one end of curved wire having thickness  $t_f$ , mid-radius  $R$ , width  $w$ , and resistivity  $\rho$  while the other end is grounded (see Fig. A.4), the current  $dI$  that flows along the cross section  $t_f dr$  at radius  $r$  is  $dI = \frac{V t_f dr}{\pi \rho r}$ . Hence the current density  $J(r)$  at radius  $r$  is  $J(r) = \frac{dI}{t_f dr} = \frac{V}{\pi \rho r}$ , that is,  $J(r) \propto \frac{1}{r}$ . Hence the total current  $I$  is  $I = \int_{R-\frac{w}{2}}^{R+\frac{w}{2}} dI = \int_{R-\frac{w}{2}}^{R+\frac{w}{2}} \frac{V t_f}{\pi \rho r} dr = \frac{V t_f}{\pi \rho} \log \frac{2R+w}{2R-w}$ . Note that in a  $\pi R$

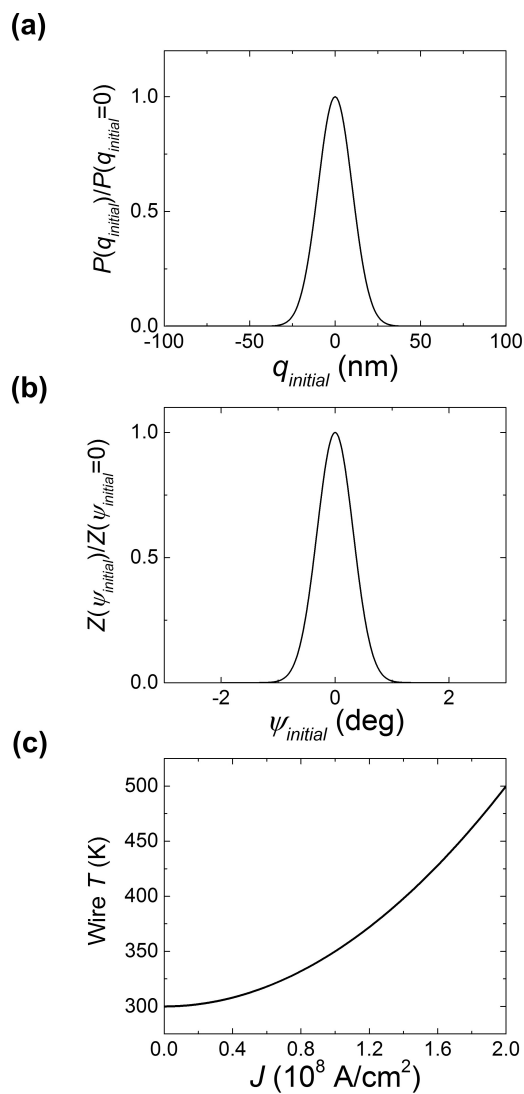


FIGURE A.3: Profile of normalized (a)  $P(q_{initial})$  and (b)  $Z(\psi_{initial})$  with  $T=500$ K,  $H_{c0}=20$  Oe,  $q_0=10$  nm,  $\Delta=5$  nm,  $M_s=580$  Oe,  $w=2$   $\mu$ m, and  $t=1$  nm. (c) Plot of wire temperature vs. current density  $J$ .

long straight wire the total current  $I$  is  $I = \frac{V t_f w}{\pi \rho R}$ . The fact that  $\log \frac{2R+w}{2R-w} > \frac{w}{R}$  leads to that  $I_{curve} > I_{straight}$  with given same length and voltage. Based on this calculation, we have implemented the non-uniform current density in Q2D model by setting  $H_{SH}(r) = \frac{R}{r} H_{SH}^0$  where  $H_{SH}^0$  is  $H_{SH}(r = R)$ . We will derive the Q2D equations of motion later and discuss the parameter  $H_{SH}^0$  in detail there. Since the conventional volume spin transfer torque (V-STT) is significantly smaller than spin-orbit torque in our system, we do not take the non-uniform current distribution effect into account in V-STT.

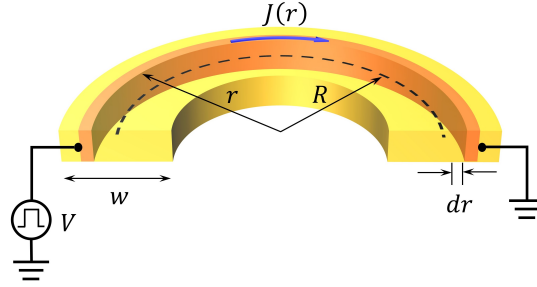


FIGURE A.4: Schematic of current distribution in curved wire with width  $w$  and mid-radius  $R$ . A voltage  $V$  is applied on the left end while the right end is grounded.

### A.1.5 Lagrangian and Equations of Motion

First, we formulate the Lagrangians that include the adiabatic and non-adiabatic spin transfer torques, external field driven torques, the spin Hall current torque, and the Dzyaloshinskii-Moriya exchange field. The equations of motion are then derived by Lagrange-Rayleigh equations[93].

With the DW profile function (A.1), the Lagrangian  $\mathcal{L}$  in the curve wire that contains the magnetostatic potential energy considering inhomogeneous anisotropy, DW kinetic energy and adiabatic spin-transfer torque is given by

$$\begin{aligned}
\mathcal{L} &= \int \int \left[ E + \frac{M_s}{\gamma} \phi \dot{\theta} \sin\theta - \frac{uM_s}{\gamma} \phi \frac{d\theta}{ds} \sin\theta \right] ds dr \\
&= \frac{2wA}{\Delta} \sec\zeta \left[ 1 + \left( \frac{4R^2}{4R^2 - w^2} \right) \sin^2\zeta + \frac{\pi^2}{3} \frac{\Delta^2}{4R^2 - w^2} \right] \\
&+ 2w\Delta K_{eff}^0 \left\{ 1 - \eta \cos \left[ \frac{2\pi(q - q_s)}{q_0} \right] \right\} \sec\zeta + w\Delta M_s H_k \cos^2(\psi - \chi) \sec\zeta \\
&\mp 2M_s H_z wq - \pi w\Delta M_s H_p \cos(\psi - \psi_H) \sec\zeta - \pi w\Delta M_s H_{DM} \cos(\psi - \chi) \sec\zeta \\
&\mp \frac{2wM_s}{\gamma} \phi (\dot{q} + u)
\end{aligned} \tag{A.6}$$

Here the upper and lower signs correspond to the  $\odot|\otimes$  and  $\otimes|\odot$  domain magnetic configurations, respectively.  $s$  is the coordinate position along the wire length direction.  $E$  is the magnetostatic energy density of domain wall per area and is given by

$$\begin{aligned}
E &= A(\nabla \vec{m})^2 + K_{eff} \left[ 1 - \eta \cos \frac{2\pi(q - q_s)}{q_0} \right] \sin^2\theta + \frac{M_s H_k}{2} \sin^2\theta \cos^2(\psi - \chi) \\
&- M_s H_z \cos\theta - M_s H_p \sin\theta \cos(\psi - \psi_H) - M_s H_{DM} \sin\theta \cos(\psi - \chi)
\end{aligned} \tag{A.7}$$

Eq. (A.6) can be rewritten as  $\mathcal{L} = \sigma + \int \int \left[ \frac{M_s}{\gamma} \phi \dot{\theta} \sin\theta - \frac{uM_s}{\gamma} \phi \frac{d\theta}{ds} \sin\theta \right] ds dr$  where the magnetostatic potential energy  $\sigma = \int \int E ds dr$ .  $A$  is the exchange stiffness,  $H_k$  is the magnitude of the in-plane anisotropy field derived from the shape anisotropy of the DW that favors a Bloch DW configuration over that of a Néel wall,  $H_z$  is the out-of-plane field,  $H_p$  and  $\psi_H$  are the in-plane magnetic field and its angle defined with respect to  $+\hat{x}$  direction.  $H_{DM}$  is the Dzyaloshinskii–Moriya interaction exchange field at the DW whose direction is always perpendicular to DW length direction thus favoring Néel type wall but the sign depends on domain configurations establishing the chirality of domain walls. The volume spin transfer



torque from the current within magnetic layer is parameterized by  $= \frac{\mu_B P J}{e M_s}$ , where  $\mu_B$  is the Bohr magneton,  $e$  is the electron charge,  $P$  is the spin polarization of the current and  $J$  is the current density in the magnetic layer. Note that  $\sigma$  is a function of DW position  $q$ , i.e.  $\frac{\partial \sigma}{\partial q} \neq 0$  and a finite pressure torque in curved wires, which is distinct from the straight wire even in the absence of Zeeman exchange field  $H_z$ . This is due to the fact that the domain wall energy varies depending on  $q$  since e.g. the DW tilt angle  $\zeta$  changes as a function of  $q$ . Meanwhile, the dissipative function  $\mathcal{F}$  that includes damping, non-adiabatic spin-transfer torque and spin-orbit torque is given by

$$\begin{aligned}
\mathcal{F} &= \int \int \frac{\alpha M_s}{2\gamma} \left[ \left( \frac{d}{dt} - \frac{\beta u}{\alpha} \frac{d}{ds} \right) \vec{m} + \frac{\gamma}{\alpha} H_{SH} \vec{m} \times \hat{e}_r \right] ds dr \\
&= \frac{\alpha M_s}{2\gamma} \left[ \frac{2w\dot{q}^2}{\Delta} \left[ \frac{w^2}{12R^2} \sin\zeta \tan^3\zeta + \cos\zeta \right] \right. \\
&\quad \left. + \frac{wq\dot{\chi}}{3R\Delta} \sin\zeta \tan\zeta \left\{ w^2 \left[ \sec^2\zeta - \frac{2q}{R} \tan\zeta \right] + \pi^2 \Delta^2 \sec^2\zeta \right\} \right. \\
&\quad \left. + \frac{w\dot{\chi}^2}{6\Delta} \sec^3\zeta \left[ w^2 + \pi^2 \Delta^2 \sin^2\zeta \right] + 2w\Delta\dot{\phi}^2 \sec\zeta \right. \\
&\quad \left. \pm \frac{2\pi\gamma}{\alpha} H_{SH}^0 \cos\phi \left[ \dot{q} \left[ \tan^2\zeta \left( R \log \frac{2R+w}{2R-w} - w \right) + R \log \frac{2R+w}{2R-w} \right] \right. \right. \\
&\quad \left. \left. + \dot{\chi} R \sec^2\zeta \left( R \log \frac{2R+w}{2R-w} - w \right) \right] + \frac{4\beta u}{\alpha \Delta} \dot{q} w \cos\zeta \right. \\
&\quad \left. \mp \frac{\pi\beta u}{2\alpha} \cos\phi \left\{ \dot{q} \left[ \frac{1}{R} \tan^2\zeta \left( R \log \frac{2R+w}{2R-w} - w \right) + \log \frac{2R+w}{2R-w} \right] \right\} \right. \\
&\quad \left. + \dot{\chi} \sec^2\zeta \left( R \log \frac{2R+w}{2R-w} - w \right) - \frac{4\beta u \Delta}{\alpha} \dot{\phi} \sin^2\phi \sec\zeta \log \frac{2R+w}{2R-w} \right]
\end{aligned} \tag{A.8}$$

Here again the upper and lower signs correspond the  $\odot|\otimes$  and  $\otimes|\odot$  domain magnetic configurations, respectively,  $\beta$  is the non-adiabatic STT coefficient. The spin Hall effect is parameterized by an effective field  $H_{SH}^0$  in the mid-wire that is given by  $H_{SH}^0 = \frac{\hbar \theta_{SH} J_{UL}}{2e M_s t}$  where  $\hbar$  is  $\frac{h}{2\pi}$ ,  $h$  is Planck constant,  $J_{UL}$  is the current density in the underlayer,  $t$  is the thickness of magnetic layer, and  $\theta_{SH}$  is the spin Hall

angle (or the effective spin Hall angle that describes the magnitude of the spin accumulation that the magnetic layer is subjected to). Note that the accumulated spin from the spin Hall current is oriented along transverse to the wire length  $s$ , i.e. the radial direction  $\hat{e}_r$ . The spin-orbit torque related term written in blue in eq. (A.8) becomes  $\pm \frac{2\pi\gamma w}{\alpha} H_{SH}^0 \dot{q} \cos\phi$  when current distribution is uniform.

Based on Lagrangians  $\mathcal{L}$  and dissipated function  $\mathcal{F}$  obtained above, the Lagrange-Rayleigh equations  $\frac{\partial \mathcal{L}}{\partial X} - \frac{d}{dt} \left( \frac{\partial \mathcal{L}}{\partial \dot{X}} \right) + \frac{\partial \mathcal{F}}{\partial X} = 0$  ( $X = q, \psi$ , and  $\chi$ ) finally lead to the equations of motion as following;

$$\begin{aligned}
& \alpha \dot{q} \left( \frac{w^2}{12R^2} \sin\zeta \tan^3\zeta + \cos\zeta \right) \pm \Delta \dot{\psi} \\
& + \frac{\alpha}{12R} \dot{\chi} \sin\zeta \tan\zeta \left[ w^2 \left( \sec^2\zeta - \frac{2q}{R} \tan\zeta \right) + \pi^2 \Delta^2 \sec^2\zeta \right] = \pm \gamma \Delta H_z \\
& - \beta u \cos\zeta \pm \frac{u\Delta}{R} \pm \frac{\pi\beta u \Delta}{4w} \cos\phi \left\{ \frac{1}{R} \tan^2\zeta \left( R \log \frac{2R+w}{2R-w} - w \right) + \log \frac{2R+w}{2R-w} \right\} \\
& + \frac{\beta u \Delta^2}{wR} \sin^2\phi \sec\zeta \log \frac{2R+w}{2R-w} - \frac{\gamma A}{RM_s} \left\{ \sec\zeta \left\{ \tan\zeta \left[ 1 \right. \right. \right. \\
& + \left. \left. \left. \left( \frac{4R^2}{4R^2 - w^2} - 1 \right) \sin^2\zeta + \frac{\pi^2}{3} \frac{\Delta^2}{4R^2 - w^2} \right] \right\} \right. \\
& + \left. \left. \left. \left( \frac{4R^2}{4R^2 - w^2} - 1 \right) \sin 2\zeta \right\} - \frac{\gamma \Delta^2}{2RM_s} \left[ 2K_{eff}^0 \left\{ 1 - \eta \cos \left[ \frac{2\pi(q - q_s)}{q_0} \right] \right\} \right] \right\} \\
& + M_s H_k \cos^2(\psi - \chi) - \pi M_s H_p \cos(\psi - \psi_p) - \pi M_s H_{DM} \cos(\psi - \chi) \left. \right] \sec\zeta \tan\zeta \\
& - \frac{2\pi\gamma\eta\Delta^2}{q_0 M_s} K_{eff}^0 \sin \left[ \frac{2\pi(q - q_s)}{q_0} \right] \sec\zeta \\
& \mp \frac{\pi}{2w} \gamma \Delta H_{SH}^0 \cos\phi \left[ \tan^2\zeta \left( R \log \frac{2R+w}{2R-w} - w \right) + R \log \frac{2R+w}{2R-w} \right] \left. \right\}
\end{aligned} \tag{A.9}$$

$$\begin{aligned}
& \left( \cos\zeta + \frac{\alpha\Delta}{R} \right) \dot{q} + \alpha\Delta\dot{\psi} = \\
& -u \mp \frac{\beta u \Delta}{w} \sin^2\phi \log \frac{2R+w}{2R-w} \pm \frac{\gamma\Delta}{2} \left[ -H_k \sin 2(\psi - \chi) \right. \\
& \left. + \pi H_p \sin(\psi - \psi_H) + \pi H_{DM} \sin(\psi - \chi) \right]
\end{aligned} \tag{A.10}$$

$$\begin{aligned}
& \frac{\alpha}{12R} \dot{q} \sin\zeta \tan\zeta \left[ w^2 \left( \sec^2\zeta - \frac{2q}{R} \tan\zeta \right) + \pi^2 \Delta^2 \sec^2\zeta \right] \\
& + \frac{\alpha}{12} \dot{\chi} \sec^3\zeta \left( w^2 + \pi^2 \Delta^2 \sin^2\zeta \right) \\
& = -\frac{\gamma A}{M_s} \sec\zeta \left\{ \tan\zeta \left[ 1 + \left( \frac{4R^2}{4R^2 - w^2} - 1 \right) \sin^2\zeta + \frac{\pi^2}{3} \frac{\Delta^2}{4R^2 - w^2} \right] \right. \\
& \left. + \left( \frac{4R^2}{4R^2 - w^2} - 1 \right) \sin 2\zeta \right\} - \frac{\gamma \Delta^2 K_{eff}^0}{M_s} \left\{ 1 - \eta \cos \left[ \frac{2\pi(q - q_s)}{q_0} \right] \right\} \sec\zeta \tan\zeta \\
& - \frac{\gamma \Delta^2 H_k}{2} \cos(\psi - \chi) \sec\zeta \left[ \cos(\psi - \chi) \tan\zeta + 2\sin(\psi - \chi) \right] \\
& + \frac{\gamma \pi \Delta^2 H_p}{2} \cos(\psi - \psi_H) \sec\zeta \tan\zeta + \frac{\gamma \pi \Delta^2 H_{DM}}{2} \sec\zeta \left[ \sin(\psi - \chi) \right. \\
& \left. + \cos(\psi - \chi) \tan\zeta \right] \mp \frac{\gamma \Delta \pi R H_{SH}^0}{2w} \cos\phi \sec^2\zeta \left( R \log \frac{2R+w}{2R-w} - w \right) \\
& + \frac{\Delta \pi \beta u}{8w} \sec\zeta \left( R \log \frac{2R+w}{2R-w} - w \right)
\end{aligned} \tag{A.11}$$

Here again the upper and lower signs correspond the  $\odot|\otimes$  and  $\otimes|\odot$  domain magnetic configurations, respectively. In case of uniform current distribution, the spin-orbit torque related terms written in blue in eqs. (A.9) and (A.11) become  $\mp \frac{\pi}{2} \gamma \Delta H_{SH}^0 \cos\phi$  and 0, respectively.

When  $R \rightarrow \infty$ , the eqs. (A.9)-(A.11) become

$$\frac{\alpha \cos \chi_s}{\Delta} \dot{q} \pm \dot{\psi} = \pm \gamma H_z - \frac{2\pi\gamma\eta\Delta^2}{q_0 M_s} K_{eff} \sin \frac{2\pi(q - q_s)}{q_0} \sec \chi - \frac{\beta u}{\Delta} \cos \chi \mp \frac{\pi}{2} \gamma H_{SH} \cos \psi \quad (\text{A.12})$$

$$\begin{aligned} \frac{\cos \chi_s}{\Delta} \dot{q} \mp \alpha \dot{\psi} &= -\frac{u}{\Delta} \cos \chi \mp \frac{\gamma}{2} H_k \sin 2(\psi - \chi) \pm \frac{\pi}{2} \gamma H_p \sin(\psi - \psi_H) \\ &\pm \frac{\pi}{2} \gamma H_{DM} \sin(\psi - \chi) \end{aligned} \quad (\text{A.13})$$

$$\begin{aligned} \frac{\pi^2}{6\gamma} \alpha M_s \Delta \left[ \left( \frac{w}{\Delta\pi} \right)^2 \sec^2 \chi + \tan^2 \chi \right] \dot{\chi} &= \\ - \left[ \frac{2A}{\Delta} + 2K_{eff} \Delta + M_s H_k \Delta \sin(\psi - \chi) + \pi M_s H_{DM} \Delta \cos(\psi - \chi) \right] \tan \chi \\ - H_k M_s \Delta \sin 2(\psi - \chi) + \pi \Delta M_s H_p \sin(\psi - \psi_H) + \pi \Delta M_s H_{DM} \sin(\psi - \chi) \end{aligned} \quad (\text{A.14})$$

These eqs. (A.12)-(A.14) correspond to the equations of motion for straight wires[79].

Note that as for straight wire, the magnetostatic potential energy  $\sigma$  does not depend on  $q$  so that the pressure torque driven DW velocity  $\nu_{pressure} = -\frac{\alpha\gamma\Delta}{2M_s} \frac{\partial\sigma}{\partial q}$  is zero in the absence of  $H_z$  and periodic variation of anisotropy. However, in curve wires  $\sigma$  is a function of  $q$  entirely due to curvature effect, i.e.,  $\nu_{pressure} \neq 0$ , even when  $H_z = 0$  and  $\eta = 0$ .

The parameters used for Q2D simulations are mostly based on our past work[36, 39] :  $\Delta=5$  nm,  $t_p=50$  ns,  $\alpha=0.1$ ,  $\beta=0$ ,  $\eta=0$ ,  $K_{eff}=3.5 \times 10^6$  erg/cm<sup>3</sup>,  $H_k=1,000$  Oe,  $H_{SH}$  ( $J = 1.4 \times 10^8$  A/cm<sup>2</sup>)=700 Oe,  $H_{DM}=1,000$  Oe,  $M_s=580$  emu/cm<sup>3</sup>,  $H_{c0} = 20$  Oe,  $\eta = 0.03$  and  $q_s = 0$  nm.

# Bibliography

- [1] A. H. Eschenfelder, *Magnetic bubble technology*, vol. 14. Springer Science & Business Media, 2012.
- [2] A. Paoletti *et al.*, *Physics of Magnetic Garnets: Proceedings of the International School of Physics' Enrico Fermi', Course LXX, Varenna on Lake Como, Villa Monastero, 27th June-9th July 1977*. Elsevier Science & Technology, 1978.
- [3] P. Chaudhari, J. Cuomo, and R. Gambino, "Amorphous metallic films for bubble domain applications," *IBM Journal of Research and Development*, vol. 17, no. 1, pp. 66–68, 1973.
- [4] C. Bajorek and R. Kobliska, "Amorphous materials for micrometer and sub-micrometer bubble domain technology," *IBM Journal of Research and Development*, vol. 20, no. 3, pp. 271–281, 1976.
- [5] L. Berger, "Emission of spin waves by a magnetic multilayer traversed by a current," *Physical Review B*, vol. 54, no. 13, p. 9353, 1996.
- [6] J. C. Slonczewski, "Current-driven excitation of magnetic multilayers," *Journal of Magnetism and Magnetic Materials*, vol. 159, no. 1-2, pp. L1–L7, 1996.

- 
- [7] M. Hayashi, L. Thomas, R. Moriya, C. Rettner, and S. S. Parkin, “Current-controlled magnetic domain-wall nanowire shift register,” *Science*, vol. 320, no. 5873, pp. 209–211, 2008.
- [8] S. Fukami, T. Suzuki, N. Ohshima, K. Nagahara, and N. Ishiwata, “Intrinsic threshold current density of domain wall motion in nanostrips with perpendicular magnetic anisotropy for use in low-write-current mrams,” *IEEE Transactions on Magnetics*, vol. 44, no. 11, pp. 2539–2542, 2008.
- [9] J. A. Currivan, Y. Jang, M. D. Mascaró, M. A. Baldo, and C. A. Ross, “Low energy magnetic domain wall logic in short, narrow, ferromagnetic wires,” *IEEE Magnetics Letters*, vol. 3, pp. 3000104–3000104, 2012.
- [10] S. Parkin, X. Jiang, C. Kaiser, A. Panchula, K. Roche, and M. Samant, “Magnetically engineered spintronic sensors and memory,” *Proceedings of the IEEE*, vol. 91, no. 5, pp. 661–680, 2003.
- [11] A. D. Kent and D. C. Worledge, “A new spin on magnetic memories,” *Nature nanotechnology*, vol. 10, no. 3, p. 187, 2015.
- [12] S. Fukami, T. Suzuki, K. Nagahara, N. Ohshima, Y. Ozaki, S. Saito, R. Nebashi, N. Sakimura, H. Honjo, K. Mori, *et al.*, “Low-current perpendicular domain wall motion cell for scalable high-speed mram,” in *VLSI Technology, 2009 Symposium on*, pp. 230–231, IEEE, 2009.
- [13] S. S. Parkin, M. Hayashi, and L. Thomas, “Magnetic domain-wall racetrack memory,” *Science*, vol. 320, no. 5873, pp. 190–194, 2008.
- [14] S. Parkin and S.-H. Yang, “Memory on the racetrack,” *Nature nanotechnology*, vol. 10, no. 3, p. 195, 2015.

- 
- [15] N. A. Spaldin, *Magnetic materials: fundamentals and applications*. Cambridge University Press, 2010.
- [16] A. Malozemoff and J. Slonczewski, *Magnetic Domain Walls in Bubble Materials: Advances in Materials and Device Research*, vol. 1. Academic press, 2016.
- [17] A. Hubert and R. Schäfer, *Magnetic domains: the analysis of magnetic microstructures*. Springer Science & Business Media, 2008.
- [18] A. Thiaville, J. Garcia, and J. Miltat, “Domain wall dynamics in nanowires,” *Journal of Magnetism and Magnetic Materials*, vol. 242, pp. 1061–1063, 2002.
- [19] R. D. McMichael and M. J. Donahue, “Head to head domain wall structures in thin magnetic strips,” *IEEE Transactions on Magnetics*, vol. 33, no. 5, pp. 4167–4169, 1997.
- [20] A. Thiaville, Y. Nakatani, J. Miltat, and Y. Suzuki, “Micromagnetic understanding of current-driven domain wall motion in patterned nanowires,” *EPL (Europhysics Letters)*, vol. 69, no. 6, p. 990, 2005.
- [21] M. Johnson, P. Bloemen, F. Den Broeder, and J. De Vries, “Magnetic anisotropy in metallic multilayers,” *Reports on Progress in Physics*, vol. 59, no. 11, p. 1409, 1996.
- [22] P. Carcia, A. Meinhaldt, and A. Suna, “Perpendicular magnetic anisotropy in pd/co thin film layered structures,” *Applied Physics Letters*, vol. 47, no. 2, pp. 178–180, 1985.
- [23] P. Carcia, “Perpendicular magnetic anisotropy in pd/co and pt/co thin-film layered structures,” *Journal of applied physics*, vol. 63, no. 10, pp. 5066–5073, 1988.

- 
- [24] S.-W. Jung, W. Kim, T.-D. Lee, K.-J. Lee, and H.-W. Lee, “Current-induced domain wall motion in a nanowire with perpendicular magnetic anisotropy,” *Applied Physics Letters*, vol. 92, no. 20, p. 202508, 2008.
- [25] M. DeJong and K. Livesey, “Analytic theory for the switch from bloch to néel domain wall in nanowires with perpendicular anisotropy,” *Physical Review B*, vol. 92, no. 21, p. 214420, 2015.
- [26] E. Martinez, L. Torres, and L. Lopez-Diaz, “Oscillator based on pinned domain walls driven by direct current,” *Physical Review B*, vol. 83, no. 17, p. 174444, 2011.
- [27] T. Koyama, D. Chiba, K. Ueda, K. Kondou, H. Tanigawa, S. Fukami, T. Suzuki, N. Ohshima, N. Ishiwata, Y. Nakatani, *et al.*, “Observation of the intrinsic pinning of a magnetic domain wall in a ferromagnetic nanowire,” *Nature materials*, vol. 10, no. 3, p. 194, 2011.
- [28] I. Dzyaloshinsky, “A thermodynamic theory of “weak” ferromagnetism of antiferromagnetics,” *Journal of Physics and Chemistry of Solids*, vol. 4, no. 4, pp. 241–255, 1958.
- [29] T. Moriya, “Anisotropic superexchange interaction and weak ferromagnetism,” *Physical Review*, vol. 120, no. 1, p. 91, 1960.
- [30] M. Bode, M. Heide, K. Von Bergmann, P. Ferriani, S. Heinze, G. Bihlmayer, A. Kubetzka, O. Pietzsch, S. Blügel, and R. Wiesendanger, “Chiral magnetic order at surfaces driven by inversion asymmetry,” *Nature*, vol. 447, no. 7141, p. 190, 2007.
- [31] M. Heide, G. Bihlmayer, and S. Blügel, “Dzyaloshinskii-moriya interaction accounting for the orientation of magnetic domains in ultrathin films: Fe/w(110),” *Physical Review B*, vol. 78, no. 14, p. 140403, 2008.



- 
- [32] P. Ferriani, K. Von Bergmann, E. Vedmedenko, S. Heinze, M. Bode, M. Heide, G. Bihlmayer, S. Blügel, and R. Wiesendanger, “Atomic-scale spin spiral with a unique rotational sense: Mn monolayer on w (001),” *Physical review letters*, vol. 101, no. 2, p. 027201, 2008.
- [33] K. Zakeri, Y. Zhang, J. Prokop, T.-H. Chuang, N. Sakr, W. Tang, and J. Kirschner, “Asymmetric spin-wave dispersion on fe (110): direct evidence of the dzyaloshinskii-moriya interaction,” *Physical review letters*, vol. 104, no. 13, p. 137203, 2010.
- [34] I. M. Miron, T. Moore, H. Szambolics, L. D. Buda-Prejbeanu, S. Auffret, B. Rodmacq, S. Pizzini, J. Vogel, M. Bonfim, A. Schuhl, *et al.*, “Fast current-induced domain-wall motion controlled by the rashba effect,” *Nature materials*, vol. 10, no. 6, p. 419, 2011.
- [35] A. Thiaville, S. Rohart, É. Jué, V. Cros, and A. Fert, “Dynamics of dzyaloshinskii domain walls in ultrathin magnetic films,” *EPL (Europhysics Letters)*, vol. 100, no. 5, p. 57002, 2012.
- [36] K.-S. Ryu, L. Thomas, S.-H. Yang, and S. Parkin, “Chiral spin torque at magnetic domain walls,” *Nature nanotechnology*, vol. 8, no. 7, p. 527, 2013.
- [37] S. Emori, U. Bauer, S.-M. Ahn, E. Martinez, and G. S. Beach, “Current-driven dynamics of chiral ferromagnetic domain walls,” *Nature materials*, vol. 12, no. 7, p. 611, 2013.
- [38] J. Torrejon, J. Kim, J. Sinha, S. Mitani, M. Hayashi, M. Yamanouchi, and H. Ohno, “Interface control of the magnetic chirality in cofeb/mgo heterostructures with heavy-metal underlayers,” *Nature communications*, vol. 5, p. 4655, 2014.

- 
- [39] K.-S. Ryu, S.-H. Yang, L. Thomas, and S. S. Parkin, “Chiral spin torque arising from proximity-induced magnetization,” *Nature communications*, vol. 5, p. 3910, 2014.
- [40] T. L. Gilbert, “A phenomenological theory of damping in ferromagnetic materials,” *IEEE Transactions on Magnetics*, vol. 40, no. 6, pp. 3443–3449, 2004.
- [41] B. Koopmans, J. Ruigrok, F. Dalla Longa, and W. De Jonge, “Unifying ultrafast magnetization dynamics,” *Physical review letters*, vol. 95, no. 26, p. 267207, 2005.
- [42] D. C. Ralph and M. D. Stiles, “Spin transfer torques,” *Journal of Magnetism and Magnetic Materials*, vol. 320, no. 7, pp. 1190–1216, 2008.
- [43] L. Berger, “Low-field magnetoresistance and domain drag in ferromagnets,” *Journal of Applied Physics*, vol. 49, no. 3, pp. 2156–2161, 1978.
- [44] P. Freitas and L. Berger, “Observation of s-d exchange force between domain walls and electric current in very thin permalloy films,” *Journal of Applied Physics*, vol. 57, no. 4, pp. 1266–1269, 1985.
- [45] C.-Y. Hung and L. Berger, “Exchange forces between domain wall and electric current in permalloy films of variable thickness,” *Journal of applied physics*, vol. 63, no. 8, pp. 4276–4278, 1988.
- [46] J. Grollier, D. Lacour, V. Cros, A. Hamzic, A. Vaurès, A. Fert, D. Adam, and G. Faini, “Switching the magnetic configuration of a spin valve by current-induced domain wall motion,” *Journal of applied physics*, vol. 92, no. 8, pp. 4825–4827, 2002.
- [47] M. Kläui, C. Vaz, J. Bland, W. Wernsdorfer, G. Faini, E. Cambril, and L. Heyderman, “Domain wall motion induced by spin polarized currents in

- ferromagnetic ring structures,” *Applied physics letters*, vol. 83, no. 1, pp. 105–107, 2003.
- [48] M. Tsoi, R. Fontana, and S. Parkin, “Magnetic domain wall motion triggered by an electric current,” *Applied Physics Letters*, vol. 83, no. 13, pp. 2617–2619, 2003.
- [49] S. Zhang and Z. Li, “Roles of nonequilibrium conduction electrons on the magnetization dynamics of ferromagnets,” *Physical Review Letters*, vol. 93, no. 12, p. 127204, 2004.
- [50] S. Zhang and Z. Li, “Roles of nonequilibrium conduction electrons on the magnetization dynamics of ferromagnets,” *Physical Review Letters*, vol. 93, no. 12, p. 127204, 2004.
- [51] G. Dresselhaus, “Spin-orbit coupling effects in zinc blende structures,” *Physical Review*, vol. 100, no. 2, p. 580, 1955.
- [52] E. I. Rashba, “Properties of semiconductors with an extremum loop. i. cyclotron and combinational resonance in a magnetic field perpendicular to the plane of the loop,” *Physics of the Solid State*, vol. 2, pp. 1109–1122, 1960.
- [53] A. Manchon, H. C. Koo, J. Nitta, S. Frolov, and R. Duine, “New perspectives for rashba spin-orbit coupling,” *Nature materials*, vol. 14, no. 9, p. 871, 2015.
- [54] I. M. Miron, K. Garello, G. Gaudin, P.-J. Zermatten, M. V. Costache, S. Auffret, S. Bandiera, B. Rodmacq, A. Schuhl, and P. Gambardella, “Perpendicular switching of a single ferromagnetic layer induced by in-plane current injection,” *Nature*, vol. 476, no. 7359, p. 189, 2011.
- [55] U. H. Pi, K. Won Kim, J. Y. Bae, S. C. Lee, Y. J. Cho, K. S. Kim, and S. Seo, “Tilting of the spin orientation induced by rashba effect in ferromagnetic metal layer,” *Applied Physics Letters*, vol. 97, no. 16, p. 162507, 2010.

- 
- [56] N. Nagaosa, J. Sinova, S. Onoda, A. MacDonald, and N. Ong, “Anomalous hall effect,” *Reviews of modern physics*, vol. 82, no. 2, p. 1539, 2010.
- [57] M. Dyakonov and V. Perel, “Current-induced spin orientation of electrons in semiconductors,” *Physics Letters A*, vol. 35, no. 6, pp. 459–460, 1971.
- [58] N. F. Mott, “The scattering of fast electrons by atomic nuclei,” *Proc. R. Soc. Lond. A*, vol. 124, no. 794, pp. 425–442, 1929.
- [59] J. Hirsch, “Spin hall effect,” *Physical Review Letters*, vol. 83, no. 9, p. 1834, 1999.
- [60] S. Murakami, N. Nagaosa, and S.-C. Zhang, “Dissipationless quantum spin current at room temperature,” *Science*, vol. 301, no. 5638, pp. 1348–1351, 2003.
- [61] J. Sinova, D. Culcer, Q. Niu, N. Sinitsyn, T. Jungwirth, and A. MacDonald, “Universal intrinsic spin hall effect,” *Physical review letters*, vol. 92, no. 12, p. 126603, 2004.
- [62] Y. K. Kato, R. C. Myers, A. C. Gossard, and D. D. Awschalom, “Observation of the spin hall effect in semiconductors,” *science*, vol. 306, no. 5703, pp. 1910–1913, 2004.
- [63] E. Saitoh, M. Ueda, H. Miyajima, and G. Tatara, “Conversion of spin current into charge current at room temperature: Inverse spin-hall effect,” *Applied physics letters*, vol. 88, no. 18, p. 182509, 2006.
- [64] H. Zhao, E. J. Loren, H. Van Driel, and A. L. Smirl, “Coherence control of hall charge and spin currents,” *Physical review letters*, vol. 96, no. 24, p. 246601, 2006.

- 
- [65] S. O. Valenzuela and M. Tinkham, “Direct electronic measurement of the spin hall effect,” *Nature*, vol. 442, no. 7099, p. 176, 2006.
- [66] L. Liu, T. Moriyama, D. Ralph, and R. Buhrman, “Spin-torque ferromagnetic resonance induced by the spin hall effect,” *Physical review letters*, vol. 106, no. 3, p. 036601, 2011.
- [67] M. Hayashi, J. Kim, M. Yamanouchi, and H. Ohno, “Quantitative characterization of the spin-orbit torque using harmonic hall voltage measurements,” *Physical Review B*, vol. 89, no. 14, p. 144425, 2014.
- [68] K. Garello, I. M. Miron, C. O. Avci, F. Freimuth, Y. Mokrousov, S. Blügel, S. Auffret, O. Boule, G. Gaudin, and P. Gambardella, “Symmetry and magnitude of spin-orbit torques in ferromagnetic heterostructures,” *Nature nanotechnology*, vol. 8, no. 8, p. 587, 2013.
- [69] L. Liu, C.-F. Pai, Y. Li, H. Tseng, D. Ralph, and R. Buhrman, “Spin-torque switching with the giant spin hall effect of tantalum,” *Science*, vol. 336, no. 6081, pp. 555–558, 2012.
- [70] L. Liu, O. Lee, T. Gudmundsen, D. Ralph, and R. Buhrman, “Current-induced switching of perpendicularly magnetized magnetic layers using spin torque from the spin hall effect,” *Physical review letters*, vol. 109, no. 9, p. 096602, 2012.
- [71] W. Zhang, W. Han, X. Jiang, S.-H. Yang, and S. S. Parkin, “Role of transparency of platinum-ferromagnet interfaces in determining the intrinsic magnitude of the spin hall effect,” *Nature Physics*, vol. 11, no. 6, p. 496, 2015.
- [72] M.-H. Nguyen, D. Ralph, and R. Buhrman, “Spin torque study of the spin hall conductivity and spin diffusion length in platinum thin films with varying resistivity,” *Physical review letters*, vol. 116, no. 12, p. 126601, 2016.

- 
- [73] C.-F. Pai, L. Liu, Y. Li, H. Tseng, D. Ralph, and R. Buhrman, “Spin transfer torque devices utilizing the giant spin hall effect of tungsten,” *Applied Physics Letters*, vol. 101, no. 12, p. 122404, 2012.
- [74] K.-U. Demasius, T. Phung, W. Zhang, B. P. Hughes, S.-H. Yang, A. Kellock, W. Han, A. Pushp, and S. S. Parkin, “Enhanced spin-orbit torques by oxygen incorporation in tungsten films,” *Nature communications*, vol. 7, p. 10644, 2016.
- [75] Q. Hao and G. Xiao, “Giant spin hall effect and switching induced by spin-transfer torque in a w/co 40 fe 40 b 20/mgo structure with perpendicular magnetic anisotropy,” *Physical Review Applied*, vol. 3, no. 3, p. 034009, 2015.
- [76] O. Lee, L. Liu, C. Pai, Y. Li, H. Tseng, P. Gowtham, J. Park, D. Ralph, and R. A. Buhrman, “Central role of domain wall depinning for perpendicular magnetization switching driven by spin torque from the spin hall effect,” *Physical Review B*, vol. 89, no. 2, p. 024418, 2014.
- [77] C. Garg, S.-H. Yang, T. Phung, A. Pushp, and S. S. Parkin, “Dramatic influence of curvature of nanowire on chiral domain wall velocity,” *Science advances*, vol. 3, no. 5, p. e1602804, 2017.
- [78] K.-S. Ryu, L. Thomas, S.-H. Yang, and S. S. Parkin, “Current induced tilting of domain walls in high velocity motion along perpendicularly magnetized micron-sized co/ni/co racetracks,” *Applied Physics Express*, vol. 5, no. 9, p. 093006, 2012.
- [79] O. Boulle, S. Rohart, L. Buda-Prejbeanu, E. Jué, I. Miron, S. Pizzini, J. Vogel, G. Gaudin, and A. Thiaville, “Domain wall tilting in the presence of the dzyaloshinskii-moriya interaction in out-of-plane magnetized magnetic nanotracks,” *Physical review letters*, vol. 111, no. 21, p. 217203, 2013.

- 
- [80] S.-H. Yang, K.-S. Ryu, and S. Parkin, “Domain-wall velocities of up to 750 m s<sup>-1</sup> driven by exchange-coupling torque in synthetic antiferromagnets,” *Nature nanotechnology*, vol. 10, no. 3, p. 221, 2015.
- [81] M. Scheinfein, “LLG Micromagnetics Simulator Version 4,” 2015.
- [82] S. Parkin, N. More, and K. Roche, “Oscillations in exchange coupling and magnetoresistance in metallic superlattice structures: Co/ru, co/cr, and fe/cr,” *Physical Review Letters*, vol. 64, no. 19, p. 2304, 1990.
- [83] S. Parkin and D. Mauri, “Spin engineering: Direct determination of the ruderman-kittel-kasuya-yosida far-field range function in ruthenium,” *Physical Review B*, vol. 44, no. 13, p. 7131, 1991.
- [84] S. S. Parkin, “Systematic variation of the strength and oscillation period of indirect magnetic exchange coupling through the 3d, 4d, and 5d transition metals,” *Physical Review Letters*, vol. 67, no. 25, p. 3598, 1991.
- [85] C. Garg, A. Pushp, S.-H. Yang, T. Phung, B. P. Hughes, C. Rettner, and S. S. Parkin, “Highly asymmetric chiral domain-wall velocities in y-shaped junctions,” *Nano letters*, vol. 18, no. 3, pp. 1826–1830, 2018.
- [86] D. A. Allwood, G. Xiong, C. Faulkner, D. Atkinson, D. Petit, and R. Cowburn, “Magnetic domain-wall logic,” *Science*, vol. 309, no. 5741, pp. 1688–1692, 2005.
- [87] W. J. Gallagher and S. S. Parkin, “Development of the magnetic tunnel junction mram at ibm: From first junctions to a 16-mb mram demonstrator chip,” *IBM Journal of Research and Development*, vol. 50, no. 1, p. 5, 2006.
- [88] N. Locatelli, V. Cros, and J. Grollier, “Spin-torque building blocks,” *Nature materials*, vol. 13, no. 1, p. 11, 2014.

- 
- [89] A. Pushp, T. Phung, C. Rettner, B. P. Hughes, S.-H. Yang, L. Thomas, and S. S. Parkin, “Domain wall trajectory determined by its fractional topological edge defects,” *Nature Physics*, vol. 9, no. 8, p. 505, 2013.
- [90] T. Phung, A. Pushp, C. Rettner, B. P. Hughes, S.-H. Yang, and S. S. Parkin, “Robust sorting of chiral domain walls in a racetrack biperplexer,” *Applied Physics Letters*, vol. 105, no. 22, p. 222404, 2014.
- [91] A. Capua, S.-h. Yang, T. Phung, and S. S. Parkin, “Determination of intrinsic damping of perpendicularly magnetized ultrathin films from time-resolved precessional magnetization measurements,” *Physical Review B*, vol. 92, no. 22, p. 224402, 2015.
- [92] S. Fukami, M. Yamanouchi, S. Ikeda, and H. Ohno, “Depinning probability of a magnetic domain wall in nanowires by spin-polarized currents,” *Nature communications*, vol. 4, p. 2293, 2013.
- [93] A. Hubert, *Theorie der Domänenwände in geordneten Medien*. Springer, 1974.



# Publications

- [1] **Garg, C.**, Yang, S. H., Phung, T., Pushp, A., & Parkin, S. S. (2017). Dramatic influence of curvature of nanowire on chiral domain wall velocity. *Science advances*, *3*(5), e1602804.
- [2] **Garg, C.**, Pushp, A., Yang, S. H., Phung, T., Hughes, B. P., Rettner, C., & Parkin, S. S. (2018). Highly Asymmetric Chiral Domain-Wall Velocities in Y-Shaped Junctions. *Nano letters*, *18*(3), 1826-1830.
- [3] Zhang, J., **Garg, C.**, Phung, T., Rettner, C., Hughes, B. P., Yang, S. H., Jiang, Y., & Parkin, S. S. (2018). Role of Micromagnetic States on Spin–Orbit Torque-Switching Schemes. *Nano letters*.
- [4] Ali, M. N., Schoop, L. M., **Garg, C.**, Lippmann, J. M., Lara, E., Lotsch, B., & Parkin, S. S. (2016). Butterfly magnetoresistance, quasi-2D Dirac Fermi surface and topological phase transition in ZrSiS. *Science advances*, *2*(12), e1601742.
- [5] Yang, S. H., **Garg, C.**, & Parkin, S. S. (2018). Chiral Exchange Drag and Chirality Oscillations in Synthetic Antiferromagnets . *Nature Physics*, 2019.
- [6] Bläsing, R., Ma, T., Yang, S. H., **Garg, C.**, Dejene, F. K., N'Diaye, A.T., Chen, G., Liu, K., & Parkin, S. S. (2018). Exchange coupling torque in ferrimagnetic

---

Co/Gd bilayer maximized near angular momentum compensation temperature.  
*Nature Communications*, 2019.

[7] Zhang, J., Phung, C., Hughes, B. P., Yang, S. H., **Garg, C.**, Jiang, Y., & Parkin, S. S. (2018). Effect of interfacial insertion layers on the spin orbit torque in W(O) | CoFeB heterostructures. *Applied Physics Express*, 12(3),033001

# Acknowledgements

First and foremost, I'd like to thank my advisor, Dr. Stuart Parkin. I first had an opportunity to work with him during my master's internship. I originally intended to use that opportunity to get his recommendation to apply to grad school in the US. However, after seeing the incredible lab and research program he had set up, I knew that there wasn't a better place for me to do my Ph.D.. I am very grateful that Stuart supervised me well, yet trusted me and gave me ample freedom to work on projects. The projects he gave me were fun and challenging yet were also meaningful in the impact they could have outside the field of science. My meetings with him have been great opportunities for me to learn from his way of brainstorming ideas, editing out manuscripts, drafting a response to reviewers, and public speaking - stuff he's best at. He has also been very considerate towards various challenges (financial, administrative or otherwise) I faced during my Ph.D. and supported me in every way possible. Despite being my boss, I could always discuss science and work with him as a peer.

Apart from Stuart, I was also mentored by various other scientists in his lab - See-Hun Yang, Timothy Phung and Aakash Pushp. See-Hun is one of the most versatile scientists I have worked with. He grew thin film samples for me, taught me microfabrication of devices, performed modelling on my experimental results, and even gave me a ride back home for the period I didn't have a car. He was very supportive and involved in most of my Ph.D. and it is hard to imagine coming this far without his involvement. Tim was my go-to person to brainstorm ideas or

start new projects. He taught me a lot about magnetism and gave me the third-person perspective that students often need when they are stuck in a limbo. He also helped me perform micromagnetic simulations on some of my studies. Aakash gave me many interesting projects to work on, and trained me and supported me in a variety of ways when it came to experimental work.

There were several others who provided me support during my Ph.D. journey. Chris Lada is an excellent engineer who designed and tweaked many of the experimental setups I worked on. I am also thankful to Kevin Roche for providing support for various miscellaneous problems in the lab. Weifeng Zhang, Panos Filippou, Yari Ferrante, Jie Zhang and Jaewoo Jeong provided a great camaraderie. Mahesh Samant helped me with several of my questions related to materials growth. Larry Lindebauer, Dave Heffner and Manny Hernandez helped me with setting up experiments. Andrew Kellock helped me with RBS measurements. Teya Topuria, Erik Lara, Eugene Delenia helped me with TEM studies. Leslie Thompson helped me get XPS spectra for my samples. Brian Hughes and Charles Rettner were incredible help for helping me fabricate devices for my studies. Mazhar Ali taught me a lot about topological materials.

I'd also like to thank Prof. Nathan Newman of Arizona State University for inspiring me to take up research. I joined his lab as an undergraduate intern in 2012. Working in his lab was my first exposure to academic research and before that I was not interested in taking up a scientific career or even working in an industry remotely related to my degree. After finishing my internship with him, I got 2 publications, had a *rite of passage* in which I became an engineer/scientist, and ended up deciding to do a Ph.D..

Finally, I'd like to thank my family for the incredible support and flexibility they have provided me in choosing my career of choice. My mom in particular has been an incredible pillar of support. I am especially grateful to her for her love and for providing me with all the guidance. My uncles Montu and Sasha have been quite supportive of my research journey as well.

# Curriculum Vitae

First Name: Chirag  
Family Name: Garg  
Gender: Male  
Date of Birth: November 19<sup>th</sup>, 1991  
Place of Birth: Kapurthala, India  
Address: 378 Oleander Drive, San Jose, 95123 CA, USA  
Nationality: Indian

## ACADEMIC EDUCATION

09/2014– *Doctor of Philosophy in Engineering (Physics)*  
Martin-Luther-University Halle-Wittenberg, Halle, Germany

8/2009–6/2014 *Master's Degree in Ceramic Engineering*  
*Bachelor's Degree in Ceramic Engineering*  
Indian Institute of Technology, BHU

Chirag Garg  
San Jose, California, USA  
20<sup>th</sup> May 2019



# Eidesstattliche Erklärung

Hiermit erkläre ich, CHIRAG GARG, dass ich die vorliegende Arbeit mit dem Titel: **Investigating the Effect of Curvature on Chiral Domain Wall Velocity** in allen Teilen selbständig verfasst und keine anderen als die angegebenen Quellen und Hilfsmittel benutzt habe. Alle wörtlich oder sinngemäß übernommenen Textstellen habe ich als solche kenntlich gemacht.

Ferner liegen gegen mich weder gerichtliche Vorstrafen vor, noch sind staatsanwaltliche Ermittlungen oder Disziplinarverfahren eingeleitet worden.

Des Weiteren erkläre ich hiermit, dass ich bisher keine andere Arbeit zur Promotion eingereicht noch mit einer anderen Arbeit den Versuch zur Promotion unternommen habe.

San Jose, California, USA

den 21. September 2018

CHIRAG GARG